Volatile transport into the Earth's mantle

—

Experimental studies on the deep nitrogen cycle and on the (F,OH)-site in topaz

vorgelegt von

Diplom-Physikerin Anke Watenphul

aus Bottrop

Fakultät VI - Planen Bauen Umwelt

der Technischen Universität Berlin

zur Erlangung des akademischen Grades

Doktorin der Naturwissenschaften

– Dr. rer. nat. –

genehmigte Dissertation

Promotionsausschuss:

Vorsitzender:	Prof. Dr. M. Kaupenjohann
Gutachter:	Prof. Dr. W. Heinrich
Gutachter:	Prof. Dr. G. Franz
Gutachterin:	Prof. Dr. A. Holzheid

Tag der wissenschaftlichen Aussprache: 29.01.2010

Berlin 2010

D83

Und schnell und unbegreiflich schnelle
Dreht sich umher der Erde Pracht;
Es wechselt Paradieseshelle
Mit tiefer, schauervoller Nacht;
Es schäumt das Meer in breiten Flüssen
Am tiefen Grund der Felsen auf,
Und Fels und Meer wird fortgerissen
In ewig schnellem Sphärenlauf.

Johann Wolfgang Goethe
Faust – Der Tragödie erster Teil
Prolog im Himmel

Contents

1 Summary

Volatile elements are of particular interest in geosciences, because they are essential for the formation of the atmosphere and oceans and play a key role in sedimentary, magmatic, and metamorphic processes and thus in the evolution of crust and mantle. Volatiles have a large influence on physical, especially rheological properties of Earth materials and on the geochemical cycles of other elements. Nitrogen and hydrogen are major volatile elements. Their abundances, partitioning and cycling between the major reservoirs, atmosphere, crust and mantle, have been investigated in many studies during the last years. Still, the present knowledge of the nitrogen cycle is only fragmentary, in part because of the missing data on the nitrogen cycling between crust and deep mantle. In contrast, much more is known about the fate of hydrogen including the Earth's deep water cycle. The Earth's mantle consists mainly of the so called nominally anhydrous minerals. While water in these phases makes the major contribution to the water reservoir in the mantle, the portion of the nominally hydrous high-pressure silicate phases cannot be neglected. This is because they have a high transport capacity for water and often also other volatiles, e.g., halogens. Hence, the stabilities and crystal chemical properties of hydrous high-pressure phases are of great interest and this research topic is far from being exhausted.

This thesis tries to extend the knowledge about the two element cycles, nitrogen and hydrogen, in the Earth's interior and demonstrates a connection between them. They are intertwined via the subduction of nitrogen to the deep Earth as ammonium, NH_4, and its degassing as molecular nitrogen, N_2, which implies the occurrence of oxidation reactions during the recycling, in which NH_4 decompose to N_2 plus H_2O. The here synthesized new ammonium-bearing high-pressure phases may serve as nitrogen hosts in the deep mantle and therefore represent not only a nitrogen reservoir in these depth but also a contribution to the mantle water budget. An important model phase for volatile transport into the mantle is topaz because of it's simple composition and large extent of it's stability. Detailed investigation of the (F,OH)-solid solution series unraveled an unexpected complexity of the behavior of hydrogen in the crystal structure.

Chapter 2 consists of two parts. Section 2.1 provides an overview of the global geochemical nitrogen cycle. It describes the nitrogen exchange between the major reservoirs and outlines the current knowledge about the fate of nitrogen during subduction processes. The results of this thesis, the successful synthesis of high-pressure ammonium-bearing phases, and their role as potential nitrogen host phases in the mantle are discussed in this context. Moreover, the sizes of the nitrogen reservoirs, the contribution of the new ammonium high-pressure phases, the exchange between these reservoirs, and mass balance calculations are considered. The section ends with a review on nitrogen isotopes, the isotopic composition of the major nitrogen reservoirs, and the potential of nitrogen isotopes as tracers of subduction processes and their changes during the Earth's evolution. Section

2.2 summarizes the new insight into the hydrogen bond geometry of topaz. It discusses it's importance as model phase for other hydrous halogen-bearing minerals in the crust and the upper mantle, especially for the understanding of crystal chemical changes, which occur during subduction of nominally water-bearing minerals.

The detailed findings of this thesis follow in the chapters 3 to 6. They are presented in the form of the complete manuscripts, which are already published or submitted for publication.

Chapter 3 reports the synthesis of four new ammonium-bearing high-pressure phases NH_4-phengite, NH_4-cymrite, NH_4-Si-wadeite, and NH_4-hollandite between 4 and 12.3 GPa, 700 to 800 °C, which are analogues of high-pressure K-bearing phases. The run products were characterized by different analytical and spectroscopic techniques. Ammonium-incorporation is confirmed by the appearance of the NH_4-vibrational modes in the IR spectra. Powder XRD with Rietveld refinement shows enlarged unit cell dimensions compared to the potassium analogues, but no changes in the space group. In eclogite facies metasediments, nitrogen is mainly bound as ammonium in micas and feldspar substituting for potassium in the crystal structure. The synthesis of the here reported ammonium endmembers gives rise to the idea that, with ongoing subduction, ammonium is continuously redistributed into the newly formed high-pressure K-bearing phases. This possibly provides an important mechanism for nitrogen and hydrogen transport into the deeper mantle.

Chapter 4 focuses on the ammonium incorporation into high-pressure clinopyroxene. High-pressure experiments in the pseudobinary system $CaMgSi_2O_6 - (NH_4)M^{3+}Si_2O_6$, with M = Cr or Al, at 9.5 to 12.8 GPa, 725 to 750 °C produced NH_4-bearing diopside. The incorporation mainly takes place by the coupled substitution $(Ca^{2+})_{M2} + (Mg^{2+})_{M1} \Leftrightarrow (NH_4^+)_{M2} + (M^{3+})_{M1}$. Ammonium was determined by IR spectroscopy, the further minor and major elements by analytical TEM and EMP. Maximum ammonium concentrations in the range of 500 to 1000 ppm were found in Cr-bearing diopside. From that data, the nitrogen storage capacity of the upper mantle could be roughly calculated as 10^{12} mol N. Within the cycling process, nitrogen is transported to the mantle via cold slabs through NH_4 in sediments and metasediments, where it is stored in K-bearing high-pressure phases. Nitrogen is released by decomposition of these phases, followed by oxidation and subsequent degassing from the mantle.

Chapter 5 presents new insight into the hydrogen bonding geometry of topaz-OH. Temperature-dependent infrared spectra between –196 and 600 °C show four different OH-bands below –160 °C, which overlap to two bands upon heating, and further superpose to one broad asymmetric band above 400 °C. This proves the existence of four non-equivalent H positions in the crystal structure of topaz-OH, which were predicted by ab-initio calculations. Performance of an autocorrelation analysis on the IR spectra reveals two temperature-induced order–disorder phase transitions. With respect to the hydrogen atoms, the space group of topaz-OH changes from *P1* to $Pbn2_1$ to *Pbnm* over the investigated temperature range.

Chapter 6 reports the results of the IR spectroscopic investigation of the OH site in topaz over nearly the complete range of composition in the (F,OH)-solid solution series. Two different OH bands can be distinguished in the IR spectra. Their occurrence is determined by the local environment of the F/OH site in the crystal structure, i.e. local ordering of F and OH in neighboring sites. The typical sharp OH band, reported by many studies, stems from OH groups with fluorine in the neighboring site. The second band occurs as a shoulder on the low-energy wing of the sharp band if both neighboring sites are occupied by OH groups. The degree of local OH–OH ordering is determined by the OH concentration and can be predicted by probability calculations. The substitution of OH for F has a non-linear effect on the increase of the crystal structure. An autocorrelation analysis was performed on temperature-dependent IR spectra. It reveals two temperature-induced phase transitions. At -135 °C, the space group changes from *P1* to $Pbn2_1$. This change only takes place with respect to the hydrogen atoms. The transition at 175 °C is related to the reversal of the local ordering in the crystal structure. The complete disordering of F and OH causes a space group change from $Pbn2_1$ to *Pbnm*.

Zusammenfassung

Volatile Elemente sind für die Geowissenschaften von besonders großem Interesse, da sie maßgeblichen Einfluss auf die Bildung der Atmosphäre und Ozeane haben, eine Schlüsselrolle in sedimentären, magmatischen und metamorphen Prozessen spielen und somit die Evolution der Erdkruste und des Erdmantels maßgeblich mitbestimmen. Volatile Elemente beeinflussen physikalische, insbesondere rheologische, Eigenschaften von Geomaterialien und die geochemischen Kreisläufe anderer Elemente. Stickstoff und Wasserstoff gehören zu den wichtigsten flüchtigen Elementen. Die Bestimmung ihrer Häufigkeit, sowie ihrer Verteilung und ihres Austausches zwischen der Atmosphäre, der Erdkruste und dem Erdmantel sind seit Jahren Thema vieler Forschungsarbeiten. Trotzdem ist das aktuelle Wissen über den Stickstoffkreislauf sehr lückenhaft, besonders über den Stickstoffaustausch zwischen Erdkruste und -mantel ist nur wenig bekannt. Im Gegensatz dazu ist das geochemische Verhalten von Wasserstoff im Subduktionsprozess wesentlich besser verstanden. Der Erdmantel besteht im Wesentlichen aus so genannten nominell wasserfreien Mineralen. Vielen aktuellen Studien zufolge leisten diese den größten Beitrag zum Wasserreservoir im Erdmantel. Jedoch ist der Anteil der nominell wasserhaltigen silikatischen Hochdruckphasen nicht zu vernachlässigen, da diese eine hohe Transportkapazität für Wasser und andere Volatile (z.B. Halogene) besitzen. Daher sind die Stabilitäten und kristallchemischen Eigenschaften von nominell wasserhaltigen Hochdruckphasen von besonderer Relevanz und diesem Forschungsgebiet gilt weiterhin großes Interesse.

Das Ziel dieser Dissertation ist, das vorhandene Wissen über die geochemischen Kreisläufe von Stickstoff und Wasserstoff im Erdinneren zu erweitern. Es wird gezeigt, dass eine Verbindung zwischen beiden Kreisläufen besteht. Stickstoff wird als Ammoniummolekül, NH_4, in den Erdmantel subduziert und entgast in die Atmosphäre als molekularer Stickstoff, N_2. Demnach treten während des Recyclingprozesses im Mantel Oxidationsreaktionen auf, in denen NH_4 zu N_2 und H_2O zersetzt wird. In der vorliegenden Arbeit werden neue ammoniumhaltige Hochdruckphasen vorgestellt, welche potentielle Stickstoffträger im tiefen Mantel sein könnten und somit nicht nur ein Stickstoffreservoir in dieser Tiefe bilden, sondern auch einen Beitrag zur Gesamtwassermenge im Mantels liefern würden. Ein wichtige Modellphase für den Transport von Volatilen in Erdmantel ist Topas, weil er eine einfache Struktur und ein großes Stabilitätsfeld besitzt. Detaillierte Untersuchungen der (OH,F)-Mischkristallreihe zeigten ein sehr komplexes Verhalten von Wasserstoff in der Kristallstruktur.

Kapitel 2 ist in zwei Abschnitte unterteilt. Abschnitt 2.1 gibt einen Überblick über den globalen geochemischen Stickstoffkreislauf. Es wird der Stickstoffaustausch zwischen den wichtigen Stickstoffreservoiren beschrieben, sowie das bisherige Wissen über das Stickstoffverhalten in Subduktionsprozessen zusammengefasst. In diesem Zusammenhang werden die Ergebnisse dieser Dissertation, die Synthese von ammoniumhaltigen Hockdruckphasen,

vorgestellt und ihre Rolle als potentielle Stickstoffträger im Mantel erläutert. Die Größe der Stickstoffreservoire, der Beitrag der neuen ammoniumhaltigen Hochdruckphasen, sowie der Stickstoffaustausch zwischen den Reservoiren und Massenbilanzen werden diskutiert. Abschließend wird die Stickstoffisotopenverteilung in den wichtigen Reservoiren beschrieben und ihr Potential als Indikator für Subduktionsprozesse und deren Änderung im Laufe der Erdentwicklung diskutiert. Abschnitt 2.2 fasst die neuen Ergebnisse zum Wasserstoffeinbau in Topas zusammen. Es wird auf ihre Bedeutung im Hinblick auf andere OH- und halogen-haltige Minerale der Erdkruste und des oberen Mantels eingegangen, insbesondere für das Verständnis der kristallchemischen Änderungen während der Subduktion von wasserhaltigen Phasen.

Die Ergebnisse dieser Dissertation sind im Detail in den Kapiteln 3 bis 6 dargestellt. Sie werden in der Form von vollständigen Manuskripten präsentiert, welche bereits in Fachzeitschriften veröffentlicht sind oder zur Veröffentlichung eingereicht wurden.

In Kapitel 3 wird die Synthese von vier neuen ammoniumhaltigen Hochdruckphasen, NH_4-Phengit, NH_4-Kymrit, NH_4-Si-Wadeit und NH_4-Hollandit bei Drücken zwischen 4 und 12,3 GPa und Temperaturen zwischen 700 und 800 °C beschrieben. Diese Phases stellen Analoge zu K-haltigen Hochdruckphasen dar. Die Syntheseprodukte wurden mit verschiedenen analytischen und spektroskopischen Methoden charakterisiert. Der Ammonium-Einbau wurde durch das Auftreten von NH_4-Schwingungen in den Infrarotspektren nachgewiesen. Pulver-Röntgendiffraktometrie mit anschließender Rietveld-Verfeinerung ergab eine Vergrößerung der Gitterkonstanten verglichen mit den Kalium-Analogphasen. Dabei wurden keine Änderungen der Raumgruppen beobachtet. Stickstoff tritt in eklogitfaziellen Metasedimenten hauptsächlich als Ammonium in Glimmern und Feldspat auf, in welchen es anstelle des Kaliums in die Kristallstruktur eingebaut wird. Die erfolgreiche Synthese der beschriebenen Ammoniumendglieder lässt vermuten, dass Ammonium kontinuierlich in die während des Subduktionsprozesses neugebildeten K-haltigen Hochdruckphasen eingebaut werden kann. Dies zeigt einen möglichen Transportmechanismus für Stickstoff und Wasserstoff in den Erdmantel auf.

Kapitel 4 beschäftigt sich mit dem Ammoniumeinbau in Hochdruck-Klinopyroxene. In Hochdruckexperimenten im pseudobinären System $CaMgSi_2O_6 - (NH_4)M^{3+}Si_2O_6$, mit M = Cr oder Al, wurde NH_4-haltiger Diopsid bei 9,5 bis 12,8 GPa, 725 bis 750 °C synthetisiert. Der Ammonium-Einbau erfolgt über die gekoppelte Substitution $(Ca^{2+})_{M2} + (Mg^{2+})_{M1} \Leftrightarrow (NH_4^+)_{M2} + (M^{3+})_{M1}$. Mittels Infrarotspektroskopie wurde das eingebaute Ammonium nachgewiesen und quantifiziert. Die Konzentrationen der Haupt- und Spurenelemente wurden durch Messungen mit analytischem TEM und der Mikrosonde bestimmt. Die maximalen Ammoniumkonzentrationen lagen zwischen 500 und 1000 ppm in Cr-haltigen Diopsiden. Aus diesen Werten kann eine Stickstoffspeicherkapazität im oberen Mantels von näherungsweise 10^{12} mol N berechnet werden. Während seines Stoffkreislaufs wird Stickstoff durch kalte subduzierte Lithosphärenplatten als NH_4 in Sedimenten und Metasedimenten in den Mantel transportiert und dort in K-haltigen Hochdruckphasen gespeichert. Nach Abbau dieser Phasen, gefolgt von Oxidationsreaktionen, wird molekularer Stickstoff frei und gelangt durch Entgasung des Mantels an dee Erdoberfläche.

In Kapitel 5 werden neue Erkenntnisse zur Geometrie des Wasserstoffeinbaus in Topas-OH präsentiert. Temperaturabhängige Infrarotspektren zwischen –196 und 600 °C zeigen vier unterscheidbare OH-Banden unterhalb von –160 °C, welche mit steigender Temperatur zu zwei Banden überlappen und oberhalb von 400 °C zu einer breiten, stark asymmetrischen Bande verschmelzen. Dieses Ergebnis beweist die Existenz von vier unterschiedlichen Wasserstoffpositionen in der Kristallstruktur von Topas-OH und bestätigt deren Vorhersage aus ab-initio Berechnungen. Die Autokorrelationsanalyse der IR-Spektren zeigt zwei temperaturabhängige Ordnungs-Unordnungs-Phasenübergänge. Im untersuchten Temperaturbereich ändert sich die Topas-OH-Raumgruppe in Bezug auf die Wasserstoffatome von *P1* zu $Pbn2_1$ zu *Pbnm*.

Kapitel 6 beschreibt die infrarotspektroskopischen Untersuchungen der OH-Position in Topasen über fast die gesamte (OH,F)-Mischkristallreihe. In den IR-Spektren kann zwischen zwei OH-Banden unterschieden werden. Deren Auftreten wird durch die lokale Umgebung der F/OH-Position in der Kristallstruktur bestimmt, d.h. durch die lokale Ordnung von F und OH in benachbarten Positionen. Die für Topas typische und in vielen Studien beschriebene scharfe OH-Bande tritt auf, wenn sich in der benachbarten Position zur OH-Gruppe ein Fluoratom befindet. Die zweite Bande erscheint als Schulter auf der Niedrigenergieflanke der scharfen OH-Bande, wenn beide benachbarten Positionen mit OH-Gruppen besetzt sind. Der Anteil an lokaler OH–OH-Ordnung wird durch die OH-Konzentration im Kristall bestimmt und kann durch Wahrscheinlichkeitsrechnungen vorhergesagt werden. Die Substitution von OH für F hat einen nichtlinearen Effekt auf die Vergrößerung der Kristallstruktur. An den temperaturabhängigen IR-Spektren wurde eine Autokorrelationsanalyse durchgeführt, die zwei Phasentransformationen zeigt. Bei -135 °C ändert sich die Raumgruppe von *P1* zu $Pbn2_1$, wobei sich diese Änderung nur auf die Wasserstoffatome bezieht. Der Phasenübergang bei 175 °C hängt mit der Aufhebung der lokalen Ordnung in der Kristallstruktur zusammen. Die komplette Unordnung von F und OH bewirkt eine Änderung der Raumgruppe von $Pbn2_1$ zu *Pbnm*.

2 Introduction

This dissertation treats two topics, the deep nitrogen cycle and the hydrogen bond geometry in topaz. The main focus lies on the first topic, and more specifically on synthesis of nitrogen-bearing phases at mantle conditions, their potential as nitrogen carrier in subduction zones and the mantle, the resulting storage capacity, and the implications for the nitrogen cycle. Section 2.1 will give a brief overview of the current knowledge on the nitrogen cycle, the results from this thesis, and how these results might enhance the established picture of the deep nitrogen cycle. Moreover, topaz-OH occurred as additional run product associated with the synthesis of the high-pressure ammonium-bearing phases. The analysis of the run products revealed an interesting behavior of the hydrogen bonds in topaz-OH depending on temperature. Further investigations showed similar behavior for topaz of the (F,OH)-solid solution series. Section 2.2 summarizes these investigations and presents an overview of the new insight gained from these studies.

Geochemical cycles play a crucial role in the Earth's evolution. Hence, the determination of reservoirs and element abundances, and of the partitioning of elements and isotopes within and among these reservoirs helps not only to complete the picture of the present Earth, but gives also ideas about earlier states of the Earth and on the formation of the atmosphere, hydrosphere, and geosphere. Element cycles are not independent of each other, but are intertwined by different reactions. Nevertheless, single elements can be used as tracers for a wide range of processes, e.g., in the case of nitrogen from subduction of sediments to fertilization in agriculture.

2.1 Nitrogen cycle

The Earth can be divided into four major reservoirs, atmosphere, hydrosphere, biosphere, and geosphere. Nitrogen is present in all spheres and partly dominates the properties of individual reservoirs. Nitrogen is the major component of the atmosphere (78%), it is dissolved in the oceans, plays a key role in the biologic evolution as amino acids are the building blocks of proteins, and it is also a component in the crust and the mantle, e.g., as NH_4 in sediments or N in diamonds. The global nitrogen cycle describes the abundances, partitioning and exchange of nitrogen in and between atmosphere, hydrosphere, biosphere, and lithosphere. The occurrence and importance of nitrogen in all major reservoirs is in part related to the high number of oxidation states. It occurs in various species with valences ranging from -3 (NH_3) to +5 (NO_3^-).

On the one hand, numerous studies in the last decades focused on the nitrogen cycling between biosphere, atmosphere, and hydrosphere, and on human alteration of the cycle. This is due to the importance of nitrogen in the formation of proteins, DNA and hence life, and the need of fixed nitrogen in the agriculture to ensure the food production and

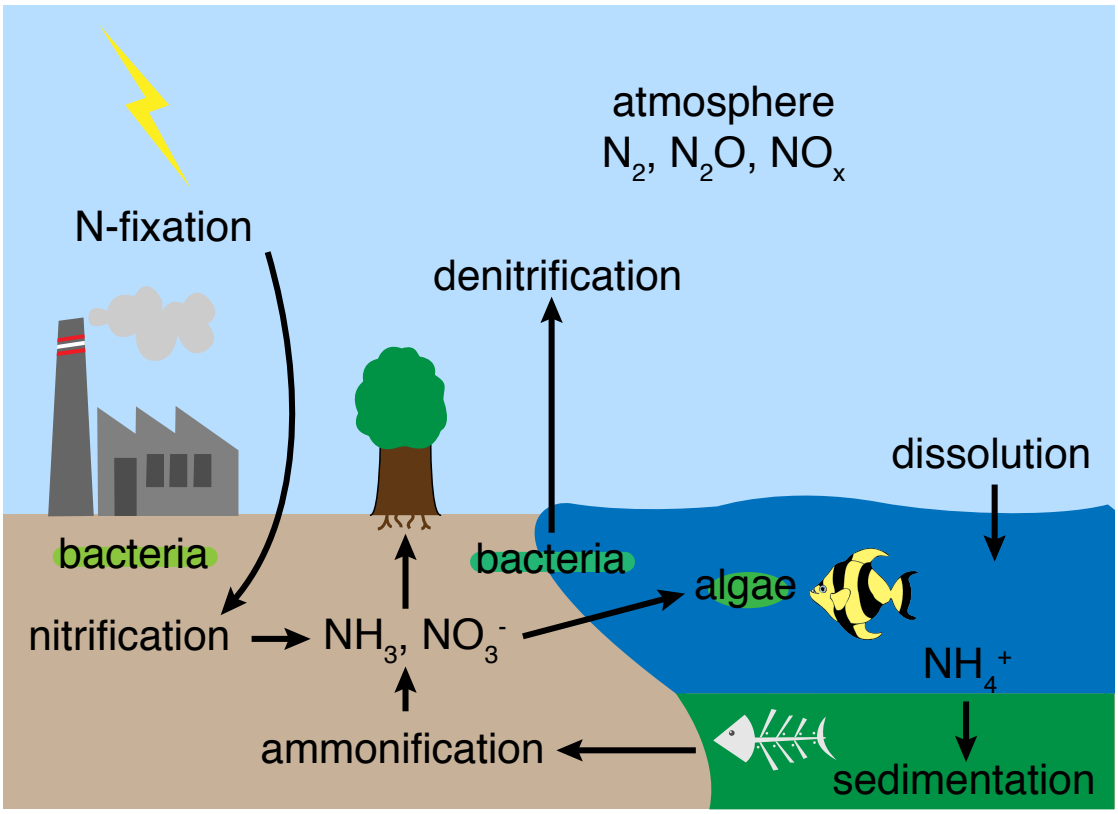

Figure 2.1: Illustration of the N-cycle between atmosphere, hydrosphere, and biosphere.

with that, the survival of humans (e.g., Delwiche, 1970; Vitousek et al., 1997; Devol, 2003; Galloway, 2004). On the other hand, much less is known on the nitrogen cycle in the solid Earth and the cycling between atmosphere/hydrosphere and lithosphere.

2.1.1 Nitrogen cycle between atmosphere/hydrosphere and biosphere

The cycling process of nitrogen between atmosphere, hydrosphere, and biosphere is illustrated in Figure 2.1. Nitrogen is with 78% the most abundant element in the atmosphere, where it is mostly present as molecular nitrogen, N_2. There are also small amounts of nitrous oxide, N_2O, which is the main regulator of ozone in the stratosphere, and of other nitrogen oxides summarized as NO_x. Interaction with the biosphere requires a fixation of the gaseous nitrogen by lightning, or by biological or industrial processes. Nitrification converts the atmospheric nitrogen to ammonia, NH_3, which is then, by different bacteria, further oxidized to nitrite, NO_2^-, and nitrate, NO_3^-. NH_3 and NO_3^- are direct nutrients for plants and, hence, for animals and humans. Ammonification reactions by bacteria and fungi restore the organic nitrogen after the death of plants or animals to the biological cycle as inorganic ammonia or ammonium. The recycling between biosphere and atmosphere is completed by the denitrification. The nitrates are stepwise reduced back by bacteria to

molecular nitrogen, which is released to the atmosphere.

Hydrosphere and atmosphere are linked by the dissolution of nitrogen and nitrogen oxides in seawater, rivers, and lakes. The cycling process involves again the biosphere. Microorganisms in the surface water carry out the nitrogen fixation. The produced ammonia is dissolved as ammonium in the water. Denitrification of decomposed organic matter releases nitrogen back to the atmosphere. Lastly, atmosphere and hydrosphere play another important role in the global nitrogen cycle because of their links with the geosphere.

2.1.2 Nitrogen cycle between surface and deep Earth

Nitrogen in crustal rocks originates principally from decomposed organic matter, which is deposited in sediments or introduced as secondary nitrogen in altered oceanic crust (AOC) (Krohn et al., 1993; Ramseyer et al., 1993; Holloway and Dahlgren, 1999; Li et al., 2007). Under anoxic conditions of methane formation at about 150 °C, amino acids decompose. The resulting ammonium is released into the fluid (Williams et al., 1992) and then readily incorporated into potassium-rich clay minerals, micas, and feldspars. The substitution of NH_4^+ for K^+ in the crystal lattice occurs due the similar in ionic radii (Shannon, 1976) and the equal charge. Seafloor sediments contain hundreds to thousands ppm N (Sadofsky and Bebout, 2004) incorporated by K-NH_4 exchange.

Generally, fresh mid-ocean ridge basalts (MORB) contain very little nitrogen, mostly less than 2 ppm (e.g., Cartigny et al. 2001a). In the time period between their eruption at mid-ocean ridges and their subduction into trenches, however, oceanic basalts undergo a massive alteration process involving extensive seawater-rock interaction over a wide temperature range (Alt et al. 1986), perhaps even involving biogeochemical alteration (Staudigel et al. 2006). These alteration processes significantly increase the nitrogen content of the altered oceanic crust by the formation of secondary nitrogen-bearing minerals in the basalts (e.g., Busigny et al., 2005; Li et al., 2007). In these secondary minerals (micas, feldspars, smectite), nitrogen is again fixed as ammonium. Concentrations reach about 10 ppm N, which is far lower than in sediments, but still higher than in MORB.

Subduction of oceanic crust, and particularly of sediments and subsequently metasediments, provides a powerful mechanism for nitrogen transport into the deep Earth. However, the fate of nitrogen in subduction zones is still not well studied. Investigations of volcanic and geothermal gases and brines showed that subducted nitrogen can be efficiently transferred back to the surface via arc volcanism. Calculated nitrogen inputs into trenches and outputs through the corresponding volcanic arcs based on local studies suggest that only little or none of the subducted nitrogen is recycled into the deeper mantle (e.g., Fischer et al., 2002; Hilton et al., 2002; Elkins et al., 2006). However, it is highly uncertain whether a local situation can be extrapolated to the global scale. Moreover, these calculations are based on many estimates (e.g., subduction depth, composition of the subducted crust, trench angle, subduction velocity, ...) and thus have relatively large uncertainties.

A more direct way to investigate the nitrogen behavior in subduction zones is the analysis of NH_4-bearing sediments subducted to different depths. During prograde metamorphism, nitrogen will be released through devolatilization reactions (Hallam and Eugster, 1976). Nitrogen isotopic analyses of metasediments show strong nitrogen devolatilization with increasing degree of metamorphism during subduction (e.g., Bebout and Fogel, 1992; Sad-

ofsky and Bebout, 2000; Mingram and Bräuer, 2001). In this process, nitrogen loss mainly occurs as degassed molecular nitrogen or ammonia, NH_3. High-grade metamorphic rocks show less than 10% of the initial nitrogen concentrations. The actual NH_4 concentrations in these rocks are probably primarily controlled by bulk fluid loss and fluid–rock interactions. The fractionation between ammonium-bearing potassium silicates and saline fluids has been experimentally studied by Bos et al. (1988) and Pöter et al. (2004). The NH_4 fractionation between phlogopite, $(NH_4, K)Mg_3AlSi_3O_{10}(OH)_2$, and dilute chloride solutions is small at 550 °C and 0.2 GPa (Bos et al., 1988). Pöter et al. (2004) showed that ammonium strongly fractionates into the fluid upon exchange between aqueous chloride solutions and (K,NH_4)-muscovite and (K,NH_4)-feldspar, respectively. The NH_4 fractionation between solid and fluid phases during subduction shows a slight dependence on pressure and temperature in the range from 0.4 to 1.5 GPa and 400 to 600 °C (Pöter et al., 2004). The experimental results suggest that ammonium is continuously released and expelled from the rocks during dehydration with progressive metamorphism. The remaining ammonium is continuously redistributed among the mica phases, and at higher metamorphic grades, also among feldspars. At these conditions, biotite may be the main host of ammonium. However, there is evidence from natural samples that almost the complete amount of nitrogen, bound as ammonium in phengitic mica, can remain in the rocks at least down to 90 km and very probably beyond the locus of island arc magmatism. Busigny et al. (2003) reported that no nitrogen was lost during the devolatilization processes in high to ultrahigh-pressure metasediments subducted along a cold geotherm ($\sim$ 8 °C/km). By this means, nitrogen is efficiently recycled to the deeper mantle.

The knowledge on nitrogen in the mantle is limited due to the low nitrogen abundances in analyzed mantle minerals. In fact, the main information about nitrogen from mantle depths comes from diamonds, mid-ocean ridge basalts, nitrogen-rich fluid inclusions in mantle xenoliths, and metal nitrides found as inclusions in coesite (e.g., Marty and Dauphas, 2003; Andersen and Neumann, 2001; Dobrzhinetskaya et al., 2008). Studies on nitrogen in diamonds and MORB are complementary. The nitrogen concentration in MORB is very low, normally only a few ppm (Cartigny et al., 1998), and difficult to assign to a specific source because of a possible degassing history or contamination by seawater during eruption (Pineau and Javoy, 1994). In contrast, the concentration of nitrogen in diamonds is usually much higher, albeit there exists a broad range from a few ppm to more than 1.2 wt% (Cartigny et al., 1997; 2001b). Diamonds form at about 150 km below continental roots and are, compared to MORB, resistant and unreactive. Therefore, they give better access to information about nitrogen in these mantle depth.

Fluid inclusions in most mantle xenoliths are generally dominated by CO_2. Nitrogen occurs most often only as trace or minor component (Pasteris, 1987; Huraiova et al., 1991). Therefore, the discovery of inclusions with pure nitrogen and $CO_2 - N_2$ mixtures with major N_2 in spinel dunite xenoliths from Lanzarote, Canary Islands, reported by Andersen et al. (1995) was quite surprising. The origin of these nitrogen-rich fluid inclusions is still a matter of debate. In principle, they might be representatives of metasomatic fluids in the upper mantle, draining pristine nitrogen from an underlying, fertile and non-degassed mantle, or recycled nitrogen of subducted sedimentary material (Andersen and Neumann, 2001).

Boron nitride (BN) and osbornite (TiN) were found as inclusions in coesite, which

indicates their formation under high pressure (Dobrzhinetskaya et al., 2008). The authors speculate that the origin of both nitrides might be a small fragment of boron-rich Si-Al metasediments, which was subducted to mantle depth. This theory is supported by the nitrogen isotopic signature in osbornite, which is characteristic for mantle nitrogen (see section 2.1.6).

Up to now, only a few studies tried to address the behavior of nitrogen in melts (e.g., Libourel et al., 2003; Roskosz et al., 2006; Mysen et al., 2008). Knowledge on the nitrogen concentration, speciation, and partitioning between crystals and melts as a function of pressure, temperature, melt composition, and especially the oxygen fugacity is required to understand the extraction from a hypothetical magma ocean or from the solid Earth through partial melting and degassing of mantle-derived magmas. Libourel et al. (2003) demonstrated that the nitrogen solubility and speciation in basaltic melts strongly depends on the oxygen fugacity. Nitrogen concentrations reach up to 0.7 wt% in nominally anhydrous alkali- and alkaline-earth silicate melts depending on the melt composition, pressure, and temperature (Roskosz et al., 2006). Mysen et al. (2008) showed that redox state and pressure have the largest effects on the nitrogen solubility, whereas the dependence on temperature is only minor. The most important effect might be the depolymerization of the melt by reduced NH-bearing complexes. Important melt properties such as viscosity, conductivity, diffusivity, and also thermodynamic properties depend on the melt polymerization. Element partitioning between minerals and melts, and liquids and solids are also affected. Qualitatively, dissolved and reduced nitrogen-bearing volatiles will change these properties in the same direction as dissolved water. Thus, the effect of nitrogen on melts and melting properties may be significant, even though it is only a minor component in the interior of the Earth (Mysen et al., 2008).

2.1.3 High-pressure ammonium-bearing silicates and ammonium-bearing clinopyroxene

The picture drawn here of the nitrogen cycle between surface and deep Earth has many gaps and question marks. At the one end, nitrogen is subducted as ammonium in white mica down to the locus of island arc magmatism (Busigny et al., 2003). Many studies propose nitrogen subduction beyond this depth, in particular the recycling of nitrogen to the deep mantle, but with exception of nitrogen as a constituent of diamonds, very small concentrations in MORB, and minor amounts in fluid inclusions in mantle xenoliths, the main nitrogen host phases in the deep Earth are unknown. At the other end of the cycle, nitrogen has been discharging from the Earth's interior for a long time through hydrothermal and volcanic activities (e.g., Javoy et al., 1986; Marty, 1995). A significant amount of nitrogen release occurs at mid-ocean ridges (Sano et al., 2001), which implies the existence of a nitrogen reservoir in normal mantle rocks, i.e., peridotites. Therefore, knowledge on nitrogen host phases in eclogitic and peridotitic mantle rocks, which connect these two ends of the nitrogen cycle, represents one of the important missing links.

This topic is addressed by two of the studies of this thesis. These focus on synthesis and characterization of possible nitrogen host phases stable at mantle depths and give some speculations on the fate of nitrogen during deep subduction along with estimates

on the nitrogen storage capacity of the mantle. The aim of both studies is to extent the present knowledge of nitrogen in mantle phases and thus to contribute to the completion of the picture of the nitrogen cycle. The results and implications are briefly summarized in this section to elucidate their contribution to answer the questions on the nitrogen cycle. The following chapters present the findings in detail, along with the description of the experimental and analytical methods.

Generally, ammonium in sediments and metasediments is incorporated into K-bearing silicates such as clay minerals, micas, and feldspars. One can reasonably assume that, under cold slab conditions, ammonium persists in the rocks as long as K-feldspar and high-pressure mica remain stable. In fluid-saturated metabasaltic and metapelitic model systems, K-phengite is stable up to 9.5 GPa, 750 to 1000 °C (Domanik and Holloway, 1996; Schmidt and Poli, 1998; Poli and Schmidt, 2002). At higher pressures, it breaks down to K-hollandite plus clinopyroxene-bearing assemblages. We were able to synthesize the ammonium-endmember of phengite, $NH_4(Mg_{0.5}Al_{1.5})(Al_{0.5}Si_{3.5})O_{10}(OH_2)$, at 4 GPa, 700 °C. Although there is no information on the upper stability limit, the strong similarities between K- and NH_4-phengite suggest a comparable stability for both endmembers, followed by similar breakdown products. The high-pressure breakdown products of K-feldspar depend on the water activity. In a wet system, K-feldspar is replaced by K-cymrite, $KAlSi_3O_8 \cdot H_2O$, above 2.5 GPa (Fasshauer et al., 1997). Above about 9 GPa, K-cymrite decomposes to K-hollandite, $KAlSi_3O_8$, plus fluid (Thompson et al., 1998). In a dry system, K-feldspar first reacts to K-Si-wadeite, $K_2Si_4O_9$, plus kyanite and coesite above 5 to 6.5 GPa, 400 to 1000 °C (Yagi et al., 1994; Urukawa et al., 1994). Above 9 GPa and in the presence of Al-bearing phases, K-Si-wadeite can further react to K-hollandite (Yong et al., 2008), otherwise it is stable to at least 15 GPa (Trønnes, 2002). K-hollandite was shown to be stable up to 95 GPa, 2300 °C (Konzett and Fei, 2000; Tutti et al., 2001). Thus, it might be the most important K-rich solid in the transition zone and the lower mantle. Ammonium analogues of these potassium silicates were synthesized in high-pressure experiments using a multi-anvil apparatus. Using buddingtonite, $NH_4AlSi_3O_8$, the ammonium analogue of K-feldspar, and ammoniac solution, NH_4OH_{aq}, as starting materials, NH_4-cymrite was synthesized at 7.8 GPa, 800 °C, NH_4-Si-wadeite at 10 GPa, 700 °C, and NH_4-hollandite at 12.3 GPa, 700 °C (see chapter 3 of this thesis). Muscovite and tobelite, K-feldspar and buddingtonite, and K- and NH_4-phlogopite form complete solid solution series (Bos et al., 1988; Pöter et al., 2004, 2007). All synthesized high-pressure NH_4-phases are very similar to their K-analogues in structure and stability. Therefore, it is very probable that they also form complete solid solution series. The occurrence of natural ammonium-bearing phengitic mica, subducted at least down to 90 km (Busigny et al., 2003), strongly supports this idea. Hence, high-pressure K-phases can incorporate large amounts of ammonium into their crystal structures. With ongoing subduction, this ammonium should be continuously redistributed into the newly formed high-pressure K-silicates. If so, it is likely that mantle nitrogen, which has a sedimentary isotopic signature (see section 2.1.6), originates not only from carbonaceous matter, but also from deeply subducted feldspars and micas.

The NH_4-endmembers of phengite, cymrite, wadeite, and hollandite are easily synthesized. However, neither of these phases nor their K-endmembers has been reported to occur in nature, except of phengitic mica. This indicates that they are very rare or unstable during ascent. Therefore, it is of particular interest to look for typical mantle minerals that

could host nitrogen. Among the major phases in eclogites and peridotites, clinopyroxene represents the most probable candidate for the incorporation of ammonium. Natural high-pressure clinopyroxene can contain several wt% K_2O (Perchuk et al., 2002; Bindi et al., 2003). Experimental studies showed that the incorporation mechanism is based on the coupled substitution $(Ca^{2+})_{M2} + (Mg^{2+})_{M1} \Leftrightarrow (K^{+})_{M2} + (M^{3+})_{M1}$, with M^{3+} = Al or Cr (Harlow 1997; Safonov et al., 2003; Harlow and Davies, 2004). In analogy to the high-pressure NH_4-silicates, it is reasonable to assume that clinopyroxene can incorporate ammonium by the same substitution mechanism with NH_4^+ replacing K^+. Two different types of diopsides were synthesized in high-pressure experiments in the pseudobinary system $CaMgSi_2O_6 - (NH_4)M^{3+}Si_2O_6$, with M = Cr or Al, at 9.5 to 12.8 GPa, 725 to 750 °C. In the first type, Ca + Mg are exchanged by NH_4 + Al, which might be typical for eclogitic high-pressure rocks. The second type might be representative for less aluminous peridotitic mantle rocks, with Ca + Mg exchanged by NH_4 + Cr. Ammonium quantification by infrared spectroscopy showed that the uptake of NH_4 in Al-diopside is about 100 ppm at mantle conditions, whereas Cr-diopside can incorporate several hundreds to thousand ppm NH_4.

The breakdown of ammonium-bearing phengite should result in NH_4-Al-bearing clinopyroxene and NH_4-bearing hollandite as described above. The low ammonium uptake of Al-diopside suggests that ammonium preferentially partitions into the phases that are richer in potassium, e.g., K-hollandite. On the other hand, Cr-diopside incorporates much more ammonium, which makes it an ideal candidate for nitrogen storage at mantle depth.

A further aspect of the ammonium incorporation into potassium-rich high-pressure phases such as phengite, cymrite, wadeite, hollandite, and clinopyroxene is the contribution to the mantle water budget. The breakdown of these ammonium-bearing phases at either oxidizing or reducing conditions will result in the formation of water. Apart from its OH-incorporation, clinopyroxene can contribute about 10^{12} mol H_2O to the mantle water budget via release and subsequent breakdown of its NH_4 component. The contribution by ammonium component in the other high-pressure silicates in cannot be estimated because their amounts in the Earth's mantle are unknown.

2.1.4 Stability of ammonium-bearing phases and redox conditions

The stability of high-pressure ammonium-bearing phases depends strongly on the redox conditions. During formation of these phases in a mineral–fluid system, these conditions need to be reducing enough to prevent the oxidation of NH_3/NH_4^+ to molecular nitrogen. Analogous to the nitrogen speciation in melts, the speciation in fluids depends on pressure, temperature, fluid composition, and perhaps most importantly on the oxygen fugacity f_{O_2}. There is only little information on the speciation in H–N–O fluids at very high pressures. At upper mantle pressures and temperatures, H–N–O fluids buffered by fayalite–magnetite–quartz (FMQ) will consist of H_2O and N_2 (Churakov and Gottschalk, 2003a,b; Simakov, 1998). There is an abrupt transition in the nitrogen speciation in the fluid from N_2 to NH_3 at f_{O_2} about 3 log units below FMQ. Increasing pressure favors the formation of NH_3. Frost and McCammon (2008) showed that the Earth's mantle becomes more reduced with depth. Upper mantle oxygen fugacities recorded by spinel peridotites range between ΔFMQ $\pm$ 2

log units. Garnet peridotites from cratonic lithosphere reveal f_{O_2} of ΔFMQ = -3 to -4 log units at 4 to 6 GPa. Modeling indicates that the oxygen fugacity may attain -5 log units below FMQ at 8 GPa.

The input of ammonium into the mantle by slab minerals, the main storage in clinopyroxene as NH_4, and the output as molecular nitrogen through hydrothermal and volcanic processes requires the occurrence of oxidation reactions at the end of the deep nitrogen cycle. The change in the redox conditions from reducing to more oxidizing might lead to reactions of the type NH_4-bearing phase + O_2 $\rightarrow$ phase(s) + 0.5 N_2 + 2 H_2O. This is supported by the occurrence of fluid inclusions with predominant N_2 in olivine porphyroclasts in spinel dunites from a chrome diopside suite (Lanzarote, Canary Islands). Andersen et al. (1995) discussed that the molecular nitrogen was produced by oxidation and breakdown of NH_4-bearing phlogopite or amphibole as a consequence of increasing oxygen fugacity and/or temperature. However, there is no indication for these nominally OH-bearing phases in these xenoliths. Based on the here obtained NH_4 storage capacity of Cr-bearing diopside, it is suggested that the release of the ammonium component in the diopsides followed by oxidation to N_2 lead to these nitrogen-rich inclusions.

In summary, the decreasing oxygen fugacity with depth suggests a preferred stability of ammonium-bearing phases, e.g., NH_4-bearing hollandite and clinopyroxene, in the lower part of the upper mantle. In the upper part, most of the recycled nitrogen is almost directly released as N_2 by ascent of fluids, so that less than 10% (Mingram and Bräuer, 2001) of the original sedimentary nitrogen content is subducted to greater depth.

2.1.5 Nitrogen reservoirs, fluxes, and mass balances

Modeling of the global nitrogen cycle requires knowledge on the amount of nitrogen stored in the main reservoirs, along with the input and output nitrogen fluxes. Constraints on nitrogen fluxes and inventories at subduction zones are crucial to understand the nitrogen budget and its recycling between atmosphere/hydrosphere, crust and mantle.

The Earth's atmosphere consists of 78% N_2, which amounts to about 1.38×10^{20} mol N_2 (Zhang and Zindler, 1993). The nitrogen content in the biosphere is about 1.1×10^{15} mol N_2 (Wedepohl, 1978). Sedimentary rocks contain about $(0.22 \pm 0.10) \times 10^{20}$ mol N_2, and about $(0.20 \pm 0.10) \times 10^{20}$ mol N_2 are stored in igneous rocks in the crust (Zhang and Zindler, 1993). Baur and Wlotzka (1974) proposed that the Earth's mantle is the dominant global nitrogen reservoir despite the much higher concentrations in the atmosphere, and sedimentary and other crustal rocks. However, the nitrogen concentration in the mantle is not well constrained. A recent study by Marty and Dauphas (2003) concluded that the amount of nitrogen stored in the silicate Earth is comparable to that in the atmosphere. The capability of clinopyroxene to host nitrogen as ammonium provides a considerable storage capacity in the upper mantle. A rough estimation, using values of 400 km for the depth range of the upper mantle, in which clinopyroxene is stable, 3.5 g/cm^3 for the mean rock density, 13 vol% clinopyroxene on average in the upper mantle, and 0.01 molecules NH_4 per formula unit clinopyroxene (corresponding to about 500 ppm NH_4), results in a calculated nitrogen storage capacity of 10^{12} mol nitrogen for the whole upper mantle. Although clinopyroxene might represent a large nitrogen reservoir in the mantle, the amount of nitrogen stored in it is still vanishingly small compared to those present

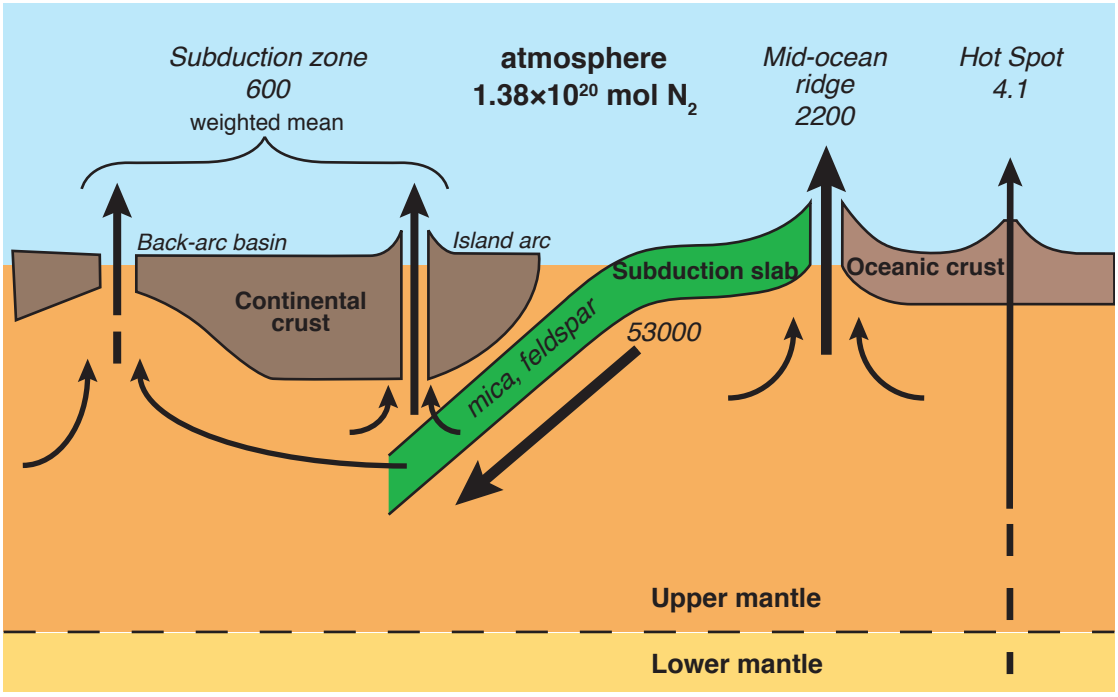

Figure 2.2: Schematic illustration of the N-cycle between surface and mantle. Amount of nitrogen recycled into the mantle via NH_4-bearing minerals in subduction slabs from Busigny et al. (2003), outgoing N_2-fluxes in subduction zones, mid-ocean ridges, and hot spots from Sano et al. (2001), extent of the atmospheric nitrogen reservoir from Zhang and Zindler (1993). Italicized numbers indicate the nitrogen flux in 10^6 mol N_2/a.

in the atmosphere, biosphere, and crust. Additional nitrogen reservoirs at mantle depths are diamonds, MORB before eruption, and further ammonium-bearing silicates such as phlogopite and amphibole observed in mantle xenoliths (Andersen et al., 1995; Yokochi et al., 2009). These reservoirs are very hard to quantify, but do probably not exceed the nitrogen storage capacity of clinopyroxene. Therefore, further nitrogen host phases should exist in the mantle, if the assumption is valid that nitrogen amounts in the atmosphere and the solid Earth are roughly equal, as suggested by Marty and Dauphas (2003). Possible candidates are NH_4-bearing hollandite and wadeite, and speculative further phases given the remaining large assumed nitrogen imbalance.

Nitrogen output fluxes from the solid Earth occur at back-arc basins, island arcs, mid-ocean ridges, and hot spots (Fig. 2.2). Several studies in the last years estimated the nitrogen output at mid-ocean ridges, which sample normal mantle rocks, i.e. peridotites. Estimates for the yearly output range between 1.2 and 8.5×10^9 mol N_2/a (e.g., Javoy et al., 1986; Zhang and Zindler, 1993; Marty, 1995; Sano et al. 2001). Fluxes from hot spots are significantly smaller and amount to about 4.1×10^6 mol N_2/a (Sano et al. 2001). The most extensive study on nitrogen output by arc volcanism was presented by Hilton et al.

(2002). That nitrogen flux, as based on measured emissions of 45 arc volcanoes from 11 regions, amounts to 1.98×10^{10} mol N_2/a (Hilton et al., 2002). It might be higher, about 3.2×10^{10} mol N_2/a, adding 20% flux for volcanoes, for which no or little data for output fluxes exist. Hilton et al. (2002) also provided estimates of the input nitrogen flux via trenches considering both subducted sediments as well as the underlying crustal basement (up to a thickness of 7 km) of 26 subduction zones. In total, 4.48×10^{10} mol N_2 are subducted each year, including 1.37×10^{10} mol N_2/a in sediments and 3.11×10^{10} mol N_2/a in the crustal basement.

A basic assumption for mass balance calculations is that the flux of crustal material into the deep mantle through subduction is approximately equal to the amount of new oceanic crust generated from mantle sources at mid-ocean ridges plus small amounts of ocean-island basalts. Enrichment of nitrogen in the mantle is supported by mass balance considerations based on the numbers given in the previous paragraph, because the amount of released nitrogen is lower than the amount nitrogen in the subducted oceanic crust. However, comparison of calculated input and output flux for specific localities such as the Nicaraguan volcanic front (Elkins et al., 2006) shows that both fluxes balance each other quite well. Based on this, Elkins et al (2006) concluded that nearly 100% of the subducted nitrogen is emitted at the volcanic front and little to none is transported beyond the zone of arc magma generation. A different approach was used by Busigny et al. (2003), who reported deep recycling of nitrogen in metapelites and metabasites in cold slab environments. They suggest that, at such pressure and temperature conditions, the amount of recycled nitrogen can be deduced from the K/N ratio because the capacity of the sediment to fix nitrogen depends mainly on the amount of K-bearing minerals in the rock, and thus on the potassium content. Based on this assumption, Busigny et al. (2003) calculated a range in the global amount of deeply subducted nitrogen from 3.4 to 5.4×10^{10} mol N_2/a.

In summary, nitrogen mass balances for subduction zones are based on comparison of the estimated N-input in trenches and N-output in volcanic and hydrothermal gases and brines. Both estimates comprise many uncertainties, e.g., unknown amounts of non-degassed nitrogen in volcanic and plutonic rocks, spatial and temporal variations of input and output within individual arc-trench segments, nitrogen loss due to devolatilization in the forearc (Li et al., 2007), and unknown reliability of the interpolation from local to global scale. Nitrogen input and output fluxes are in favor for a recycling into the mantle, but differ by less than one order of magnitude. Therefore, current estimates of the efficiency of subduction-related nitrogen recycling can be only regarded as semi-quantitive. Conclusions on the amount of nitrogen transported into the Earth's mantle via subduction have to be drawn with caution.

2.1.6 Nitrogen isotopes as tracer of the Earth's evolution

Another aspect of the global nitrogen cycle is the existence of nitrogen reservoirs with isotopically different compositions in the biosphere and hydrosphere, and particularly in the geosphere. Understanding the evolution of these isotopically different reservoirs makes an important contribution to the understanding of the global nitrogen cycle. This is because the evolution of the nitrogen isotopic composition of the reservoirs involves the

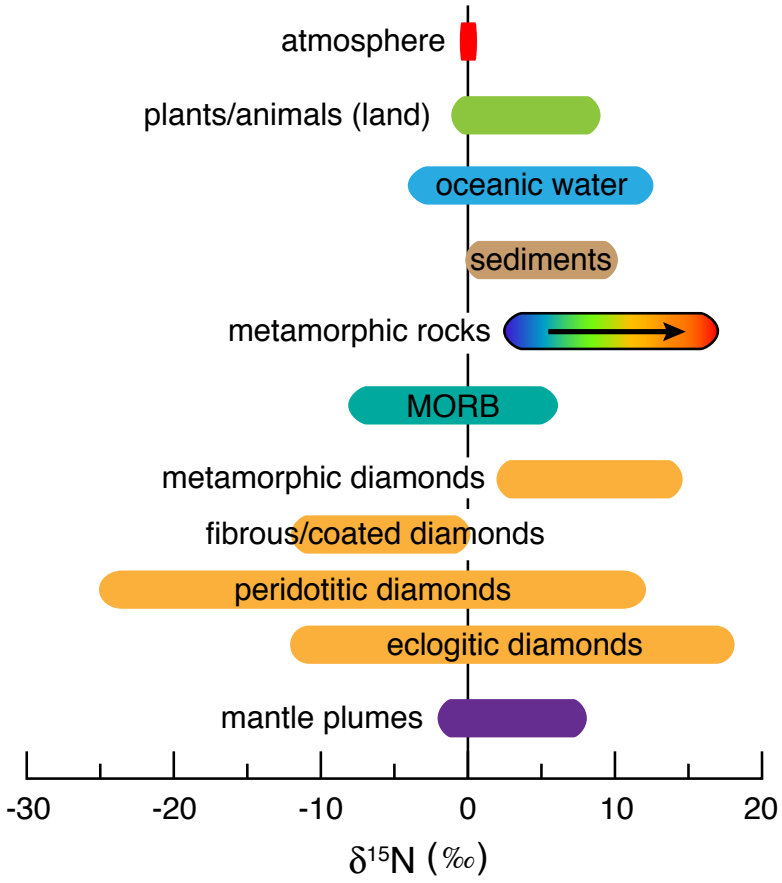

Figure 2.3: Variation in the nitrogen isotopic composition of atmosphere, organic matter, oceans, sediments, metamorphic rocks, mid-ocean ridge basalts (MORB), various diamond types, and mantle plumes. The arrow in the bar for the metamorphic rocks indicates the δ^{15}N evolution with increasing metamorphic grade. Sources of data: atmosphere, oceanic water, and sediments: Hoefs (2009); plants/animals: Wada et al. (1976); metamorphic rocks: Haendel et al. (1986); MORB and all diamond types: Cartigny (2005); mantle plumes: Marty and Dauphas (2003).

timeframe from the early Hadean (from the origin of the Earth's core, mantle, oceans, and atmosphere) to the Present and thus spans almost the entire history of the Earth.

Nitrogen has two stable isotopes, ^{14}N and ^{15}N, with abundances of 99.63% and 0.37% (Rosman and Taylor, 1998). The nitrogen isotopic signature, δ^{15}N, expresses the deviation of a particular ^{15}N/^{14}N ratio from the atmospheric ratio, which is used as standard with δ^{15}N = 0‰ by definition.

Figure 2.3 gives an overview of the nitrogen isotopic variation in important reservoirs and additionally in several diamond types. The nitrogen isotopic signature of organic matter is predominantly positive. Although all processes in the biogeochemical nitrogen cycle illustrated in Fig. 2.1 cause a certain degree of nitrogen isotopic fractionation, the

dominating reaction is the denitrification. Described in a very simplified way, nitrogen leaves the atmosphere via biological fixation and is returned via denitrification. Thus, these two processes control the isotopic composition of organic nitrogen. Wada et al. (1975) showed that biological fixation causes no significant nitrogen isotopic fractionation between the atmosphere and organic nitrogen. During denitrification, ^{14}N preferentially returns to the atmosphere, whereas NO_3^-, which is enriched in ^{15}N, is dissolved in the oceanic water. Therefore, oceanic water displays a mean $\delta^{15}N$-value of +6‰ (Beaumont and Robert, (1999) and references therein). Nitrogen in sediments has organic origin and thus a very similar isotopic signature. Sediments are also enriched in the heavier nitrogen isotope, with an average $\delta^{15}N$-value of +6 to +7‰ (Sweeney et al., 1978). With increasing metamorphism, devolatilization leads to a decrease in the nitrogen content and a relative enrichment in ^{15}N in the high-grade metamorphic rocks (Haendel et al., 1986).

Nitrogen in the biosphere, hydrosphere, sediments, metasediments and crustal igneous rocks has positive $\delta^{15}N$-values compared to the atmosphere. Use of a simple model of the nitrogen cycle, which is based on the present atmospheric value of 0‰, recycling of ^{15}N-enriched crustal rocks, and degassing of ^{14}N-enriched molecular nitrogen from the depths, results in mean $\delta^{15}N$-values > 0 for the Earth's mantle (e.g., Boyd et al., 1994; Cartigny et al., 1997). This is in conflict with the observations on the majority of mantle samples, because $\delta^{15}N$-values found in peridotitic and eclogitic diamonds and MORB are on average negative (~ -6‰; Cartigny, 2005). Only mantle plumes, which sample the lower mantle, show an enrichment in ^{15}N (mean value $\sim +3$; Marty and Dauphas, 2003) in agreement with that model. Overall, the simplified model of the deep nitrogen cycle does not explain the origin of the isotopic heterogeneities in the solid Earth.

This so-called imbalance between internal (mantle) and external (atmosphere + sediments + crust) reservoirs is especially obvious in the case of diamonds, which provide one of the most important sources of information about mantle nitrogen. Diamonds originate from depths ranging from about 150 to $>$ 700 km below the Earth's surface (Stachel et al., 2005) and incorporate nitrogen as their main trace element. Importantly, diamonds preserve the information about the mantle reservoirs they grew from because they remain virtually unchanged during their ascent. In summary, $\delta^{15}N$-values of diamonds vary widely between -25‰ (Cartigny et al., 1997) and 18‰ (Cartigny, 2005). However, significant differences manifest if one takes their origin into account (Fig. 2.3). Metamorphic diamonds, whose formation is associated with the subduction of continental crust, have distinctly positive $\delta^{15}N$-values (Cartigny, 2005). The incorporated nitrogen is derived from subducted sediments and thus has organic origin, which explains the enrichment in ^{15}N. The $\delta^{15}N$-values of fibrous and coated diamonds are negative and center around -5‰, which is very close to the assumed typical mantle nitrogen signature derived from values for MORB. In agreement with that, Boyd and Pillinger (1994) suggested that fibrous and coated diamonds grew from fluids, which are derived from the convecting mantle. The nitrogen isotopic signature of peridotitic diamonds spreads over the largest range, but most values ($\sim$ 65%) are negative with an average of -5 ± 3‰ (Cartigny, 2005). This equals the assumed typical mantle nitrogen isotopic signature. Eclogitic diamonds, however, presumably formed from sediments recycled into the mantle. Thus, it can be expected that their $\delta^{15}N$-values are positive because of the relative ^{15}N enrichment during subduction, which is also found in the metamorphic diamonds. Although the range of the nitrogen

isotopic composition is shifted towards positive values compared to peridotitic diamonds, about 70% of the δ^{15}N-values of eclogitic diamonds are in fact negative (Cartigny, 2005). This implies that most nitrogen incorporated into eclogitic diamonds has no sedimentary origin.

Several models have been proposed to conciliate the isotopic heterogeneities within the solid Earth (e.g., Exley et al., 1986; Marty and Humbert, 1997; Javoy, 1998; Marty and Dauphas, 2003). The results from this thesis suggest that, with ongoing subduction, nitrogen in the form of ammonium can be redistributed into potassium-bearing high-pressure phases, and thus be transported down to the transition zone and possibly beyond. In view of these results, the model by Marty and Dauphas (2003) is favored. In short summary, they propose that the ancient mantle was presumably depleted in ^{15}N and the isotopic composition of the recycled organic nitrogen has changed from initially negative δ^{15}N-values towards an increasingly positive isotopic signature in the Late Archean, the Proterozoic and the Phanerozoic, up to the values found in recent sediments. Therefore, the recycling of initially isotopically light nitrogen derived from early organic matter could account for the ^{15}N-depleted nitrogen component present in most diamonds and MORB. In the Archean, ^{15}N-depleted nitrogen was recycled in large mantle domains and was well mixed due to high convection rates. The hotter mantle prevented the subduction of slabs to the deepest mantle, which preserved the isotopic signature in these regions. Eclogitic diamonds with negative δ^{15}N-values originated from subducted slabs containing Archean organic matter. In the Proterozoic and the Phanerozoic, the subducted material became enriched in ^{15}N because photosynthesis produced increasing oxygen concentrations in the oceans and the atmosphere, which permitted formation of NO_3^-. This enabled denitrification and, thus, led to an increased nitrogen isotope fractionation. Subducted slabs could now reach lower mantle regions sampled by mantle plumes. Eclogitic diamonds with positive δ^{15}N-values are thought to originate from slabs, which were subducted in the Proterozoic and the Phanerozoic.

Other studies pointed out that nitrogen isotope fractionation during degassing, diamond growth, and also during ammonium redistribution into successor high-pressure phases cannot be neglected. Otherwise, any nitrogen isotope variability, even that in samples from the same locality, would have to be assigned to heterogeneities in the source material, which would imply the usually questionable assumption that sediments of very different age were subducted simultaneously (e.g., Cartigny and Ader, 2003; Thomassot et al., 2007).

It appears that the variability of the nitrogen isotopic composition in the Earth's mantle, and particular in mantle-derived diamonds, may primarily reflect distinct nitrogen sources. But, mineral–fluid/melt reactions controlled by the mineral assemblage of the rocks, in which for example the diamonds formed, could be an important factor in producing the observed nitrogen isotopic variations. Furthermore, fractionation of nitrogen isotopes will occur during subduction, and variability is additionally produced because nitrogen is not only transported into the mantle via carbonaceous material, but also via ammonium in silicates, as discussed in section 2.1. Thus, the isotopic evolution of the nitrogen reservoirs in the Earth's interior is far from being completely understood as no isotopic fractionation data are available for high-pressure mineral-fluid/melt systems.

2.2 Hydrogen bond geometry in topaz

2.2.1 Hydrous halogen-bearing minerals in subduction zones

Hydrous minerals are widespread in the Earth's crust and the upper mantle. Typical examples are clay minerals, micas, amphiboles, humites, and serpentines. Subduction of these minerals replenishes the mantle with hydrogen and further volatile elements. Calculated estimates for the annual global flux of subducted water vary in wide ranges, but are usually in the order of $5 \cdot 10^{13}$ mol H_2O/a, with about 40% structurally bound in hydrous minerals, mostly serpentines (Jarrard, 2003). Ongoing subduction causes stepwise dehydration of the these minerals. Beyond 220 km, only a few hydrous phases remain, e.g., topaz-OH, phase egg, lawsonite, and dense hydrous magnesium silicates (DHMS), and the volumetrically dominant nominally anhydrous minerals (NAMs) become the principle hydrogen reservoir at greater depths (Schmidt and Poli, 2003).

A couple of studies showed that the stability of hydrous phases is strongly affected by the hydrogen bond geometry (e.g., Parise et al., 1994; Catti et al., 1995; Faust and Williams, 1996), and it depends on the particular phase if it is stabilized or destabilized by hydrogen bonds. In this context, a further important aspect has to be taken into account. Similarities in charge and ionic radius facilitate the incorporation of halogen anions, particularly F^- and Cl^-, for the $(OH)^-$ groups in many hydrous minerals. Common examples for the (F,OH) substitution are topaz, clinohumite, chondrodite, micas, and serpentines, and amphiboles for the substitution of Cl. Generally, most hydrous minerals form solid solutions between the OH and the F or Cl endmembers. The incorporation of halogen anions shifts the stability fields and has significant effects on physical and crystal chemical properties such as compressibility, symmetry, and structural order–disorder. The fate of hydrous minerals in subduction processes can only be understood and modeled properly if such effects are considered. However, many of these minerals display a wide chemical diversity due to their relatively complex crystal structures, e.g., clay minerals, micas, and amphiboles. Because of this, the discrete influence of halogen/OH substitution on crystal chemical properties is masked by other effects and thus not well known. Therefore, hydrous phases in chemically relatively simple systems such as $Al_2O_3 - SiO_2 - H_2O$ (ASH) and $MgO - SiO_2 - H_2O$ (MSH) hold great potential as model phases to study volatile transport in subduction zones in dependence of pressure, temperature, and addition of other components.

In this thesis, the hydrogen bond geometry in topaz was investigated as a function of OH concentration and temperature. Topaz, $Al_2SiO_4(F, OH)_2$, is very well suited as model phase to study the influence of F/OH substitution on crystal chemical properties. This is because topaz has a fairly simple crystal structure and is also quite common in nature, where it mainly occurs in near-surface environments, i.e., in rhyolites, granites and particularly in associated pegmatites and hydrothermal deposits (e.g., Ribbe, 1982; Barton, 1982). In the following, the new insight to the hydrogen bond geometry of topaz is presented in the context of other studies, along with speculations on the possible generalization of these results.

2.2.2 Hydrogen bond geometry in topaz

Topaz is an orthosilicate. It's crystal structure is composed of edge-sharing alumina octahedra connected by isolated silica tetrahedra. Fluorine and OH are statistically distributed over the same crystallographic position (e.g., Zemann et al., 1979), which is one corner position of the Al octahedra. Crystal structural and spectroscopic investigations show that the OH group resides in a cavity, which is aligned in the (010) plane and inclined to the c axis by about 35° (e.g., Gebert and Zemann, 1965; Shinoda and Aikawa, 1997; Libowitzky and Beran, 2006). Topaz-OH, the fully hydrated endmember, has two distinct OH positions (Northrup et al., 1994), while the structure formed by isolated Si tetrahedra connecting Al octahedra chains remains the same. The space group of topaz is independent of the OH concentration, but varies with temperature (see below). At ambient conditions, topaz has space group $Pbn2_1$ (Chapter 5 and 6).

The OH concentration, in the following given as fraction X_{OH} = OH/(OH + F) on a molar basis, has a significant influence on a wide range of properties such as the lattice parameters, the shape of the IR spectrum, the piezo- and pyroelectricity, and the phase stability. The OH content ranges between 0 and 0.3 in the majority of the natural topazes, i.e., those from near-surface environments. However, topaz found in low-temperature, high- to ultrahigh-pressure metamorphic rocks displayed OH concentrations of up to 0.55 (Theye, 1988; Zhang et al., 2002). Experimental studies suggest that the solid solution series between topaz-F and topaz-OH may be complete, depending on the P–T–X conditions (Wunder et al., 1999). The OH endmember, albeit only known from experimental studies, is a high-pressure high-temperature phase with a large stability field (Fig. 2.4). One consequence of the substitution of the slightly larger hydroxyl anion into the crystal structure is the increase in the lattice parameters. Several different but linear correlations between unit cell parameters and OH fraction are reported in the literature (e.g., Ribbe and Rosenberg, 1971; Wunder et al., 1999; Alberico et al., 2003). In contrast, the results from an autocorrelation analysis in this study show that the change in structural parameters with increasing OH content is continuous, but non-linear (Chapter 6). However, the total uncertainty of the linear correlations is less than 8%, and even smaller at X_{OH} between 0 and 0.4. Thus, fairly reliable F or OH concentrations can be obtained from the unit cell parameters, if these linear relationships are applied.

Short-range ordering of F and OH in the crystal structure

A crucial result from the investigation of topaz in this thesis is the importance of short-range ordering in the crystal structure on crystal chemical properties. All IR spectra of topaz samples, which cover nearly the complete range of the (F,OH)-solid solution, show two distinguishable OH bands. One the one hand, there is the typical sharp band at about 3650 cm^{-1}, on the other hand a less distinct OH band as shoulder on the low-energy wing of the sharp band. The occurrence of two OH bands cannot be explained by diffraction studies, which do not distinguish between F and OH occupation of the respective crystallographic position, i.e., one corner of the Al octahedra. However, IR spectroscopy is very sensitive to differences in the local environment of the investigated species, in this case OH, and in the bond arrangement such as differing H bond acceptors, whereas diffraction methods

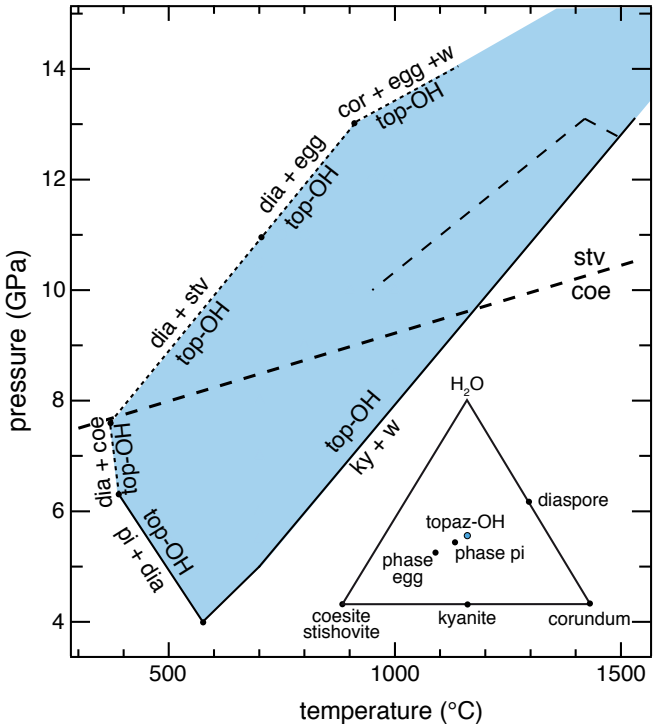

Figure 2.4: The ASH system at high pressure and temperature. The estimated stability field of topaz-OH is colored in light blue. The insert shows the chemography of the high-pressure phases. Equilibria top-OH = ky + w, top-OH = pi + dia and top-OH = dia + coe from Wunder et al. (1993), top-OH = dia + stv, top-OH = dia + egg derived from the CASH system (Schmidt, 1995), and top-OH = cor + egg + w from Ono (1999). Coesite–stishovite transition from Akaogi et al. (1995). Abbreviations: top-OH = topaz-OH, ky = kyanite, w = water, pi = phase pi ($Al_3Si_2O_7(OH)_3$), dia = diaspore, coe = coesite, stv = stishovite, cor = corundum, and egg = phase egg ($AlSiO_3(OH)$).

provide only information on the long-range order, i.e., averages over many unit cells. Thus, it is reasonable to conclude that the local surrounding, i.e., short-range ordering of F and OH, is responsible for the occurrence of two distinct OH bands in topaz. This short-range ordering is possible because there are two adjacent Al octahedra corner positions occupied by F or OH in the same cavity (Fig. 2.5), which permits interaction. According to Zemann et al. (1979), no preferred ordering of F and OH occurs in the crystal structure of topaz. Thus, the occupation of two adjacent F/OH sites is statistical and three cases are possible, which are illustrated in Fig. 2.5: (1) two fluorine atoms, (2) one fluorine atom and one hydroxyl group, and (3) two hydroxyl groups. Hence, there are two different surroundings of the absorbing OH groups, which causes two distinct bands in the IR spectra. The frequency of occurrence of each case depends only on the OH concentration and can be predicted by probability calculations. Based on that, it is most likely that the typical sharp band originates from case two and that the shoulder is related to two adjacent OH groups (case three). This is supported by the excellent agreement of the ratio of the calculated

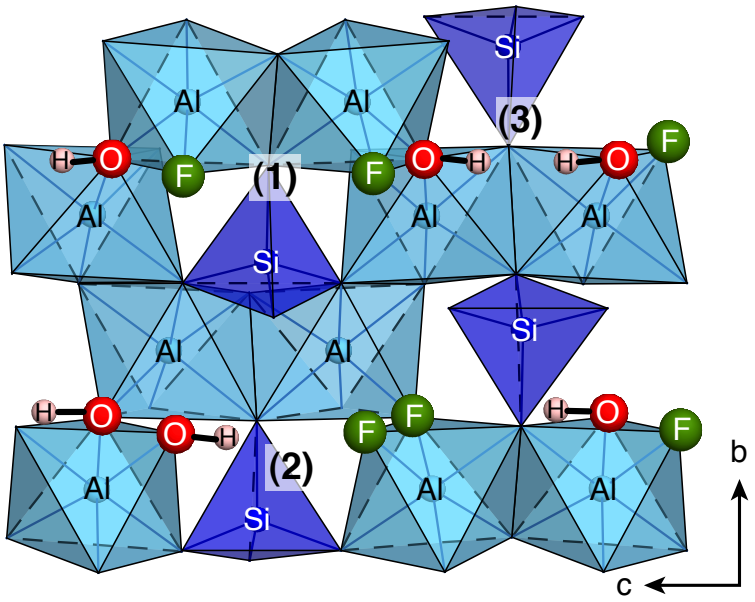

Figure 2.5: Crystal structure of topaz with highlighted F/OH positions. Numbers in parentheses designate the three possible cases of adjacent corner occupation, i.e., case (1): F···F, case (2): OH···F (2), and case (3): OH···OH (slightly modified after Fig. 6.7, chapter 6).

probabilities of cases (2) and (3) and the ratio of the integrated absorbances of the two OH bands in the IR spectra.

The short-range ordering of F and OH does not only affect the OH stretching bands in the IR spectra, but also the symmetry of topaz crystals and thus in turn probably also other spectroscopic features. Generally, topaz is reported to crystallize in space group *Pbnm* based on structural refinements of neutron or X-ray diffraction data. These refinements do not distinguish between F or OH occupation of the Al octahedra corners. However, short-range ordering of F and OH is essential to explain the occurrence of two OH stretching bands in the IR spectra and can thus not be neglected. With exception of both endmembers of the (F,OH)-solid solution series, the consideration of short-range ordering results locally in the loss of the mirror plane (001) and, therefore, in the reduction of the local symmetry from space group *Pbnm* to $Pbn2_1$. This local symmetry reduction has further implications for the crystal chemical properties of topaz such as piezo- and pyroelectricity. Space group *Pbnm* is centrosymmetric, whereas $Pbn2_1$ is non-centrosymmetric. Piezo- and pyroelectricity are only allowed in non-centrosymmetric space groups and were, indeed, observed experimentally in topaz (Hoover, 1993). The occurrence of both effects was considered as anomalous in that study. The here presented results suggest that this is not the case, but a consequence of local ordering of F and OH in the crystal structure of topaz.

The effect of short-range ordering of F and OH on the increase in the lattice parameters with OH concentration is unknown. It is tempting to speculate that the non-linear behavior

of the c lattice parameter above $X_{OH} \simeq 0.4$, which controls the volume increase, is related to OH$\cdots$OH ordering as the probability for two adjacent OH groups is 1/3 at $X_{OH} = 0.4$. Likewise, the effect of local ordering on the phase stability of topaz is unexplored. It can only be stated that F-rich topaz with little local ordering is a typical low-pressure mineral. Topaz from high-pressure rocks exhibits higher OH concentrations and thus, more OH$\cdots$OH short-range ordering. The OH endmember is restricted to ultrahigh pressures and has a modified hydrogen bond geometry.

Temperature and pressure-dependent changes of the crystal structure

Understanding the behavior of hydrous minerals in subduction zones requires knowledge about their properties at both high pressure and temperature. However, in-situ determination of crystal chemical properties of minerals at such conditions is very difficult. Therefore, minerals are commonly investigated in dependence of only one parameter, either pressure or temperature.

Temperature and pressure have opposite effects on the crystal structure. In general, increasing temperature increases the thermal vibration of the atoms, and the interatomic distances become larger, which leads to volume expansion. In contrast, increasing pressure results in volume contraction, and usually in shortening of the interatomic distances. It has often been proposed that low temperature and high pressure induce similar effects on crystal chemical properties, so that investigation of one parameter is sufficient to describe the complete pressure and temperature behavior of the mineral. However, this assumption is not always correct as shown in this thesis based on the investigations of topaz. Especially local symmetry changes, which originate from order–disorder of hydrogen atoms, are normally not detectable in studies, in which only pressure is varied.

Fluorine-bearing topaz as well as topaz-OH undergo temperature-dependent phase transitions, which can be revealed from autocorrelation analyses of the IR spectra. In both cases, the space group changes at low temperature from *P1* to $Pbn2_1$ and at high temperature from $Pbn2_1$ to *Pbnm*. For the first transition, the temperature of the investigated (F,OH)-bearing topazes (X_{OH} = 0.075 and 0.23) is about -135 °C (Chapter 6), whereas the transition in the OH endmember occurs at about -160 °C (Chapter 5). However, it is still unknown if the phase transition temperatures depend on the OH concentration. The low-temperature transition in (F,OH)-bearing topaz and topaz-OH is related to hydrogen ordering in distinct positions. It is assumed for (F,OH)-bearing topaz that the low-temperature contraction of the crystal structure results in a too close approach of two adjacent OH groups. Both positions cannot be simultaneously occupied by two OH groups in the "normal" geometry due to the so-called proton–proton repulsion (e.g., Barton, 1982). This presumably causes a small rotation of both OH groups in opposite direction, which results in an enlarged interatomic distance. As a consequence, the new hydrogen positions are non-equivalent, which leads to a local symmetry reduction of the space group to *P1*.
In the case of topaz-OH, ab-initio calculations predict four non-equivalent hydrogen positions in close proximity (Churakov and Wunder, 2004). At low temperature, proton motion is strongly restricted, so that the hydrogen atoms are practically fixed at these

distinct positions. The increase of the thermal vibrations with temperature permits a dynamical exchange between the four positions. Therefore, the protons in two closely adjacent positions switch so fast above -160 °C that these two positions practically merge to one. Overall, the "fixation" of the protons in four positions at low temperature causes a local symmetry reduction to space group *P1*.

The high-temperature transitions are also order–disorder transitions. In topaz-OH, this transition involves again only hydrogen ordering in the crystal structure. Above 400 °C, proton mobility is so enhanced that the protons switch freely between the four positions. On average, this behavior results in the formation of a (001) mirror plane, which changes the space group from $Pbn2_1$ to *Pbnm*. In contrast, the high-temperature transition in (F,OH)-bearing topaz is caused by changes of the local F···F and OH···OH ordering in the crystal structure. At temperatures above 160 °C, F and OH are on average completely disordered, which likewise results in a symmetry change from $Pbn2_1$ to *Pbnm*.

Infrared spectra of topaz at room temperature and pressures between 0 and 30 GPa were determined by Bradbury and Williams (2003) and Komatsu et al. (2005). The OH stretching bands shifted to higher wavenumbers, but a phase transition was not observed. This may simply be due to the fact that these studies did not use autocorrelation analysis, which is the most sensitive tool to detect phase transitions. Komatsu et al. (2005) also investigated the pressure-dependent behavior of topaz-OH by Raman spectroscopy. In this case, differences between pressure- and temperature-induced effects on the crystal chemical properties become apparent. Increasing pressure causes a shift of the two OH stretching bands of topaz-OH to lower wavenumbers, similar to the behavior of (F,OH)-bearing topaz with increasing pressure or decreasing temperature. This is coupled with a significant decrease of the intensity of the OH band at lower wavenumbers, along with broadening of both bands. In contrast, the investigation of the temperature dependence from this thesis shows that both bands split symmetrically into a total of four bands at temperatures below -160 °C. Moreover, the OH band at lower energy shifts towards lower wavenumbers with decreasing temperature, whereas the one at higher wavenumbers does not change it's position.

There may be several reasons why temperature and pressure have a different influence on the crystal structure of topaz-OH, but a similar effect on that of (F,OH)-bearing topaz. However, it is very likely that this is related to the differences in the hydrogen bond geometry. In (F,OH)-bearing topaz at low temperature, the OH groups presumably rotate slightly to increase the interatomic distance, which leads to a local symmetry reduction. However, the protons do not switch between different positions in the crystal structure. On the other hand, the hydrogen atoms in topaz-OH switch permanently between the allowed positions. Low temperature inhibits this behavior and traps the protons in particular positions. Upon increasing pressure at room temperature, (F,OH)-bearing topaz shows a similar behavior to that at decreasing temperature. This is because the shift of the OH stretching bands is in both cases related to the contraction of the crystal structure. In topaz-OH, pressure also contracts the crystal structure, but does not affect proton motion as this originates from the thermal energy of the hydrogen atoms.

2.2.3 Implications for other hydrous halogen-bearing minerals

Topaz is much more famous and important as beautiful gem stone than as water carrier in subduction zones due to it's low abundance in nature. However, it is a very suitable model phase to study volatile incorporation as reasoned previously. Therefore, the results from this thesis on it's hydrogen bond geometry summarized in the preceding paragraphs may well have implications for other hydrous halogen-bearing minerals.

Local ordering of hydroxyl groups and halogen anions possibly occurs in all hydrous minerals with this substitution. This is because the short-range ordering bases only on the statistical distribution of both species is the same site in the crystal structure. In topaz, short-range ordering affects a wide range of crystal chemical and physical properties and is essential for the understanding of the behavior under pressure and temperature. In analogy, this may also be the case for other hydrous halogen-bearing minerals. For example, minerals of the humite group, in particular chondrodite, $Mg_5(SiO_4)_2(F,OH)_2$, and clinohumite, $Mg_9(SiO_4)_4(F,OH)_2$, form complete (F,OH)-solid solution series similar to topaz, with F and OH statistically distributed over the same position in the crystal structure. Likewise, the possible occurrence of proton–proton repulsion in humite minerals and the influence on the occupation of H positions has been controversially discussed in a series of papers (e.g., Williams, 1992; Lin et al., 1999; Lager et al., 2001; Friedrich et al., 2001). Lager et al. (2001) proposed that two hydrogen atoms are never in close proximity on a local scale because of proton disorder. The idea of short H distances with the resulting strong repulsion originated from the application of diffraction methods, which, however, determine only average structures. Therefore, one can conclude that the local environment of the hydrogen atoms and their possible local ordering play also an important role in minerals of the humite group. As now demonstrated for topaz in this thesis, Friedrich et al. (2001) suggested that the hydrogen atoms may become ordered in the crystal structure at low temperature, which leads to a symmetry reduction. This suggestion is based on their investigations on the crystal structures of natural chondrodite and clinohumite at temperatures to -253 °C, in which they observed a few weak reflections, which could not be ascribed to the Renninger effect (double diffraction effect).

Several studies concentrated on the influence of F/OH substitution on mineral stability. Chondrodite and clinohumite are stable over a wide range of pressure and temperature, from 2 to about 10 GPa and 600 to 1100 °C (Harlow, 2002). The incorporation of small amounts of fluorine appears to increase the stability of both minerals towards higher pressure compared to that of the OH endmembers (Stalder and Ulmer, 2001; Harlow, 2002). On the other hand, the incorporated fluorine content decreases significantly with increasing pressure (Stalder and Ulmer, 2001). These observations are in line with those for topaz.

Based on the observations on two model systems, ASH and MSH, it can be reasonably assumed that local ordering of hydroxyl groups and halogens occurs in almost all hydrous halogen-bearing minerals and that this ordering affects their crystal chemical and physical properties. Moreover, incorporation of halogens appears to influence mineral stabilities and therefore the recycling of water into the Earth's mantle.

In summary, the properties of hydrous halogen-bearing minerals are not only determined by their halogen content, but also by local phenomena in the crystal structure such

as ordering/disordering. These properties may be strongly influenced by pressure and temperature. Therefore, detailed knowledge on the variation of crystal chemical properties with pressure, temperature, composition, and local structural ordering is required to completely understand and to model the behavior of volatile-bearing minerals during subduction processes, which represent the almost exclusive means of volatile transport into the Earth's mantle.

2.3 References

Abbott, R.N. Jr. (1990) Topaz: energy calculations bearing on the location of hydrogen. Canadian Mineralogist, 28, 827-833.

Akaogi, M., Yusa, H., Shiraishi, K., and Suzuki, T. (1995) Thermodynamic properties of α-quartz, coesite, and stishovite and equilibrium phase relations at high pressures and high temperatures. Journal of Geophysical Research, 100, 22337-22347.

Alt, J.C., Honnorez, J., Laverne, C., and Emmermann, R. (1986) Hydrothermal alteration of a 1 km section through the upper oceanic crust, Deep Sea Drilling Project Hole 504B: mineralogy, chemistry and evolution of seawater-basalt interactions. Journal of Geophysical Research, 91(B10), 10309-10335.

Andersen, T., and Neumann, E-R. (2001) Fluid inclusions in mantle xenoliths. Lithos, 55, 301-320.

Andersen, T., Burke, E.A.J., and Neumann, E-R. (1995) Nitrogen-rich fluid in the upper mantle; fluid inclusions in spinel dunite from Lanzarote, Canary Islands. Contributions to Mineralogy and Petrology, 120, 20-28.

Barton, M.D. (1982) The thermodynamic properties of topaz solid solution and some petrological applications. American Mineralogist, 67, 956-974.

Baur, W.H., and Wlotzka, F. (1974) Nitrogen. In: Wedepohl, K.H. (Ed.), Handbook of geochemistry. Springer, Berlin.

Beaumont, V., and Robert, F. (1999) Nitrogen isotope ratios of kerogens in Precambrian cherts: a record of the evolution of atmosphere chemistry? Precambrian Research, 96, 63-82.

Bebout G.E., and Fogel, M.L. (1992) Nitrogen-isotope compositions of metasedimentary rocks in the Catalina schists, California: Implications for metamorphic devolatilization history. Geochimica et Cosmochimica Acta, 56, 2839-2849.

Bindi, L., Safonov, O.G., Yapaskurt, V.O., Perchuk, L.L., and Menchetti, S. (2003) Ultrapotassic clinopyroxene from the Kumdy-Kol microdiamond mine, Kokchetav Complex, Kazakhstan: Occurrence, composition and crystal-chemical characterization. American Mineralogist, 88, 464-468.

Bos, A., Duit, W., Van der Eerden, A.M.J., and Jansen, J.B.H. (1988) Nitrogen storage in biotite: an experimental study of ammonium and potassium partitioning between 1M-phlogopite and vapor at 2 kb. Geochimica et Cosmochimica Acta, 52, 1275-1283.

Boyd, S.R., Pillinger, C.T., Milledge, H.J., Mendelssohn, M.J., and Seal, M. (1992) C and N isotopic composition and the infrared absorption spectra of coated diamonds: evidence for the regional uniformity of CO_2–H_2O rich fluids in lithospheric mantle. Earth and Planetary Science Letters, 109, 633-644.

Boyd, S.R., Hall, A., and Pillinger, C.T. (1993) The measurement of $\delta^{15}N$ in crustal rocks by static vacuum mass spectrometry: Application to the origin of the ammonium in the Cornubian batholith, south-west England. Geochimica et Cosmochimica Acta, 57, 1339-1347.

Bradbury, S.E., and Williams, Q. (2003) Contrasting bonding behavior of two hydroxyl-bearing metamorphic minerals under pressure: Clinozoisite and topaz. American Mineralogist, 88, 1460-1470.

Busigny, V., Cartigny, P., Philippot, P., Ader, M., and Javoy, M. (2003) Massive recycling of nitrogen and other fluid-mobile elements (K, Rb, Cs, H) in a cold slab environment: evidence from HP to UHP oceanic metasediments of the Schistes Lustrés nappe (western Alps, Europe). Earth and Planetary Science Letters, 215, 27-42.

Busigny, V., Laverne, C., and Bonifacie, M. (2005) Nitrogen content and isotopic composition of oceanic crust at a superfast spreading ridge: A profile in alterated basalts from ODP Site 1256, Leg 206. Geochemistry, Geophysics, Geosystems, 6, Q12O01, doi:10.1029/2005GC001020.

Cartigny, P. (2005) Stable isotopes and the origin of diamond. Elements, 1, 79-84.

Cartigny, P., and Ader, M. (2003) A comment on "The nitrogen record of crust–mantle interaction and mantle convection from Archean to Present" by B. Marty and N. Dauphas [Earth Planet. Sci. Lett. 206(2003) 397–410]. Earth and Planetary Science Letters 216, 425-432.

Cartigny, P., Boyd, S.R., Harris, J.W., and Javoy, M. (1997) Diamonds and the isotopic composition of mantle nitrogen. Terra Nova, 9, 175-179.

Cartigny, P., Harris, J.W., Phillips, D., Girard, M., and Javoy, M. (1998) Subduction-related diamonds? – The evidence for a mantle-derived origin from coupled $\delta^{13}C$–$\delta^{15}N$ determinations. Chemical Geology, 147, 147-159.

Cartigny, P., Jendrzejewski, N., Pineau, F., Petit, E., and Javoy, M. (2001a) Volatile (C, N, Ar) variability in MORB and the respective roles of mantle source heterogeneity and degassing: the case of the Southwest Indian Ridge. Earth and Planetary Science Letters, 194, 241-257.

Cartigny,P., De Corte, K., Shatsky, V.S., Ader, M., De Paepe, P., Sobolev, N.V., and Javoy, M. (2001b) The origin and formation of metamorphic microdiamonds from

the Kokchetav massif, Kazakhstan: a nitrogen and carbon isotopic study. Chemical Geology, 176, 265-281.

Catti, M., Ferraris, G., Hull, S., and Pavese, A. (1995) Static compression and H disorder in Brucite, $Mg(OH)_2$, to 11 GPa: a powder neutron diffraction study. Physics and Chemistry of Minerals, 22, 200-206.

Churakov, S.V., and Gottschalk, M. (2003a) Perturbation theory based equation of state for polar molecular fluids: I. Pure fluids. Geochimica et Cosmochimica Acta, 67, 2397-2414.

Churakov, S.V., and Gottschalk, M. (2003b) Perturbation theory based equation of state for polar molecular fluids: II. Fluid mixtures. Geochimica et Cosmochimica Acta, 67, 2415-2425.

Churakov, S.V., and Wunder, B. (2004) Ab initio calculations of the proton location in topaz-OH, $Al_2SiO_4(OH)_2$. Physics and Chemistry of Minerals, 31, 131-141.

Delwiche, C.C. (1970) The nitrogen cycle. Scientific American, 223,137-146.

Devol, A.H. (2003) The nitrogen cycle - Solution to a marine mystery. Nature, 422, 575-576.

Dobrzhinetskaya, L., Wirth, R., Yang, J., Green, H., Weber, P., and Hutcheon, I. (2008) Boron and Nitrogen in ultrahigh-pressure terrestrial rocks. Geochimica et Cosmochimica Acta, 72, A221.

Domanik, K.J., and Holloway, J.R. (1996) The stability and composition of phengitic muscovite and associated phases from 5.5 to 11 GPa: implications for deeply subducted sediments. Geochimica et Cosmochimica Acta, 60, 4133-4154.

Elkins, L.J., Fischer, T.P., Hilton, D.R., Sharp, Z.D., McKnight, S., and Walker, J. (2006) Tracing nitrogen in volcanic and geothermal volatiles from the Nicaraguan volcanic front. Geochimica et Cosmochimica Acta, 70, 5215-5235.

Exley, R.A., Boyd, S.R., Mattey, D.P., and Pillinger, C.T. (1986) Nitrogen isotope geochemistry of basaltic glasses: Implications for mantle degassing and structure? Earth and Planetary Science Letters, 81, 163-174.

Fasshauer, D.W., Chatterjee, N.D., and Marler, B. (1997) Synthesis, structure, thermodynamic properties, and stability relations of K-cymrite, $K[AlSi_3O_8] \cdot H_2O$. Physics and Chemistry of Minerals, 24, 455-462.

Faust, J., and Williams, Q. (1996) Infrared spectra of phase B at high hydroxyl bonding under compression. Geophysical Research Letters, 23, 427-430.

Fischer, T.P., Hilton, D.R., Zimmer, M.M., Shaw, A.M., Sharp, Z.D., and Walker, J.A. (2002) Subduction and recycling of nitrogen along the Central American margin, Science, 297, 1154-1157.

Friedrich, A., Lager, G.A., Kunz, M., Chakoumakos, B.C., Smyth, J.R., and Schultz, A.J. (2001) Temperature-dependent single-crystal neutron diffraction study of natural chondrodite and clinohumites. American Mineralogist, 86, 981-989.

Frost, D.J., and McCammon, C.A. (2008) The redox state of Earth's mantle. Annual Review of Earth and Planetary Sciences, 36, 389-420.

Galloway, J.N. (2004) The global nitrogen cycle. In: Schlesinger, W.H., (Eds.), Treatise on geochemistry, Biogeochemistry, vol. 8, pp. 557-583.

Gebert, W., and Zemann, J. (1965) Messungen des Ultrarot-Pleochroismus von Mineralen. III. Der Pleochroismus der OH-Streckfrequenz in Topas. Neues Jahrbuch der Mineralogie, Monatshefte, 1965, 380-384.

Haendel, D., Mühle, K., Nitzsche, H-M., Stiehl, G., and Wand, G. (1986) Isotopic variations of the fixed nitrogen in metamorphic rocks. Geochimica et Cosmochimica Acta, 50, 749-758.

Hallam, M., and Eugster, H.P. (1976) Ammonium silicate stability relations. Contributions to Mineralogy and Petrology, 57, 227-244.

Harlow, G.E. (1997) K in clinopyroxene at high pressure and temperature: An experimental study. American Mineralogist, 82, 259-269.

Harlow, G.E. (2002) Diopside + F-rich phlogopite at high P and T: Systematics, crystal chemistry and the stability of $KMgF_3$, clinohumite and chondrodite. Geological Materials Research, 4(3), 1-28.

Harlow, G.E., and Davies R.M. (2004) Status report on stability of K-rich phases at mantle conditions. Lithos, 77, 647-653.

Hilton, D.R., Fischer, T.P., and Marty, B. (2002) Noble gases and volatile recycling at subduction zones. In: Porcelli, D.P., Ballentine, C.J., and Wieler, R., (Eds.), Noble Gases – In Geochemistry and Cosmochemistry. Reviews in Mineralogy and Geochemistry, vol. 47, Mineralogical Society of America and Geochemical Society, Chantilly, Virginia, pp. 319-370.

Hoefs, J. (2009) Stable isotope geochemistry. 6th edn, Springer, Berlin.

Hoover, B. (1993) Topaz. Butterworths-Heinemann, Oxford, p.40.

Huraiova, M., Dubessy, J., and Konecny, P. (1991) Composition and oxidation state of upper mantle fluids from southern Slovakia. Plinius, 5, 110-111.

Jarrard, R.D. (2003) Subduction fluxes of water, carbon dioxide, chlorine, and potassium. Geochemistry, Geophysics, Geosystems, 4(5), 8905, doi: 10.1029/2002GC000392.

Javoy, M. (1997) The major volatile elements of the Earth: Their origin, behavior, and fate. Geophysical Research Letters, 24, 177-180.

Javoy, M. (1998) The birth of the Earth's atmosphere: the behaviour and fate of its major elements. Chemical Geology, 147, 11-25.

Javoy, M., and Pineau, F. (1991) The volatile record of a popping rock from the Mid-Atlantic Ridge at 14°N: chemical and isotopic composition of gas trapped in vesicles. Earth and Planetary Sciences Letters, 107, 598-611.

Javoy, M., Pineau, F., and Demaiffe, D. (1984) Nitrogen and carbon isotopic composition in the diamonds of Mbuji Mayi (Zaire). Earth and Planetary Sciences Letters, 68, 399-412.

Javoy, M., Pineau, F., and Delorme, H. (1986) Carbon and nitrogen isotopes in the mantle. Chemical Geology, 57, 41-62.

Johnson, E.A., (2006) Water in nominally anhydrous crustal minerals: speciation, concentration, and geologic significance. In: Keppler, H., and Smyth, J., (Eds.) Water in nominally anhydous minerals. Reviews in Mineralogy and Geochemistry, vol. 62, Mineralogical Society of America and Geochemical Society, Chantilly, Virginia, pp. 117-154.

Komatsu, K., Kagi, H., Okada, T., Kuribayashi, T., Parise, J.B., and Kudoh, Y. (2005) Pressure dependence of the OH-stretching mode in F-rich natural topaz and topaz-OH. American Mineralogist, 90, 266-270.

Konzett, J., and Fei, Y. (2000) Transport and storage of potassium in the Earth's upper mantle and transition zone: an experimental study to 23 GPa in simplified and natural bulk compositions. Journal of Petrology, 41, 583-603.

Lager, G.A., Ulmer, P., Miletich, R., and Marshall, W.G. (2001) O–D$\cdots$O bond geometry in OD-chondrodite. American Mineralogist, 86, 176-180.

Li, L., Bebout, G.E., and Idleman, B.D. (2007) Nitrogen concentration and δ^{15}N of alterated oceanic crust obtained on ODP Legs 129 and 185: Insights into alteration-related nitrogen enrichment and the nitrogen subduction budget. Geochimica et Cosmochimica Acta, 71, 2344-2360.

Libourel, G., Marty, B., and Humbert, F. (2003) Nitrogen solubility in basaltic melt. Part I. Effect of oxygen fugacity. Geochimica et Cosmochimica Acta, 67, 4123-4135.

Libowitzky, E., and Beran, A. (2006) The structure of hydrous species in nominally anhydrous minerals: information from polarized IR spectroscopy. In: Keppler, H., and Smyth, J.R. (Eds.) Water in nominally anhydrous minerals, Reviews in Mineralogy and Geochemistry, vol. 62, pp. 29-52.

Lin, C.C., Liu, L.G., and Irifune, T. (1999) High-pressure Raman spectroscopic study of chondrodite. Physics and Chemistry of Minerals, 26, 226-233.

Marty, B. (1995) Nitrogen content of the mantle inferred from N_2-Ar correlation in oceanic basalts. Nature, 377, 326-329.

Marty, B., and Humbert, F. (1997) Nitrogen and argon isotopes in oceanic basalts. Earth and Planetary Science Letters, 152, 101-112.

Marty, B., and Dauphas, N. (2003) - The nitrogen record of crust–mantle interaction and mantle convection from Archean to Present. Earth and Planetary Science Letters, 206, 397-410.

Mingram, B., and Bräuer, K. (2001) Ammonium concentration and nitrogen isotope composition in metasedimentary rocks from different tectonometamorphic units of the European Variscan Belt. Geochimica et Cosmochimica Acta, 65, 273-287.

Mysen, B.O., Yamashita, S., and Chertkova, N. (2008) Solubility and solution mechanisms of NOH volatiles in silicate melts at high pressure and temperature – amine groups and hydrogen fugacity. American Mineralogist, 93, 1760-1770.

Northrup, P.A., Leinenweber, K., and Parise, J.B. (1994) The location of H in the high-pressure synthetic $Al_2SiO_4(OH)_2$ topaz analogue. American Mineralogist, 79, 401-404.

Ono, S. (1998) Stability limits of hydrous minerals in sediment and mid-ocean ridge basalt compositions: implications for water transport in subduction zones. Journal of Geophysical Research, 103,18253-18267.

Ono, S. (1999) High temperature stability limit of phase egg, $AlSiO_3(OH)$. Contributions to Mineralogy and Petrology, 137, 83-89.

Parise, J.B., Leinenweber, K., Weidner, D.J., Tan, K., and Von Dreele, R.B. (1994) Pressure-induced H bonding: Neutron diffraction study of brucite, $Mg(OD)_2$, to 9.3 GPa. American Mineralogist, 79, 193-196.

Pasteris, J.D. (1987) Fluid inclusions in mantle xenoliths. In: Nixon, P.H. (Ed.), Mantle xenoliths. Wiley, Chichester, 691-707.

Perchuk, L.L., Safonov, O.G., Yapaskurt, V.O., and Barton Jr., J.M. (2002) Crystal-melt equilibria involving potassium-bearing clinopyroxene as indicator of mantle-derived ultrahigh-potassic liquids: an analytical review. Lithos, 60, 89-111.

Pineau, F., and Javoy, M. (1994) Strong degassing at ridge crests: the behaviour of dissolved carbon and water in basalt glasses at 14°N, Mid-Atlantic ridge. Earth and Planetary Science Letters, 123, 179-198.

Pöter, B., Gottschalk, M., and Heinrich, W. (2004) Experimental determination of the ammonium partitioning among muscovite, K-feldspar, and aqueous chloride solutions. Lithos, 74, 67-90.

Pöter, B., Gottschalk, M., and Heinrich, W. (2007) Crystal-chemistry of synthetic K-feldspar—buddingtonite and muscovite—tobelite solid solutions. American Mineralogist, 92, 151-165.

Poli, S., and Schmidt, M. (2002) Petrology of subducted slabs. Annual Review of Earth and Planetary Sciences, 207-235.

Ribbe, P.H. (1982) Topaz. In: Ribbe, P.H. (Ed.), Orthosilicates. Reviews in Mineralogy, 2rd edn, pp. 215-230.

Roskosz, M., Mysen, B.O., and Cody, G.D. (2006) Dual speciation of nitrogen in silicate melts at high pressure and temperature: An experimental study. Geochimica et Cosmochimica Acta, 70, 2902-2918.

Rosman, K.J.R., and Taylor, P.D.P. (1998) Isotopic composition of the elements 1997. Pure and Applied Chemistry, 70, 217-235.

Sadofsky, S.J., and Bebout, G.E. (2000) Ammonium partitioning and nitrogen-isotope fractionation among coexisting micas during high-temperature fluid – rock interactions: examples from the new England Appalachians. Geochimica et Cosmochimica Acta, 64, 2835-2849.

Sadofsky, S.J., and Bebout, G.E. (2004) Nitrogen geochemistry of subducting sediments: New results from the Izu-Bonin-Mariana margin and insights regarding global nitrogen subduction. Geochemistry, Geophysics, Geosystems 5, Q03I15, doi:10.1029/2003GC000543.

Safonov, O.G., Litvin, Y.A., Perchuk, L.L., Bindi, L., and Menchetti, S. (2003) Phase relations of potassium-bearing clinopyroxene in the system $CaMgSi_2O_6 - KAlSi_2O_6$ at 7 GPa. Contributions to Mineralogy and Petrology, 146, 120-133.

Sano, Y., Takahata, N., Nishio, Y., Fischer, T.P., and Williams, S.N. (2001) Volcanic flux of nitrogen from the Earth. Chemical Geology, 171, 263-271.

Schmidt, M.W. (1995) Lawsonite: upper pressure stability and formation of higher density hydrous phases. American Mineralogist, 80, 1286-1292.

Schmidt, M.W., and Poli, S. (1998) Experimentally based water budgets for dehydrating slabs and consequences for arc magma generation. Earth and Planetary Science Letters, 163, 361-379.

Schmidt, M.W., and Poli, S. (2003) Generation of mobile components during subduction of oceanic crust. In: Holland, H.D., and Turekian, K.K., (Eds.) Treatise on Geochemistry, Vol. 3. pp. 567-591.

Schreyer, W. (1995) Ultradeep metamorphic rocks: retrospective viewpoint. Journal of Geophysical Research 100,8353-8366.

Shannon, R.D. (1976) Revised effective ionic radii and systematic studies of interatomic distances in halides and chalcogenides. Acta Crystallographica, A32, 751-767.

Shinoda, K., and Aikawa, N. (1997) IR active orientation of OH bending mode in topaz. Physics and Chemistry of Minerals, 24, 551-554.

Simakov, S.K. (1998) Redox state of upper mantle peridotites under the ancient cratons and its connection with diamond genesis. Geochimica et Cosmochimica Acta, 62, 1811-1820.

Stachel, T., Brey, G.P., and Harris, J.W. (2005) Inclusions in sublithospheric diamonds: glimpses of deep Earth. Elements, 1, 73-78.

Stalder, R., and Ulmer, P. (2001) Phase relations of a serpentine composition between 5 and 14 GPa: significance of clinohumite and phase E as water carriers into the transition zone. Contributions in Mineralogy and Petrology, 140, 670-679.

Staudigel, H., Furnes, H., Banerjee, N.R., Dilek, Y., and Muelenbachs, K. (2006) Microbes and volcanoes: a tale from the oceans, ophiolites, and greenstone belts. GSA today, 16, 4-10.

Sweeney, R.E., Liu, K.K., and Kaplan, I.R. (1978) Oceanic nitrogen isotopes and their uses in determining the source of sedimentary nitrogen. In: Robinson, B.W. (Ed.) Stable isotopes in the Earth Sciences. DSIR Bulletin on the International Conference of Stable Isotopes, 1976, New Zealand. pp. 599-604.

Theye, T. (1988) Aufsteigende Hochdruckmetamorphose in Sedimenten der Phyllit–Quarzit-Einheit Kretas und des Peloponnes. Ph.D. Thesis, University of Braunschweig.

Thomassot, E., Cartigny, P., Harris, J.W., and Vijoen, K.S. (2007) Methane-related diamond crystallization in the Earth's mantle: Stable isotope evidence from a single diamond-bearing xenolith. Earth and Planetary Science Letters, 257, 362-371.

Thompson, P., Parsons, I. Graham, C.M., and Jackson, B. (1998) The breakdown of potassium feldspar at high water pressures. Contributions to Mineralogy and Petrology, 130, 176-186.

Tolstikhin, I.N., and Marty, B. (1998) The evolution of terrestrial volatiles: a view from helium, neon, argon and nitrogen isotope modeling. Chemical Geology, 147, 27-52.

Trønnes, R.G. (2002) Stability range and decomposition of potassic richterite and phlogopite end members up to 15 GPa. Mineralogy and Petrology, 74, 129-148.

Tutti, F., Dubrovinsky, L.S., Saxena S.K., and Carlson S. (2001) Stability of $KAlSi_3O_8$ hollandite-type structure in the EarthÕs lower mantle conditions. Geophysical Research Letters, 28, 14, 2735-2738.

Urakawa, S., Kondo, T., Igawa, N., Shimomura, O., and Ohno, H. (1994) Synchrotron radiation study on the high-pressure and high-temperature phase relations of $KAlSi_3O_8$. Physics and Chemistry of Minerals, 21, 387-391.

Vitousek, P.M., Aber, J.D., Howarth, R.W., Likens, G.E., Matson, P.A., Schindler, D.W., Schlesinger, W.H., and Tilman, D.G. (1997) Human alteration of the global nitrogen cycle: sources and consequences. Ecological Applications, 7, 737-750.

Wada, E., Kadonaga, T., and Matsuo, S. (1975) ^{15}N abundances in nitrogen of naturally occurring substances and global assessment of denitrification from isotopic viewpoint. Geochemical Journal, 9, 139-148.

Wedepohl, K.H. (1978) Nitrogen. In: Handbook of Geochemistry, Elements H(1) to Al(13), Vol. II/1, Springer, Berlin.

Williams, L.B., Wilcoxon, B.R., Ferrell, R.E., and Sassen, R. (1992) Diagenesis of ammonium during hydrocarbon maturation and migration, Wilcox Group, Louisiana, USA. Applied Geochemistry, 7, 123-134.

Williams, Q. (1992) A vibrational spectroscopic study of hydrogen in high pressure mineral assemblages. In: Syono, Y., and Manghnani, M.H. (Eds.), High-pressure Research: Application to Earth and Planetary Sciences. Terra Publishing Company, pp. 289-296.

Wunder, B., Rubie, D.C., Ross II, C.D., Medenbach, O., Seifert, F., and Schreyer, W. (1993) Synthesis, stability, and properties of $Al_2SiO_4(OH)_2$: a fully hydrated analogue of topaz. American Mineralogist, 78, 285-297.

Wunder, B., Andrut, M., and Wirth, R. (1999) High-pressure synthesis and properties of OH-rich topaz. European Journal of Mineralogy, 11, 803-813.

Yagi, A., Suzuki, T., and Akaogi. M. (1994) High pressure transition in the system $KAlSi_3O_8 - NaAlSi_3O_8$. Physics and Chemistry of Minerals, 21, 12-17.

Yokochi, R., Marty, B., Chazot, G., and Burnard, P. (2009) Nitrogen in peridotite xenoliths: Lithophile behavior and magmatic isotope fractionation. Geochimica et Cosmochimica Acta, 73, 4843-4861.

Yong, W., Dachs, E., Withers, A.C., and Essene E.J. (2008) Heat capacity and phase equilibria of wadeite-type $K_2Si_4O_9$. Contributions to Mineralogy and Petrology, 155, 137-146.

Zemann, J., Zobetz, E., Heger, G., and Vollenke, H. (1979) Strukturbestimmung eines OH-reichen Topases. Österreichische Akademie der Wissenschaften, Mathematisch-Naturwissenschaftliche Klasse, 116, 145-147.

Zhang, R.Y., Liou, J.G., and Shu, J.F. (2002) Hydroxyl-rich topaz in high-pressure and ultrahigh-pressure kyanite quartzites, with retrograde woodhousite, from the Sulu terrane, eastern China. American Mineralogist, 87, 445-453.

Zhang, Y., and Zindler, A. (1993) Distribution and evolution of carbon and nitrogen in Earth. Earth and Planetary Science Letters, 117, 331-345.

Chapter 3

This chapter is published as

"High-pressure ammonium-bearing silicates: implications for nitrogen and hydrogen storage in the Earth's mantle"

by

Anke Watenphul, Bernd Wunder, and Wilhelm Heinrich

in

American Mineralogist, 94, 283-292, 2009.

High-pressure ammonium-bearing silicates: implications for nitrogen and hydrogen storage in the Earth's mantle

Anke Watenphul*, Bernd Wunder, and Wilhelm Heinrich

Deutsches GeoForschungsZentrum (GFZ), Telegrafenberg, 14473 Potsdam, Germany, Section 4.1 * E-mail: watenphul@gfz-potsdam.de

Abstract

The ammonium analogues of the high-pressure potassium-bearing silicate phases K-hollandite, K-Si-wadeite, K-cymrite, and phengite were synthesized in the system $(NH_4)_2O(-MgO) - Al_2O_3 - SiO_2 - H_2O$ (N(M)ASH) using multi-anvil and piston-cylinder equipment. Syntheses included NH_4-hollandite [$NH_4AlSi_3O_8$] at 12.3 GPa, 700 °C; NH_4-Si-wadeite [$(NH_4)_2Si_4O_9$] at 10 GPa, 700 °C; NH_4-cymrite [$NH_4AlSi_3O_8 \cdot H_2O$] at 7.8 GPa, 800 °C; and NH_4-phengite [$NH_4(Mg_{0.5}Al_{1.5})(Al_{0.5}Si_{3.5})O_{10}(OH)_2$] at 4 GPa, 700 °C. Run products were characterized by SEM, FTIR, and powder XRD with Rietveld refinements. Cell parameters of the new NH_4 end-members were determined to $a = 9.4234(9)$ Å, $c = 2.7244(3)$ Å, $V = 241.93(5)$ Å^3 (NH_4-hollandite); $a = 6.726(1)$ Å, $c = 9.502(3)$ Å, $V = 372.3(1)$ Å^3 (NH_4-Si-wadeite); $a = 5.3595(3)$ Å, $c = 7.835(1)$ Å, $V = 194.93(5)$ Å^3 (NH_4-cymrite). NH_4-phengite consisted of a mixture of $1M, 2M_1, 2M_2, 3T$, and $2Or$ polytypes. The most abundant polytype $2M_1$ has the cell dimensions $a = 5.2195(9)$ Å, $b = 9.049(3)$ Å, $c = 20.414(8)$ Å, $\beta = 95.65(3)°$, $V = 959.5(5)$ Å^3. All unit cell volumes are enlarged in comparison to the potassium analogues. Substitution of NH_4 for K does not cause changes in space group symmetry. NH_4 incorporation was confirmed by the appearance of NH_4 vibration modes ν_4 and ν_3 occurring in the ranges of 1397–1459 and 3223–3333 cm^{-1}, respectively.

Ammonium in eclogite facies metasediments is mainly bound in micas and concentrations may reach up to a few thousand ppm. It can be stored to greater depths in high-pressure potassium silicates during ongoing subduction. This possibly provides an important mechanism for nitrogen and hydrogen transport into the deeper mantle.

Keywords: Hollandite, wadeite, cymrite, phengite, ammonium, high-pressure synthesis, nitrogen cycle

3.2 Introduction

There is general agreement that nitrogen has been discharging for a long time from the Earth's mantle to the atmosphere through volcanic and hydrothermal activities (e.g., Javoy et al. 1986; Marty 1995; Sano et al. 2001). It is, however, controversially debated if a substantial amount of nitrogen is recycled during subduction processes. The discussion carried out in a series of recent papers mainly relies on the interpretation of the amount of molecular nitrogen and nitrogen isotope ratios measured in diamonds, mantle xenoliths, basalts, volcanic gases, hydrothermal fluids and the atmosphere, and on the question whether different nitrogen reservoirs in the mantle existed that may have been produced by input of isotopically different nitrogen from subducted sediments (e.g., Mohapatra and Murty 2000; Pinti et al. 2001; Fischer et al. 2002; Busigny et al. 2003; Cartigny and Ader 2003; Marty and Dauphas 2003a, 2003b; Mather et al. 2004; Fischer et al. 2005; Pitcairn et al. 2005; Thomassot et al. 2007).

Nitrogen in sediments has an organic origin. Under anoxic conditions at about 150 °C amino acids decompose to NH_4, which is incorporated into clay minerals, micas and feldspars substituting for K in small but significant amounts (Williams et al. 1992). It has been shown that during progressive contact and Barrovian-type metamorphism NH_4 is continuously released so that in high-grade rocks less than 10 % of the original nitrogen remains (Bebout and Fogel 1992; Bebout et al. 1999; Sadofsky and Bebout 2000; Mingram and Bräuer 2001; Pöter et al. 2004; Pitcairn et al. 2005). By contrast, Busigny et al. (2003) showed that in high-pressure low-temperature metapelites and metabasites from the Western Alps the entire nitrogen, up to 1600 ppm mainly bound as NH_4 in micas, remains in the rock up to at least 3 GPa. It would appear that there is no information about the fate of nitrogen in subducting slabs beyond that, and we do not know if and how nitrogen could be transported into the deeper mantle.

NH_4^+ has an ionic radius similar to Rb^+ (Shannon 1976) and replaces K^+ in silicates. One may reasonably assume that under slab conditions NH_4 persists in rocks as long as K-feldspar and high-pressure micas remain stable. In a status report on the stability of K-phases at mantle conditions, Harlow and Davies (2004) documented a number of K-bearing silicates that may form at higher pressure, mainly based on a summary of experimental results. In a wet system, K-feldspar may be replaced by K-cymrite [$K^{IV}Al^{IV}Si_3O_8 \cdot H_2O$] above about 2.5 GPa (Fasshauer et al. 1997; Fig. 3.1). K-cymrite is stable up to about 9 GPa, where it decomposes to K-hollandite [$K^{VI}Al^{Vl}Si_3O_8$] and fluid (Thompson et al. 1998). In a dry system, K-feldspar reacts to K-Si-wadeite [$K_2^{VI}Si^{IV}Si_3O_9$], (also termed Si-wadeite; Harlow and Davies 2004; Yong et al. 2008) + kyanite + coesite above 5 to 6.5 GPa, 400 to 1000 °C (Yagi et al. 1994; Urakawa et al. 1994). At pressures higher than about 9 GPa, the stability of K-Si-wadeite is limited by reactions that typically produce K-hollandite (Yong et al. 2008; Fig. 3.1). K-hollandite appears also as a reaction product of phengite breakdown in metapelitic and metabasaltic bulk compositions at pressures higher than 8 to 11 GPa, 750 to 900 °C (Domanik and Holloway 1996; Schmidt and Poli 1998; Poli and Schmidt 2002) and is probably stable up to 95 GPa, 2300 °C (Konzett and Fei 2000; Tutti et al. 2001). Therefore, K-hollandite is believed to be the main K-rich solid-phase reservoir for potassium through the transition zone to the lower mantle in silicate compositional systems because K-Al-bearing silicates react to yield K-hollandite with increasing pressure (Harlow

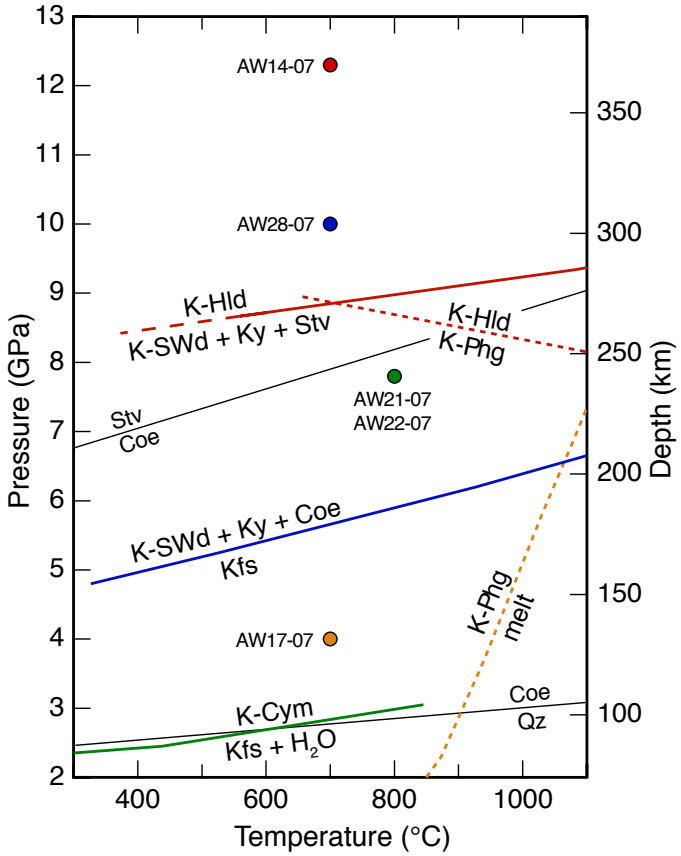

Figure 3.1: *P–T* plot showing stabilities of relevant high-pressure phases in the $K_2O - (MgO) - Al_2O_3 - SiO_2 - H_2O$ system. Data for K-cymrite from Fasshauer et al. (1997), for K-Si-wadeite and K-hollandite from Yong et al. (2008). Upper temperature and pressure stabilities of K-phengite determined for natural samples of metapelitic bulk compositions (Poli and Schmidt 2002), stabilities of SiO_2 polymorphs from Akaogi et al. (1995). Dots depict synthesis conditions of the NH_4-bearing analogues (Table 3.1). Abbreviations as in Table 3.1.

and Davies 2004, and references therein).

All high-pressure K-silicates constitute potential carriers of nitrogen and hydrogen into the deep mantle. The aim of this study is to show that the ammonium end-member analogues of hollandite [$NH_4AlSi_3O_8$], wadeite [$(NH_4)_2Si_4O_9$], cymrite [$NH_4AlSi_3O_8 \cdot H_2O$], and phengite [$NH_4(Mg_{0.5}Al_{1.5})(Al_{0.5}Si_{3.5})O_{10}(OH)_2$] can be synthesized stably at high pressure. Some of their crystal chemical properties are given, along with some speculations on possible transport of nitrogen and hydrogen to greater depths of the Earth.

3.3 Experimental and analytical techniques

3.3.1 Experimental procedures

There are some inherent difficulties in synthesizing NH_4-bearing minerals at high pressure. Experiments performed in multi-anvil modules routinely apply heated gels as starting materials. This is impossible in the case of ammonium because it rapidly evaporates during heating. For the synthesis of NH_4-hollandite, NH_4-Si-wadeite, and NH_4-cymrite we therefore used well-characterized, hydrothermally pre-synthesized buddingtonite, $[NH_4AlSi_3O_8]$, the NH_4-analogue of sanidine (Harlov et al. 2001a; Pöter et al. 2007) as starting solid. As stabilizing NH_4-phases requires some NH_3/NH_4^+-gas pressure we mainly used a wet system for runs by adding an NH_4OH solution in excess, only run AW22-07 used nominally dry buddingtonite as starting material, but a small amount of water absorption on the sample surface could not be avoided during sample preparation. This produces the required partial pressure of ammonia and keeps the hydrogen fugacity sufficiently high, i.e., the redox conditions reducing, at least as long as the H–N–O fluid provides sufficient hydrogen at given P and T. However, with our setup hydrogen loss from the gold or platinum capsules cannot be completely prevented (see below). Hydrogen loss gradually shifts conditions towards more oxidizing. Molecular nitrogen, N_2, is increasingly produced, finally resulting in the complete decomposition of the ammonium-bearing phase. This behavior was demonstrated by the sliding reaction buddingtonite $[NH_4AlSi_3O_8] + O_2 \rightarrow Al_2SiO_5 + SiO_2 + N_2 + H_2O$ performed in long-run hydrothermal experiments (Harlov et al. 2001a). Run durations were therefore adapted to minimize overall hydrogen loss. For calculation of neutral fluid species and relevant equilibria in the H–N–O system at very high pressure see, e.g., Churakov and Gottschalk (2003a, b). Similarly, NH_4-phengite was synthesized from a SiO_2, γ-Al_2O_3 and MgO oxide mix with NH_4OH solution in excess. Proportions of oxides were according to a phengite composition of $[(NH_4)(Mg_{0.6}Al_{1.4})(Al_{0.4}Si_{3.6})O_{10}(OH)_2]$. The intended celadonite-component chosen here is about that determined by Melzer and Wunder (2000) for (K,Rb,Cs)-bearing phengites synthesized at identical P,T conditions. Solids and fluids were cold-welded either into Pt-capsules (run AW14-07; Table 3.1) or Au-capsules (runs AW28-07, AW21-07, AW22-07; Table 3.1) of 3 mm length, 2 mm outer diameter, and 0.2 mm wall thickness. In all but one experiment, a 25% NH_4OH-solution was given in excess to the solid starting material (Table 3.1). The exact amount of ammonium loaded into the capsules was unknown because of rapid evaporation of a small fraction of ammonia during welding.

Synthesis of NH_4-bearing phengite was performed in a piston-cylinder press. The high-pressure cell consisted of a steel furnace with rock salt and fired pyrophyllite as pressure media. Two Au-capsules of 10 mm length and 3 mm diameter were filled with about 16 mg of solid and fluid starting material and sealed using a plasma arc welder while partly immersed in an ice/water mixture. Pressure was calibrated according to the quartz–coesite transition. For this assembly, the estimated pressure uncertainty is approximately 1%. The temperature was monitored using a chromel-alumel thermocouple; the precision is around ± 2 °C. A detailed description of the press and the experimental method is given in Wunder (1998).

After the experiments the capsules were carefully separated from the assembly material. They were cleaned in an ultrasonic bath for 10 min in ethanol and carefully opened. To

Table 3.1. Starting material, experimental conditions and run products

Run no.	Starting material	P (GPa)	T (°C)	t (h)	Run products (wt%)
AW14-07	Buddingtonite + NH_4OH solution	12.3	700	6	NH_4-Hld (31), Stv (22), NH_4-SWd (17), OH-Top (8), Ky (21), Egg (< 1)
AW28-07	Buddingtonite + NH_4OH solution	10.0	700	24	NH_4-SWd (34), OH-Top (39), Stv (27)
AW21-07	Buddingtonite + NH_4OH solution	7.8	800	24	NH_4-Cym (70), Coe (23), Ky (7)
AW22-07	Buddingtonite (nominally dry)	7.8	800	24	NH_4-Cym (49), Coe (26), Ky (25)
AW17-07	Oxide mixture + NH_4OH solution	4.0	700	26	NH_4-Phg $2M_1$ (75), NH_4-Phg $3T$ (14), NH_4-Phg $2Or$ (4), NH_4-Phg $1M$ (< 1), NH_4-Phg $2M_2$ (< 1), Coe (6), Ky (tr)*

* Traces of kyanite only detected by EMP.
Abbreviations: Coe: coesite, Ky: kyanite, NH_4-Cym: NH_4-cymrite, NH_4-Hld: NH_4-hollandite, NH_4-Phg: NH_4-phengite, NH_4-SWd: NH_4-Si-wadeite, OH-Top: OH-topaz, Stv: stishovite, Egg: Phase Egg.
Amount of run products (wt%) calculated from Rietveld refinements.

NH_4-hollandite, NH_4-Si-wadeite and NH_4-cymrite were synthesized using a rotating multi-anvil apparatus (Table 3.1). The advantage of rocking or rotating versus static systems for fluid-bearing charges is outlined in Schmidt and Ulmer (2004). To prevent separation of fluid and solid components, experiments were performed by 360°-rotation of the Walker-type module with a speed of 4°/s. The tungsten carbide anvils had a truncation edge length of 8 mm. Sample assemblies (Fig. 3.2) consisted of an MgO (+ 5% Cr_2O_3) octahedra with an edge length of 14 mm. The inner parts of the assembly were made up of a zirconia oxide sleeve, a stepped graphite heater, a Mo-disk and ring, and an axial thermocouple with wires of different W–Re alloys. Hexagonal boron nitride around the capsules was used as inner pressure medium because it was shown to behave relatively impermeable to hydrogen in piston cylinder experiments (Truckenbrodt et al. 1997), so that the furnace would not control the hydrogen fugacity of the sample within a reasonable time-span. The temperature was measured using a W5%Re–W26%Re (Type C) thermocouple. To protect the thermocouple wires, we used coils of the same material as the wires to eliminate any influences on the EMF of the thermocouples (Nishihara et al. 2006). The precision of the thermocouple is about ± 10 °C. The pressure calibration was performed by press-load experiments based on room temperature phase transitions in Bi and high-temperature phase transitions (quartz–coesite; $CaGeO_3$ garnet–perovskite; coesite–stishovite; forsterite–wadsleyite). The precision along the pressure range of this study is approximately ± 0.2 GPa.

exclude that the measured ammonium in the different analytical methods was due to outside contamination of the crystals, the run products were washed with 50 ml warm bi-distilled water and afterwards dried at 100 °C for several days.

3.3.2 Analytical methods

Powder X-ray diffraction (XRD). The run products were ground for several minutes in an agate mortar, diluted with Elmer's White glue and spread evenly on a "zero scattering" circular foil. Preferential orientation of the crystals was minimized by constantly stirring the

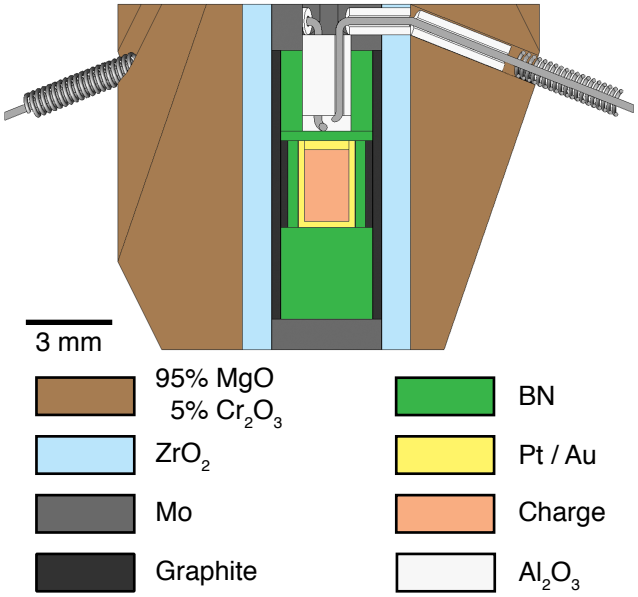

Figure 3.2: Schematic cross section of the 14/8 mm assembly used for multi-anvil experiments.

sample during the drying process. The sample was covered with an empty foil and mounted into a transmission sample holder. Powder XRD-patterns were recorded in transmission with a fully automated STOE STADI P diffractometer using CuKα_1-radiation at 40 kV and 40 mA, a take-off angle of 6°, a primary monochromator, and a 7° wide position-sensitive detector (PSD). The intensities were recorded between 5° and 125° 2θ with a detector step size of 0.1° and a resolution of 0.02°. Counting times were selected to result in a maximum intensity of around 3000 counts; this was due to about 20 s per detector step. The collected patterns were processed using the GSAS software package for Rietveld refinement (Larson and von Dreele 2004) for phase identification, phase proportions, and unit cell parameters. The refinement procedure for NH_4-bearing phases followed that of Pöter et al. (2007). Initial crystal structures were taken from the Inorganic Crystal Structure Database (ICSD, FIZ Karlsruhe, http://icsdweb.FIZ-karlsruhe.de). For input parameters, the structures of the respective potassium end-members were modified in that K was replaced by Na, because Na has the same number of electrons as NH_4. Due to the complexity of the NH_4-phengite sample (AW17-07, Table 3.1) with five polytypes ($1M, 2M_1, 2M_2, 3T$ and $2Or$), and coesite and kyanite as additional phases, the refinement was kept as simple as possible, i.e., common profile parameters were used for all mica polytypes by setting appropriate constraints. The statistical parameters χ^2 and Durbin-Watson (DW) of Rietveld refinements from all runs are within the ranges of $1 < \chi^2 < 1.26$ and $1.23 < \mathrm{DW} < 1.48$.

Infrared (IR) spectroscopy. About 1 mg of the run products was ground in an agate mortar and then mixed with 450 mg of dried KBr. The homogenized mixture was subsequently pressed into 13 mm diameter transparent pellets under vacuum and then dried for several days at 170 °C. Measurements were carried out in the spectral range from 4000 cm^{-1}

to 400 cm^{-1} with a resolution of 2 cm^{-1} using a Bruker IFS 66vFTIR spectrometer equipped with a globar as light source, a KBr beam-splitter and a DTGS-detector. The sample chamber of the interferometer was evacuated down to 200 Pa so that the influence of atmospheric H_2O and CO_2 was negligible. The measured spectra were averaged over 256 scans. The interferograms were phase-corrected after the procedure of Mertz (1965) and Griffiths and de Haseth (1986). Blackman-Harris 3-term mode was chosen as apodization function. The measured spectra were transformed into transmission spectra. After background correction the band center, FWHM, and integral intensity of each band were determined using the program PeakFit by Jandel Scientific.

Electron microprobe (EMP) analyses. Polished grain mounts of NH_4-hollandite from run AW14-07 and NH_4-phengite from run AW17-07 were measured using a JEOL JXA-8500F field emission electron probe microanalyzer in the wavelength-dispersive mode (WDS). As standards orthoclase (Al), wollastonite (Si) and periclase (Mg), only for the NH_4-phengites, were used. Attempts to obtain "good" nitrogen concentrations were not successful because crystal sizes are too small, count yields are low and NH_4-phases tend to decompose under the beam at long counting rates. Operating conditions were 10 kV, 5 nA and a beam diameter of about 50 nm. On-peak counting times were 10 s for Si and Al and 20 s for Mg. Background on both sides of the peak was measured for 5 and 10 s, respectively. Conditions were chosen carefully to reduce the damage of the mica under the electron beam. NH_4-hollandite crystals did not exceed 1 μm in width and 800 nm in thickness, NH_4-phengite crystals 2 μm in width and 250 nm in thickness. Calculation of the penetration depth of the focused electron beam resulted in about 1200 nm. Analyses of the NH_4-hollandite crystals were accepted, if the oxide sum, i.e., $SiO_2 + Al_2O_3$ was between 88.6 and 92.2 wt%; 89.9 wt% would represent an ideal NH_4-hollandite having 1 $(NH_4)_2O$ pfu. In case of the NH_4-phengites analyses were accepted, if $SiO_2 + MgO + Al_2O_3$ was between 84 and 88.3 wt%, the latter representing an ideal NH_4-phengite having additionally 1 $(NH_4)_2O$ and 1 H_2O pfu. The composition of NH_4-hollandite was calculated on the basis of 8 oxygens and assuming full occupation of the interlayer site. The NH_4-phengite composition was calculated on the basis of 11 oxygens assuming ideal dioctahedral micas with 2/3 of the octahedral and all of the tetrahedral sites occupied, full occupation of the interlayer site by one NH_4, and two OH groups pfu. Because nitrogen was not measured, possible deficiencies in interlayer NH_4 and concomitant occurrence of some pyrophyllite or talc component in NH_4-phengite (see Pöter et al. 2007; for synthetic NH_4-muscovite) are disregarded.

Scanning electron microscopy (SEM). Reaction products were characterized using a high resolution Hitachi S-4000 instrument at the TU Berlin. Individual phases (Table 3.1) were identified by EDS-analysis of the respective elements.

3.4 Results

Starting materials, experimental conditions and relative amounts of run products are summarized in Table 3.1. All experiments produced new NH_4-phases, though always with additional phases in various amounts. Run AW14-07 (12.3 GPa, 700 °C) produced NH_4-hollandite along with NH_4-Si-wadeite, stishovite, OH-topaz, kyanite, and traces of phase Egg. Run AW28-07 (10.0 GPa, 700 °C) yielded NH_4-Si-wadeite together with OH-topaz

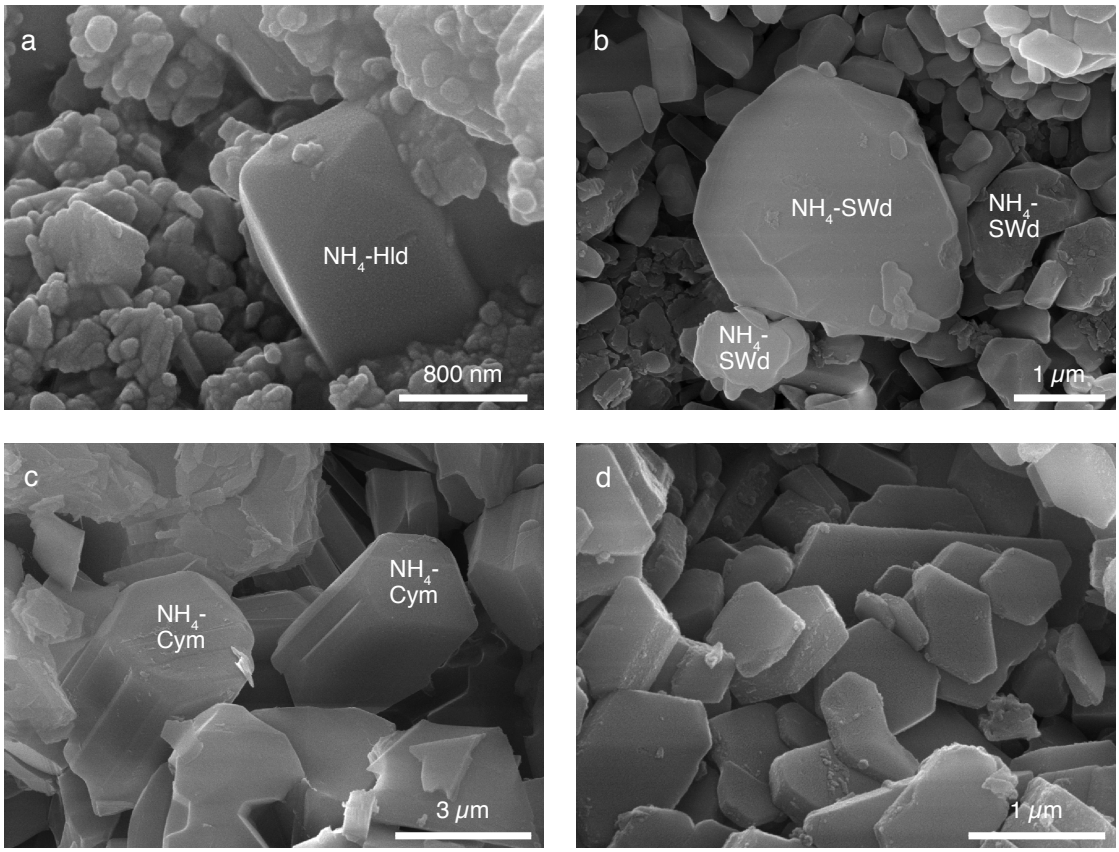

Figure 3.3: Scanning electron micrographs of the run products. **(a)** NH_4-hollandite, run AW14-07. **(b)** NH_4-Si-wadeite, OH-topaz, and stishovite, run AW28-07. **(c)** NH_4-cymrite, run AW22-07. **(d)** NH_4-phengite, run AW17-07.

and stishovite. Run AW21-07 (7.8 GPa, 800 °C) gave NH_4-cymrite plus coesite and kyanite. Run AW22-07, at initially dry starting conditions and identical P and T of 7.8 GPa, 800 °C also produced NH_4-cymrite plus coesite and kyanite. In AW17-07 (4 GPa, 700°C) various polytypes of NH_4-phengite were produced, along with traces of coesite and kyanite. SEM-micrographs of run products with the relevant phases NH_4-hollandite, NH_4-Si-wadeite, NH_4-cymrite, and NH_4-phengite are shown in Figure 3.3a-d. Grain sizes of all new NH_4-phases rarely exceed 3 μm. NH_4-hollandite, NH_4-cymrite and NH_4-phengite form idiomorphic crystals with typical tetragonal (NH_4-Hld; Fig. 3.3a), hexagonal (NH_4-Cym; Fig. 3.3c) and pseudohexagonal (NH_4-Phg; Fig. 3.3d) crystal shapes. Glass or any phase resembling quenched melt was not observed in any of the experimental products.

Unit cell dimensions of NH_4-hollandite, NH_4-Si-wadeite and NH_4-cymrite are given in Table 3.2 along with that of their potassium-bearing analogues. The substitution of NH_4 for K does not induce changes in space group symmetry of the three new NH_4-phases when compared to their respective K-analogues. Lattice parameters, however, change significantly due to the incorporation of the larger NH_4^+ instead of the K^+ cation. The ionic radius of

Table 3.2. Lattice parameters of NH_4-bearing high-pressure phases calculated from Rietveld refinements. For comparison, respective K-phases are also given.

Phase	*a* (Å)	*c* (Å)	*V* (Å^3)	Space group
NH_4-hollandite	9.4234(9)	2.7244(3)	241.93(5)	*I4/m*
K-hollandite*	9.315(4)	2.723(4)	236.3(4)	
NH_4-Si-wadeite	6.726(1)	9.502(3)	372.3(1)	*P6$_3$/m*
K-Si-wadeite†	6.6124(9)	9.5102(8)	360.11(7)	
NH_4-cymrite	5.359(1)	7.835(9)	194.93(2)	*P6/mmm*
K-cymrite‡	5.3348(1)	7.7057(1)	189.924(8)	

*Zhang et al. (1993)
† Swanson and Prewitt (1983)
‡ Fasshauer et al. (1997)

K^+ in VI, VIII, and XII-fold coordination is 1.38, 1.51, and 1.64 Å, respectively (Shannon 1976), whereas that of NH_4^+ is about 1.59, 1.68, and 1.80 Å. The latter values are estimated from composition-volume relationships of alkali-bearing silicates (M. Gottschalk, personal communication).

For NH_4-hollandite, the average of 17 EMP analyses results in $NH_4Al_{1\pm0.03}Si_{3\pm0.03}O_8$, assuming 1 NH_4^+ pfu. The average of 21 EMP analyses for NH_4-phengites results in $NH_4(Mg_{0.45\pm0.03}Al_{1.53\pm0.03})(Al_{0.49\pm0.03}Si_{3.51\pm0.03})O_{10}(OH)_2$, also assuming 1 NH_4^+ pfu. The NH_4-celadonite component of the NH_4-phengites is slightly lower than that given by the NMASH bulk composition. The five polytypes $1M, 2M_1, 2M_2, 3T$ and $2Or$ are present, with $2M_1$ (75%) and $3T$ (14%) as the predominant phases (Table 3.1). Unit cell parameters of the polytypes are presented in Table 3.3. They were calculated using the multi-polytype refinement model for synthetic K-phengite polytype mixtures proposed by Schmidt et al. (2001). Polytypes $2Or, 1M$ and $2M_2$ occur in minor or minute amounts and their cell parameters are somewhat less reliable. For comparison, unit cell parameters of synthetic $2M_1$ and $1M$ K-phengites with K-celadonite components similar to our NH_4-celadonite components

Table 3.3. Lattice parameters of NH_4-phengite polytypes produced in run AW17-07. Data calculated from Rietveld refinements.

Phase	*a* (Å)	*b* (Å)	*c* (Å)	β (°)	*V* (Å^3)	Space group
NH_4-Phg *2M$_1$*	5.2204(8)	9.049(2)	20.44(1)	95.71(3)	960.9(5)	*C2/c*
NH_4-Phg *3T*	5.220(2)	30.64(2)			723.2(6)	*P3$_1$12*
NH_4-Phg *2Or*	5.220(2)	8.992(7)		20.65(4)	969(2)	*Pnmn*
NH_4-Phg *1M*	5.315(4)	9.067(4)	10.46(1)	101.79(8)	493.1(7)	*C2*
NH_4-Phg *2M$_2$*	8.93(1)	5.198(5)	20.77(3)	99.3(1)	952(2)	*C2/c*
K-Phg *2M$_1$*	5.2118(6)	9.041(2)	19.972(1)	95.44(6)	936.3(1)	*C2/c*
K-Phg *1M*	5.201(1)	9.026(2)	10.131(4)	101.12(2)	468.5(4)*	*C2/c*

Notes: Data for K-phengite are from Massonne and Schreyer (1986); their experiments V90 (*2M$_1$*) and V270 (*1M*).
*calculated from lattice parameters.

Table 3.4. Band assignments for vibration modes (ν) with respect to the band centers in cm^{-1} along with relative intensities.

ν	$(NH_4)^+$*	NH_4-Hld	NH_4-SWd	NH_4-Cym	NH_4-Phg	Budd	Tob†
ν_4	1397	1402 sh (m)	1397 sh (m)	1404 sh (w)	1407 sh (m)	1402 sh (w)	1430 (s)
		1436 (s)	1422 (s)	1423 (s)	1433 (s)	1423 sh (m)	1475 sh (m)
		1459 sh (m)	1438 sh (m)	1447 sh (m)		1445 (m)	
ν_2	1685	1669 (w)	1671 (w)	not obs.	1660 (w)	1690 (w)	not obs.
$2\nu_4$		2878 (m)	2842 (m)	2852 (w)	2825 (w)	2844 (w)	2825 (m)
$\nu_2+\nu_4$		3043 (m)	2967 sh (m)	3091 sh (m)	3042 (m)	3065 (m)	3035 (m)
		3025 (m)					
$2\nu_2$		3140 (s)	3140 (s)	3179 sh (m)	3170 (w)	3187 sh (w)	3175 (m)
ν_3	3134	3223 (m)	3320 (m)	3233 sh (m)	3246 sh (m)	3288 (s)	3300 (s)
		3281 sh (w)		3294 (s)	3311 (s)		3455 sh (w)
		3333 sh (w)					

* Values for the free NH_4^+ molecule from Herzberg (1966).
† Values from Harlov et al. (2001b).
Abbreviations: as in Table 3.1; Budd: buddingtonite, Tob: tobelite, sh: shoulder, w: weak, m: medium, s: strong. For further explanation see text.

are also given (Table 3.3; data for K-phengites from Massonne and Schreyer 1986).

IR spectra of run products AW14-07, AW28-07, AW22-07, and AW17-08 are presented in Figure 3.4, along with the spectra of synthetic buddingtonite and tobelite (sample 13-99 from Pöter et al. (2007)). The free ammonium ion NH_4^+ has T_d symmetry resulting in four normal vibrational modes (Herzberg 1966): symmetric (ν_1) and antisymmetric (ν_3) stretching vibrations, and symmetric (ν_2) and antisymmetric (ν_4) bending vibrations (Kearley and Oxton 1983). All fundamentals are Raman-active, but only the triply degenerated states ν_3 and ν_4 are IR-active. However, in complex structures the NH_4 symmetry is reduced by the crystal field, so that the ν_1 and ν_2 bands appear in IR spectra, and the degeneracy of the ν_2, ν_3 and ν_4 bands may be annihilated to some extent. Positions of the NH_4 vibration modes in Figure 3.4 follow the assignments for buddingtonite (Harlov et al. 2001a). Table 3.4 summarizes band positions and relative intensities along with the fundamental frequencies of the free ammonium molecule (Nakamoto, 1986, after Landolt-Börnstein, 1951), but several studies (Likhacheva et al. 2002; Mookherjee et al. 2002a, b; Harlov et al. 2001b, c) show that in varying minerals the frequencies differ due to the crystal field and are mostly higher than the reported data for the free ion.

Ammonium incorporation into all new high-pressure phases is clearly demonstrated by the appearance of the NH_4 bending mode(s) ν_4, occurring in the range from 1397 to 1459 cm^{-1} (Fig. 3.4). Stretching mode(s) ν_3 appear at 3223 to 3333 cm^{-1} for NH_4-cymrite and NH_4-phengite (see also Harlov et al. 2001b, for NH_4-muscovite). There are no significant ν_3 modes for NH_4-hollandite and NH_4-Si-wadeite at these wavenumbers, instead, a strong band is present at about 3130 cm^{-1} for these two phases. One may speculate that this represents ν_3 due to a shift towards lower wavenumbers in the higher coordinated structures. A comparison between NH_4-phengite and tobelite show a wide accordance among the spectra, the small observable differences are caused by the additional Mg in the octahedral site of the phengite.

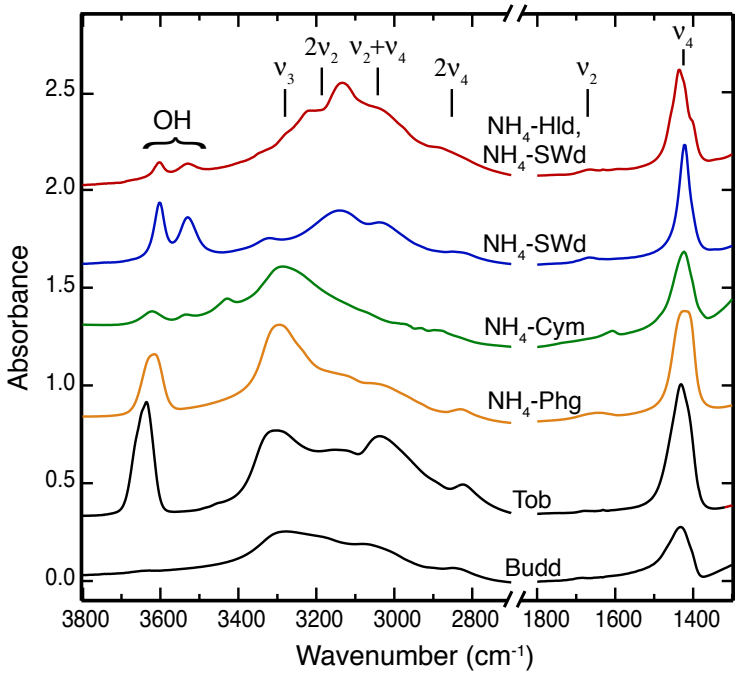

Figure 3.4: Mid-Infrared spectra of the run products of AW14-07 [NH_4-hollandite (31 wt%) plus NH_4-Si-wadeite (17 wt%)], AW28-07 (NH_4-Si-wadeite), AW22-07 (NH_4-cymrite), AW17-07 (NH_4-phengite), tobelite [see Pöter et al. (2007), their sample 13-99] and buddingtonite in the range from 1300 to 1800 and from 2700 to 3800 cm^{-1}. Spectra are shifted vertically. Relative proportions of NH_4-Hld and NH_4-SWd are calculated from Rietveld refinements. The normal modes on the basis of T_d symmetry for the NH_4-tetrahedron are marked as described by Harlov et al. (2001a) for buddingtonite. Additional OH-vibrations in the upper two spectra stem from OH-topaz (Table 3.1).

Due to the distortion of the crystal field, ν_2 appears as an additional weak band in the range from 1660 to 1690 cm^{-1}; further weak bands and shoulders arise from overtone and combination modes (Fig. 3.4, Table 3.4). A detailed description of the effective symmetry of the NH_4 molecule is not possible from IR spectra alone because ν_3, overtones $2\nu_2$ and $2\nu_4$, and combination modes $\nu_2 + \nu_4$ interfere with each other at similar wavenumbers (Harlov et al. 2001b). Therefore, the band assignments (Table 3.4), which are based on identified bands for buddingtonite and other NH_4-bearing minerals (Harlov 2001a, b, c; Pöter et al. 2007) represent only one of several possibilities.

Bands at 3531 and 3603 cm^{-1} as occurring in the spectra of the NH_4-hollandite and NH_4-Si-wadeite-bearing samples represent the two OH-stretching bands of OH-topaz (Wunder et al. 1993). NH_4-cymrite contains molecular water, consequently, in the NH_4-cymrite-bearing sample a H_2O bending mode at 1606 cm^{-1} and the OH-stretching modes at 3533 and 3621 cm^{-1} are present, the positions are the same as observed by Fasshauer et al. (1997) for K-cymrite. According to that study the shoulder, which can be observed at 3433 cm^{-1}, is also due to H_2O. The spectrum of NH_4-phengite shows the typical OH-stretching vibration

of micas from 3604 to 3629 cm^{-1} (e.g., Harlov 2001b; Pöter et al. 2007).

3.5 Discussion

3.5.1 Crystal structure comparison between NH_4- and K-bearing phases

NH_4-hollandite [$NH_4AlSi_3O_8$]. The crystal structure of hollandite (Fig. 3.5a) is constructed of edge-sharing octahedra that form a four-sided eight-membered channel. The octahedra are randomly occupied to 3/4 with Si and 1/4 with Al. The channel is capable of incorporating low-valence large-radius cations in twelve-fold coordination, such as Na^+ (Liu et al. 1978), K^+ (Ringwood et al. 1967), and NH_4^+ (this study). The space group is $I4/m$. Comparison with K-hollandite reveals that the c lattice parameter remains largely unchanged whereas the a lattice parameter increases from 9.315 Å (K-hollandite; Zhang et al. 1993) to 9.423 Å (NH_4-hollandite; Table 3.2). The larger NH_4^+ ion significantly expands the diameter of the octahedra channels, but not the channel length. The cell volume increases from 236.3 $Å^3$ (K-hollandite) to 241.93 $Å^3$ (NH_4-hollandite). The same behavior can be observed in case of the smaller Na^+-ion. The a lattice parameter of Na-hollandite (9.30 Å) shows a significant reduction compared to K-hollandite, while the channel length remains nearly unchanged (c = 2.73 Å; Liu et al. 1978).

NH_4-Si-wadeite [$(NH_4)_2Si_4O_9$]. The crystal structure of NH_4-Si-wadeite and its K-analogue Si-wadeite [$K_2Si_4O_9$] (Kinomura et al. 1975; Yagi et al. 1994) is a framework structure consisting of parallel Si_3O_9-layers in an ABAB... stacking sequence along the c axis (Fig. 3.5b). The layers are linked by Si-occupied octahedra. In Si-wadeite 1/4 of the total Si is octahedrally coordinated and 3/4 is tetrahedrally coordinated. K^+ and NH_4^+ are nine-fold coordinated and sit in large cages, which occur between the A and B layers of the Si_3O_9 rings. The space group is $P6_3/m$. Comparison with K-Si-wadeite shows nearly identical c lattice parameters (Table 3.2), whereas the a lattice parameter increases from 6.6124 Å (K-Si-wadeite; Swanson and Prewitt 1983) to 6.726 Å (NH_4-Si-wadeite). Incorporation of NH_4 instead of K expands the diameter of the Si_3O_9-rings and hence the cages. Neither the stacking sequence of the layers nor their distance is changed. The cell volume increases from 360.1 (K-Si-wadeite) to 372.1 $Å^3$ (NH_4-Si-wadeite).

NH_4-cymrite [$NH_4AlSi_3O_8 \cdot H_2O$]. NH_4-cymrite and K-cymrite display a sheet-like crystal structure (Fig. 3.5c). Si and Al are randomly distributed on symmetrically equivalent tetrahedrally coordinated sites. The tetrahedra form hexagonal rings, which are further connected to double-layers via common opposite vertices. NH_4 and K in twelve-fold coordination are situated in the middle of the rings between two of these double-layers. Molecular water is located within the double six-membered tetrahedral rings, whereas its orientation along the c axis is yet unknown. The space group is $P6/mmm$. Compared to K-cymrite (c = 7.7057 Å; Fasshauer et al. 1997), NH_4-cymrite (c = 7.835 Å) shows the major increase in the c lattice parameter, whereas the a lattice parameter increases only by 0.5% (Table 3.2). This is typical for sheet-like structures, where substitution of larger monovalent interlayer cations for smaller ones drastically enlarges the distance between the sheets, whereas the six-membered tetrahedral rings are only slightly expanded. It has been argued that there is only one crystallographic site for molecular water in K-cymrite, due to the occurrence of only two peaks in the OH-stretching region (Thompson et al. 1998). The IR spectrum of

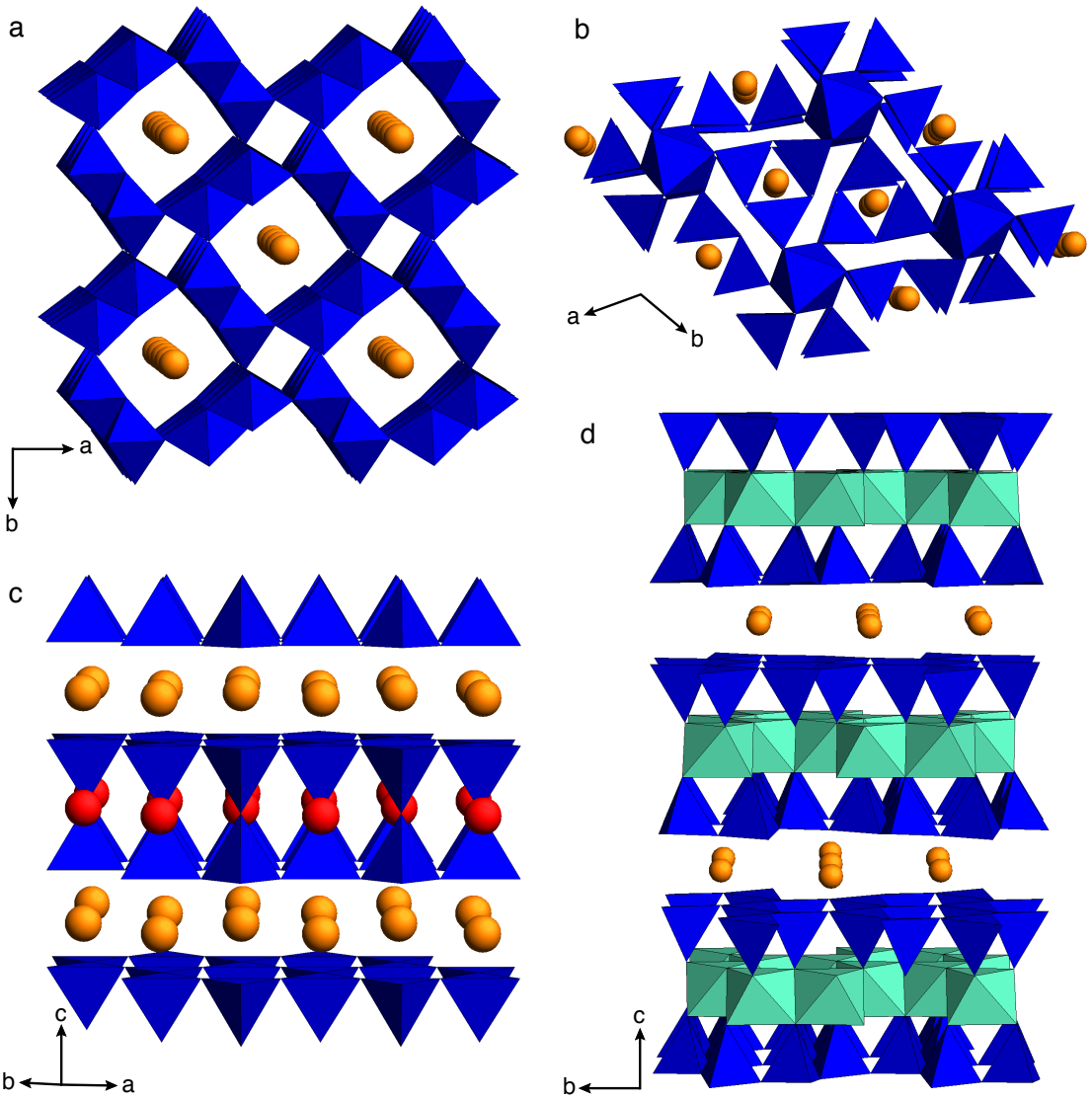

Figure 3.5: Projection of crystal structures of **(a)** NH_4-hollandite and **(b)** NH_4-Si-wadeite viewed down the c axis, **(c)** NH_4-cymrite; and **(d)** NH_4-phengite ($2M_1$ polytype) viewed along the a axis. The NH_4^+ ion is illustrated as sphere in orange, a possible ordering/disordering of the NH_4^+ cations in the crystal structures is neglected, as there was no hint from the XRD refinements. Si-containing tetrahedra and octahedra are shown in blue. The red balls in the NH_4-cymrite structure represent the H_2O-molecules. The light green octahedra in the phengite structure are occupied by Al and Mg.

NH_4-cymrite shows the same two peaks at the respective wavenumbers, so that no variation in the order of the water molecules is indicated.

NH_4-phengite $[\mathbf{NH_4(Mg_{0.5}Al_{1.5})(Al_{0.5}Si_{3.5})O_{10}(OH)_2}]$. Comparison of the lattice parameters of $2M_1$ NH_4-phengite (Fig. 3.5d) with that of $2M_1$ K-phengite having nearly

identical celadonite component (Massonne and Schreyer 1986) reveals that the c lattice parameter and angle β are significantly enlarged (19.972 Å vs 20.44 Å; 95.44° vs 95.71°) whereas the a and b lattice parameters show only a very slight increase (Table 3.2). In case of the $1M$ polytypes the c lattice parameter is likewise increased but the angle β contracts by about 0.1%. There is a much larger difference in the a lattice parameters for the $1M$ polytypes compared to that for the $2M_1$ polytypes. This holds also for b, though to a minor extent. Similar variations in cell parameters between $1M$ and $2M_1$ polytypes of muscovite and tobelite, i.e., NH_4-muscovite, are documented in Pöter et al. (2007). The tetrahedral distortion due to tetrahedral rotation in dioctahedral micas is described by the rotation angle α, where $\cos\alpha = b/(9.051 + 0.254N)$ (Radoslovich and Norrish 1962; Bailey 1984). N is the number of tetrahedral Al atoms pfu and b is the lattice parameter. The tetrahedral rotation angle of $2M_1$ K-phengite with the celadonite component given above is calculated to 9.9°, that of $2M_1$ NH_4-phengite to 9.5° (Massonne and Schreyer 1986; Table 3.4). The larger NH_4^+ ion stretches not only the distance between the sheets but also reduces the extent of tetrahedral rotation in the NH_4- relative to the K-phengite. Differences may also exist in the development of the respective polytypes. Schmidt et al. (2001) synthesized K-phengites in the KMASH system at similar conditions and report that there is no clear dependence of the polytype distributions on their celadonite component, however, in the K-bearing system the $1M$ is much more abundant than the $3T$-polytype. This is quite the contrary to our NH_4-pengites ($3T$: 13.6 wt%; $1M$: 1 wt%) indicating that the larger NH_4^+ ion might favor formation of the $3T$-polytype.

3.5.2 Stabilities compared to K-analogues

The stability of NH_4-phases depends on the redox conditions. Conditions must be reducing to allow the formation of NH_3/NH_4^+ in the mineral-fluid system and to prevent oxidation to N_2. There is little information on the speciation of H–N–O fluids at very high pressures. Calculations using the perturbation theory-based equation of state of Churakov and Gottschalk (2003b) reveal that H–N–O fluids buffered by QFM in the relevant P–T range will consist almost exclusively of H_2O and N_2 (see also Simakov 1998; 2006). An abrupt transition is indicated at f_{O_2} between -2 and -3 log units below QFM so that towards more reducing conditions NH_3 and H_2O become the main species. Data on the dissociation constant $log(K)$ of $(NH_3)H_2O \leftrightarrow NH_4^+ + OH^-$ only exist for very dilute solutions up to 700 °C and 400 MPa (Quist and Marshall 1968). $Log(K)$ ranges from about 10–9 at fluid densities of 0.5 g/cm^3 to about 10–3 at 1.15 g/cm^3. Fluid densities in our experiments are much higher, up to 1.5–1.6 g/cm^3 (Churakov and Gottschalk 2003a, 2003b), and one may expect much stronger dissociation, the extent of which remains unknown. In any case, redox conditions in our experiments were sufficiently reducing to enable the formation of NH_4-silicates in presence of NH_3-bearing fluid, albeit some oxidation and formation of N_2 due to hydrogen loss may have occurred during the course of the experiments.

In the NASH system, the stabilities of high-pressure NH_4-silicates in the presence of fluid in P–T space broadly correspond to their K-analogues. K-cymrite is stable from 2.5 GPa, 400 °C to about 9 GPa, 1200 °C (Fasshauer et al. 1997; Thompson et al. 1998; Harlow and Davies 2004). The two experiments at 7.8 GPa, 800 °C on buddingtonite bulk composition are well located within the stability field of K-cymrite and produced NH_4-

cymrite plus some coesite and kyanite as additional phases. Run AW22-07 was performed on nominally dry buddingtonite, without adding fluid. Even the breakdown of nominally dry buddingtonite along with a little amount of absorbed surface water, which could not be avoided in sample preparation, provided sufficient NH_3- and H_2O-bearing fluid to stabilize NH_4-cymrite along with coesite and kyanite. At the given conditions and in presence of pure H_2O-fluid ($a_{H_2O} = 1$) OH-topaz is stable (Wunder et al. 1993); we, however, observe kyanite + H_2O. A possible interpretation is that due to the significant amounts of nitrogen-bearing species in the fluid the water activity is reduced, thus expanding the stability field of kyanite relative to OH-topaz. Towards higher pressure of 10 GPa at 700 °C, NH_4-Si-wadeite is formed, along with stishovite and OH-topaz, the latter stably replacing kyanite + H_2O (Wunder et al. 1993). This is similar to the K-bearing system, where K-Si-wadeite + kyanite + silica replaces K-cymrite as pressure increases (Davies and Harlow 2002). K-Si-wadeite + kyanite + stishovite produce K-hollandite at pressures higher than 8 to 9 GPa by a water-absent univariant reaction (Yong et al. 2008; Fig. 3.1). In the NH_4-bearing system, NH_4-Si-wadeite (+ OH-topaz + stishovite) persists at least up to 10 GPa. NH_4-hollandite appears at 12.5 GPa, 700 °C, together with NH_4-Si-wadeite, OH-topaz, kyanite, and stishovite. Taking the NH_4-bearing system as an analogue to the K-bearing system, it appears that both the low-pressure assemblage (NH_4-SWd + OH-Top/Ky + Stv) and the high-pressure phase (NH_4-Hld) were concurrently formed. This may indicate that our experimental conditions happened to meet the NH_4-hollandite-forming reaction curve and that the NH_4-hollandite-in reaction occurs at pressures a few GPa higher than that for K-hollandite. On the other hand, the reaction is not univariant because of shifts in the fluid composition due to hydrogen loss, and it may well be that the produced assemblage is transitional in response to changing activities of fluid phase components. The latter is somewhat supported by the presence of both kyanite and OH-topaz, probably resulting from changing water activity during the course of the experiment. In any case, stability relations of the high-pressure NH_4-silicates closely resemble that of their K-analogues in that the same sequence of K- and NH_4-cymrite, K- and NH_4-Si-wadeite, and K- and NH_4-hollandite occurs from lower to higher pressures along approximately the same pressure range.

In fluid-saturated metabasaltic and metapelitic model systems it has been experimentally shown that K-phengite is stable up to about 9.5 GPa, 750 to 1000 °C. At higher pressures, it breaks down to K-hollandite + clinopyroxene-bearing assemblages (Domanik and Holloway 1996; Schmidt 1996; Schmidt and Poli 1998; Poli and Schmidt 2002). Clinopyroxene formed at these conditions incorporates about 1 wt% of K_2O (Schmidt and Poli 1998; Bindi et al. 2006). We synthesized NH_4-phengite at 4 GPa, 700 °C. There is again no information on its upper pressure stability, however, given the strong similarities between the KASH and NASH systems one may reasonably assume that NH_4-phengite in natural systems would react to NH_4-hollandite + clinopyroxene-bearing assemblages at similar pressure. If so, incorporation of significant amounts of NH_4 into high-pressure clinopyroxene is possible. As K-hollandite may persist up to 95 GPa, 2300 °C (cf. above) it is conceivable that NH_4-hollandite is also stable at conditions through the transition zone to the lower mantle.

3.5.3 Implications for nitrogen and hydrogen transport into Earth's mantle

At conditions of 500 to 600 °C, 0.2 to 0.4 GPa the binaries K-muscovite–NH_4-muscovite (tobelite), K-feldspar–NH_4-feldspar (buddingtonite), and K-phlogopite–NH_4-phlogopite form complete solid solution series (Bos et al. 1988; Pöter et al. 2004, 2007). Given the similarities in structure and stability relations, this probably holds also for the high-pressure end-members. In any case, high-pressure K-phases are expected to be able to incorporate large amounts of NH_4 into their structures. If so, NH_4 can be continuously redistributed into solids when high-pressure K-phases are successively generated at conditions of subducting slabs. This provides an important means for nitrogen transport into the deep mantle (see also Busigny et al. 2003; Thomassot et al. 2007).

Incorporation of ammonium into K-hollandite and possibly high-pressure clinopyroxene and transport into the deeper mantle may have another important implication. There is a wealth of experimental work addressing the actual concentrations and the storage capacity of H_2O in nominally anhydrous minerals in the upper mantle down to the transition zone (for summaries see Hirschmann et al. 2005; Keppler and Bolfan-Casanova 2006). There is overall agreement that the H_2O storage capacity in nominally anhydrous mantle assemblages just above the transition zone amounts to about 0.4 wt% (Hirschmann et al. 2005) and to at least 5 times higher when wadsleyite becomes stable. Bromiley and Keppler (2004) argued that omphacitic clinopyroxene is the main OH-bearing phase in subducted eclogites after breakdown of hydrous minerals with maximum concentrations of a few hundred wt-ppm of H_2O, dependent on clinopyroxene composition and pressure. Natural omphacites usually have several hundred with maximum concentrations of about 1000 wt-ppm H_2O (Skogby 2006). It would thus appear that omphacites and their breakdown products were unable to feed the transition zone with large amounts of water. If, on the other hand, most of the available NH_4 in eclogite-facies rocks can be stored in K-rich phases such as clinopyroxene and hollandite to greater depth, this would provide a formidable mechanism of hydrogen transport into the transition zone and beyond. If so, the fate of any possible NH_4-silicate component at depths of the transition zone would be subject to the redox conditions, of which no sound information is currently available. Hypothetical oxidation reactions of the type NH_4-component in solid + O_2 → solid(s) + N_2 + H_2O would produce water and molecular nitrogen, forming two H_2O molecules from one NH_4; under reducing conditions NH_4 component in solids would form ammonia and water by reaction to solid(s) + NH_3 + H_2O; and one may even speculate that under very reducing conditions nitrides or oxonitride component in oxides and hydrogen could possibly be generated. The latter is certainly speculative, however, if one accepts that highly reduced phases such as moissanite and Fe-silicides included in deep-seated diamonds (e.g., Moore et al. 1986; Otter and Gurney 1989; Leung et al. 1990, 1996) or in kimberlitic rocks (Mathez et al. 1995; Di Pierro et al. 2003) represent redox conditions of certain, albeit limited regions of the mantle, oxygen fugacities of 5 to 6 log units below the iron-wuestite buffer were indicated (e.g., Mathez et al. 1995). At about that conditions nitrides or oxonitrides may also become stable, and it may well be that they provide another solid sink for nitrogen in the deep Earth, aside from nitrogen in diamonds.

Sediments and metasediments may contain several thousands of wt-ppm of ammonium present in clay minerals, micas and feldspars, which is continuously redistributed into newly

formed high-pressure K-bearing phases along rocks' P–T path during subduction. This provides the means for nitrogen and hydrogen transport down to the transition zone of the Earth's mantle and possibly to even greater depth. Ammonium as a component is potentially very important for long-time, large-scale recycling of hydrogen and nitrogen between the Earth's surface and the deep mantle.

Acknowlegdements

We thank A. Hahn and R. Schulz for technical assistance, U. Gernert (ZELMI, Technical University of Berlin) for providing SEM facilities, D. Rhede and O. Appelt for help with EMP work, and M. Gottschalk for fruitful discussions. The reviews by M. Mookherjee and J. Konzett, and the editorial comments by E. Libowitzky helped to improve the manuscript and were highly appreciated. This work was supported by the German Science Foundation [He 2015/(8-1)] within the framework of the Priority Program 1236 "Structures and properties of crystals at extreme pressures and temperatures" which is gratefully acknowledged.

3.6 References

Akaogi, M., Yusa, H., Shiraishi, K., and Suzuki, T. (1995) Thermodynamic properties of α-quartz, coesite, and stishovite and equilibrium phase relations at high pressures and high temperatures. Journal of Geophysical Research, 100, 22337-22347.

Bailey, S.W. (1984) Crystal chemistry of the true micas. In S.W. Bailey, Eds., Micas, 13, p. 13-60. Reviews in Mineralogy, Mineralogical Society of America, Chantilly, Virginia.

Bebout, G.E. and Fogel, M.L. (1992) Nitrogen-isotope compositions of metasedimentary rocks in the Catalina schists, California: Implications for metamorphic devolatilization history. Geochimica et Cosmochimica Acta, 56, 2839-2849.

Bebout, G.E., Cooper, D.C., Bradley, A.D., and Sadofsky, S.J. (1999) Nitrogen-isotope record of fluid-rock interactions in the Skiddaw aureole and granite, English Lake District. American Mineralogist, 84, 1495-1505.

Bindi, L., Downs, R.T., Harlow, G.E., Safonov, O.G., Litvin, Y.A., Perchuk, L.L., Uchida, H., and Menchetti, S. (2006) Compressibility of synthetic potassium-rich clinopyroxene: In-situ high-pressure single-crystal X-ray study. American Mineralogist, 91, 802-808.

Bos, A., Duit, W., Van der Eerden, A.M.J., and Jansen J.B.H. (1988) Nitrogen storage in biotite: an experimental study of ammonium and potassium partitioning between $1M$-phlogopite and vapor at 2 kb. Geochimica et Cosmochimica Acta, 52, 1275-1283.

Bromiley, G.D. and Keppler, H. (2004) An experimental investigation of hydroxyl solubility in jadeite and Na-rich clinopyroxenes. Contributions to Mineralogy and Petrology, 147, 189-200.

Busigny, V., Cartigny, P., Philippot, P. Ader, M., and Javoy, M. (2003) Massive recycling of nitrogen and other fluid-mobile elements (K, Rb, Cs, H) in a cold slab environment: evidence from HP to UHP oceanic metasediments of the Schistes Lustrés nappe (western Alps, Europe). Earth and Planetary Science Letters, 215, 27-42.

Cartigny, P. and Ader, M. (2003) A comment on "The nitrogen record of crust-mantle interaction and mantle convection from Archean to Present" by B. Marty and N. Dauphas. Earth and Planetary Science Letters, 206, 397-410.

Churakov, S.V. and Gottschalk, M. (2003a) Perturbation theory based equation of state for polar molecular fluids: I. Pure fluids. Geochimica et Cosmochimica Acta, 67, 2397-2414.

Churakov, S.V. and Gottschalk, M. (2003b) Perturbation theory based equation of state for polar molecular fluids: II. Fluid mixtures. Geochimica et Cosmochimica Acta, 67, 2415-2425.

Davies , R.M. and Harlow, G.E. (2002) The high pressure stability of K-cymrite and phases in the system $Or - H_2O$. American Geophysical Union, Fall Meeting 2002, Abstract No.V72B-1308.

Di Pierro, S., Gnos, E., Grobety, B.H., Armbruster, T., Bernasconi, S.M., and Ulmer, P. (2003) Rock-forming moissanite (natural α-silicon carbide). American Mineralogist, 88, 1817-1821.

Domanik, K.J. and Holloway, J.R. (1996) The stability and composition of phengitic muscovite and associated phases from 5.5 to 11 GPa: implications for deeply subducted sediments. Geochimica et Cosmochimica Acta, 60, 4133-4154.

Fasshauer, D.W., Chatterjee, N.D., and Marler, B. (1997) Synthesis, structure, thermodynamic properties, and stability relations of K-cymrite, $K[AlSi_3O_8] \cdot H_2O$. Physics and Chemistry of Minerals, 24, 455-462.

Fischer, T.P., Hilton, D.R., Zimmer, M.M., Shaw, A.M., Sharp, Z.D., and Walker, J.A. (2002) Subduction and recycling of nitrogen along the Central American Margin. Science, 297, 1154-1157.

Fischer, T.P., Takahara, N., Sano, Y., Sumino, H., and Hilton, D.R. (2005) Nitrogen isotopes in the mantle: Insights from mineral separates. Geophysical Research Letters, 32, L11305.

Griffiths, P.R. and de Haseth, J.A. (1986) Fourier transform infrared spectroscopy. John Wiley and Sons, New York.

Harlov, D.E., Andrut, M., and Pöter, B. (2001a) Characterisation of buddingtonite $(NH_4)[AlSi_3O_8]$ and ND_4-buddingtonite $(ND_4)[AlSi_3O_8]$ using IR spectroscopy and Rietveld refinement of XRD spectra. Physics and Chemistry of Minerals, 28, 188-198.

Harlov D.E., Andrut, M., and Pöter, B. (2001b) Characterisation of tobelite $(NH_4)Al_2[AlSi_3O_{10}](OH)_2$ and ND_4-tobelite $(ND_4)Al_2[AlSi_3O_{10}](OD)_2$ using IR spectroscopy and Rietveld refinement of XRD spectra. Physics and Chemistry of Minerals, 28, 268-276.

Harlov, D.E., Andrut, M., and Melzer S (2001c) Characterisation of NH_4-phlogopite $(NH_4)[Mg_3AlSi_3O_{10}](OH)_2$ and ND_4-phlogopite $(ND_4)[Mg_3AlSi_3O_{10}](OD)_2$ using IR spectroscopy and Rietveld refinement of XRD spectra. Physics and Chemistry of Minerals, 28, 77-86.

Harlow, G.E. and Davies R.M. (2004) Status report on stability of K-rich phases at mantle conditions. Lithos, 77, 647-653.

Herzberg, G. (1966) Molecular Spectra and Molecular Structure Vol.2: Infrared and Raman Spectra of Polyatomic Molecules. Van Nostrand, Princeton.

Hirschmann, M.M., Aubaud, C., and Withers, A. (2005) Storage capacity of H_2O in nominally anhydrous minerals in the upper mantle. Earth and Planetary Science Letters, 236, 167-181.

Javoy, M., Pineau, F., and Delorme, H. (1986) Carbon and nitrogen isotopes in the mantle. Chemical Geology, 57, 41-62.

Kearley, G.J. and Oxton, L.A. (1983) Recent advances in the vibrational spectroscopy of ammonium ion in crystal. In R.J.H. Clark et R.E. Hesters, Eds., Advances in Infrared and Raman Spectroscopy, 10, Chap. 2, John Wiley and Sons, New York.

Keppler, H. and Bolfan-Casanova, N. (2006) Thermodynamics of water solubility and partitioning. In H. Keppler and J.R. Smyth, Eds., Water in nominally anhydrous minerals, 62, p. 193-230. Reviews in Mineralogy and Geochemistry, Mineralogical Society of America and Geochemical Society, Chantilly, Virginia.

Kinomura, N., Kume, S., and Koizumi, M. (1975) Synthesis of $K_2SiSi_3O_9$ with silicon in 4- and 6-coordination. Mineralogical Magazine, 40, 401-404.

Konzett, J. and Fei, Y. (2000) Transport and storage of potassium in the Earth's upper mantle and transition zone: an experimental study to 23 GPa in simplified and natural bulk compositions. Journal of Petrology, 41, 583-603.

Landolt-Börnstein (1951) Physikalisch-chemische Tabellen, Vol. 2, Springer, Berlin.

Larson, A.C. and von Dreele, R.B. (2004) Generalized structure analysis system. Alamos National Laboratory Report LAUR 96-748. Los Alamos National Laboratory, New Mexico.

Leung, I.S., Guo, W., Freidman, I., and Gleanson, J. (1990) Natural occurrence of silicon carbide in a diamondiferous kimberlite from Fuxian. Nature, 346, 352-354.

Leung, I.S., Taylor, L.A., Tsao, C.S., and Han, Z. (1996) SiC in diamond and kimberlites: Implications for nucleation and growth of diamond. International Geology Review, 38, 595-606.

Likhacheva, A.Yu., Paukshtis, E.A., Seryotkin, Yu.V. and Shulgenko, S.G. (2002) IR spectroscopic characterization of NH_4-analcime. Physics and Chemistry of Minerals, 29, 617-623.

Liu, L.G. (1978) High-pressure phase transformations of albite, jadeite and nepheline. Earth and Planetary Science Letters, 37, 438-444.

Marty, B. (1995) Nitrogen content of the mantle inferred from $N_2 - Ar$ correlation in oceanic basalts. Nature, 377, 326-329.

Marty, B. and Dauphas, N. (2003a) The nitrogen record of crust-mantle interaction and mantle convection from Archean to Present. Earth and Planetary Science Letters, 206, 397-410.

Marty, B. and Dauphas, N. (2003b) Nitrogen isotopic composition of the present mantle and the Archean biosphere: Reply to comment by Pierre Cartigny and Magali Ader. Earth and Planetary Science Letters, 216, 433-439.

Massonne, H-J. and Scheyer W. (1986) High-pressure syntheses and X-ray properties of white micas in the system $K_2O - MgO - Al_2O_3 - H_2O$. Neues Jahrbuch Mineralogische Abhandlungen, 153, 177-215.

Mather, T.A., Allen, A.G., Bavison, B.M., Pyle, D.M., Oppenheimer, C., and McGonigle, A.J.S. (2004) Nitric acid from volcanoes. Earth and Planetary Science Letters, 218, 17-30.

Mathez, E.A., Fogel, R.A., Hutcheon, I.D., and Marshintsev, V.K. (1995) Carbon isotopic composition and origin of SiC from kimberlites of Yakutia, Russia. Geochimica et Cosmochimica Acta, 59, 781-791.

Melzer, S. and Wunder, B. (2000) Island-arc basalt alkali ratios: constraints from phengite-fluid partitioning experiments. Geology, 28, 583-586.

Mertz, L. (1965) Transformation in Optics. Wiley, New York.

Mingram, B. and Bräuer, K. (2001) Ammonium concentration and nitrogen isotope composition in metasedimentary rocks from different tectonometamorphic units of the European Variscan Belt. Geochimica et Cosmochimica Acta, 65, 273-287

Mohapatra, R.H. and Murty, S.V.S. (2000) Search for the mantle nitrogen in the ultramafic xenoliths from San Carlos, Arizona. Chemical Geology, 164, 305-320.

Mookherjee, M., Redfern S.A.T., Zhang, M., and Harlov, D.E. (2002a) Orientational order-disorder in synthetic ND_4/NH_4-phlogopite: a low-temperature infrared study. European Journal of Mineralogy, 14, 1033-1039.

Mookherjee, M., Redfern S.A.T., Zhang, M., and Harlov, D.E. (2002b) Orientational order-disorder of $N(D,H)_4^+$ in tobelite. American Mineralogist, 87, 1686-1691.

Moore, R.O., Otter, M.L., Rickard, R.S., Harris, J.W, and Gurney, J.J. (1986) The occurrence of moissanite and ferri-periclase as inclusions in diamond. In 4^{th} International Kimberlite Conference, Perth, Extended Abstracts; Abstract Geological Society of Australia, 16, 409-411.

Nakamoto, K. (1986) Infrared and Raman spectra of inorganic and co-ordination compounds. Wiley, New York.

Nishihara, Y., Matsukage, K.N., and Karato, S.-I. (2006) Effects of metal protection coils on thermocouple EMF in multi-anvil high-pressure experiments. American Mineralogist, 91, 111-114.

Otter, M.L. and Gurney, J.J. (1989) Mineral inclusions in diamonds from the Sloan diatreme, Colorado-Wyoming State Line Kimberlite District, North America. In Kimberlite and Related Rocks, Volume 2, Their Mantle/Crust Setting, Diamonds and Diamond Exploration; Geological Society of Australia, Special Publication, 14, p. 1042-1053, Blackwell Scientific, Cambridge, UK.

Pinti, D.L., Hashizume, K., and Matsuda, J.I. (2001) Nitrogen and argon signatures in 3.8 to 2.8 Ga metasediments: Clues on the chemical state of the Archean ocean and deep biosphere. Geochimica and Cosmochimica Acta, 65, 2301-2315.

Pitcairn, I.K., Teagle, D.A.H., Kerrich, R., Craw, D., and Brewer, T.S. (2005) The behaviour of nitrogen and nitrogen isotopes during metamorphism and mineralization: Evidence from the Otago and Alpine schists, New Zealand. Earth and Planetary Science Letters, 233, 229-246.

Poli, S. and Schmidt, M. (2002) Petrology of subducted slabs. Annual Review of Earth and Planetary Sciences, 207-235.

Pöter, B., Gottschalk, M., and Heinrich, W. (2004) Experimental determination of the K-NH_4-partitioning between muscovite, K-feldspar, and aqueous chloride solutions. Lithos, 74, 67-90.

Pöter, B., Gottschalk, M., and Heinrich, W. (2007) Crystal-chemistry of synthetic K-feldspar–buddingtonite and muscovite–tobelite solid solutions. American Mineralogist, 92, 151-165.

Quist, A.S, and Marshall W.L. (1968) Ionization equilibria in ammonia-water solutions to 700 °C and to 4000 bars of pressure. Journal of Physical Chemistry, 72, 3122-3128.

Radoslovich, E.W. and Norrish, K. (1962) The cell dimensions and symmetry of layer-lattice silicates. American Mineralogist, 47, 599-616.

Ringwood, A.E., Reid, A.F., and Wadsley, A.D. (1967) High-pressure $KAlSi_3O_8$, an aluminosilicate with sixfold coordination. Acta Crystallographica, 23, 1093-1095.

Sadofsky, S.J. and Bebout, G.E. (2000) Ammonium partitioning and nitrogen-isotope fractionation among coexisting micas during high-temperature fluid-rock interactions: Examples from the New England Appalachians. Geochimica et Cosmochimica Acta, 64, 2835-2849.

Sano, Y., Takahata, N., Nishio, Y., Fischer T.P., and Williams S.N. (2001) Volcanic flux of nitrogen from the Earth. Chemical Geology, 171, 263-271.

Schmidt, M.W. (1996) Experimental constraints on recycling of potassium from subducted oceanic crust. Science, 272, 1927-1930.

Schmidt, M. and Poli, S. (1998) Experimentally based water budgets for dehydrating slabs and consequences for arc magma generation. Earth and Planetary Science Letters, 163, 361-379.

Schmidt, M. and Ulmer, P. (2004) A rocking multianvil: elimination of chemical segregation in fluid-saturated high-pressure experiments. Geochimica et Cosmochimica Acta, 68, 1889-1899.

Schmidt, M.W., Dugnani, M., and Artioli, G. (2001) Synthesis and characterization of white micas in the join muscovite-aluminioceladonite. American Mineralogist, 86, 555-565.

Shannon, R.D. (1976) Revised effective ionic radii and systematic studies of interatomic distances in halides and chalcogenides. Acta Crystallographica, A32, 751-767.

Simakov, S.K. (1998) Redox state of upper mantle peridotites under the ancient cratons and its connection with diamond genesis. Geochimica et Cosmochimica Acta, 62, 1811-1820.

Simakov, S.K. (2006) Redox state of eclogites and peridotites from sub-cratonic upper mantle and a connection with diamond genesis. Contributions to Mineralogy and Petrology, 151, 282-296.

Skogby, H. (2006) Water in natural mantle minerals I: Pyroxenes. In H. Keppler and J.R. Smyth, Eds., Water in nominally anhydrous minerals, 62, p. 155-167. Reviews in Mineralogy and Geochemistry, Mineralogical Society of America and Geochemical Society, Chantilly, Virginia.

Swanson, D.K. and Prewitt, C.T. (1983) The crystal structure of $K_2Si^{VI}Si_3^{IV}O_9$. American Mineralogist, 68, 581-585.

Thomassot, E., Cartigny, P., Harris, J.P., and Viljoen K.S. (2007) Methane-related diamond crystallization in the Earth's mantle: Stable isotope evidences from a single diamond-bearing xenolith. Earth and Planetary Science Letters, 257, 362-371.

Thompson, P., Parsons, I. Graham, C.M., and Jackson, B. (1998) The breakdown of potassium feldspar at high water pressures. Contributions to Mineralogy and Petrology, 130, 176-186.

Truckenbrodt, J., Ziegenbein, D., and Johannes, W. (1997) The different behavior of boron nitride and unfired pyrophyllite assemblies. American Mineralogist, 82, 337-344.

Tutti, F., Dubrovinsky, L.S., Saxena S.K., and Carlson S. (2001) Stability of $KAlSi_3O_8$ hollandite-type structure in the Earth's lower mantle conditions. Geophysical Research Letters, 28, 14, 2735-2738.

Urakawa, S., Kondo, T., Igawa, N., Shimomura, O., and Ohno, H. (1994) Synchroton radiation study on the high-pressure and high-temperature phase relations of $KAlSi_3O_8$. Physics and Chemistry of Minerals, 21, 387-391.

Williams, L.B., Wilcoxon, B.R., Ferrell, R.E., and Sassen, R. (1992) Diagenesis of ammonium during hydrocarbon maturation and migration, Wilcox Group, Louisiana, USA. Applied Geochemistry, 7, 123-134.

Wunder, B. (1998) Equilibrium experiments in the system $MgO - SiO_2 - H_2O$ (MSH): stability fields of clinohumite-OH $[Mg_9Si_4O_{16}(OH)_2]$, chondrodite-OH $[Mg_5Si_2O_8(OH)_2]$ and phase A $(Mg_7Si_2O_8(OH)_6)$. Contributions to Mineralogy and Petrology, 132, 111-120.

Wunder, B., Rubie, D.C., Ross II, C.R., Medenbach, O., Seifert, F., and Schreyer, W. (1993) Synthesis, stability, and properties of $Al_2SiO_4(OH)_2$: A fully hydrated analogue of topaz. American Mineralogist, 78, 285-297.

Yagi, A., Suzuki, T., and Akaogi. M. (1994) High pressure transition in the system $KAlSi_3O_8 - NaAlSi_3O_8$. Physics and Chemistry of Minerals, 21, 12-17.

Yong, W., Dachs, E., Withers, A.C., and Essene E.J. (2008) Heat capacity and phase equilibria of wadeite-type $K_2Si_4O_9$. Contributions to Mineralogy and Petrology, 155, 137-146.

Zhang, J., Ko, J., Hazen, R.M., and Prewitt, C.T. (1993) High-pressure crystal chemistry of $KAlSi_3O_8$ hollandite. American Mineralogist, 78, 493-499.

Chapter 4

This chapter is published as

"Ammonium-bearing clinopyroxene: A potential nitrogen reservoir in the Earth's mantle"

by

Anke Watenphul, Bernd Wunder, Richard Wirth,
and Wilhelm Heinrich

in

Chemical Geology, 270, 240-248, 2010.

Ammonium-bearing clinopyroxene: A potential nitrogen reservoir in the Earth's mantle

Anke Watenphul*, Bernd Wunder, Richard Wirth, and Wilhelm Heinrich

Deutsches GeoForschungsZentrum (GFZ), Telegrafenberg, 14473 Potsdam, Germany, Section 3.3 * E-mail: watenphul@gfz-potsdam.de

Abstract

In the pseudobinary system $CaMgSi_2O_6 - (NH_4)M^{3+}Si_2O_6$, with M = Cr or Al, and NH_4OH in excess, multi-anvil experiments at 9.5 to 12.8 GPa, 725 to 750 °C produced NH_4-bearing diopside. Incorporation mainly follows the coupled substitution $(Ca^{2+})_{M2} + (Mg^{2+})_{M1} \Leftrightarrow (NH_4^+)_{M2} + (M^{3+})_{M1}$. Ammonium was identified and quantified by IR spectroscopy. In Cr-bearing diopside we found maximum concentrations in the range of 500 to 1000 ppm of NH_4.

The storage capacity of mantle clinopyroxenes for ammonium turns them to potential candidates for the nitrogen reservoir in the Earth's upper mantle, and this mechanism also contributes to its water budget. While nitrogen is transported into the mantle via cold slabs through NH_4 inherited from sedimentary material, and stored in K-bearing minerals and successor high-pressure phases, nitrogen output from the mantle is through degassing of N_2. A probable mechanism for that is that nitrogen is kept as NH_4 in clinopyroxene in the Earth's mid and lower mantle, whereas in the upper part, it is lost due to oxidation to molecular nitrogen. It is most likely that clinopyroxene plays a major role in the long-time, large-scale nitrogen cycle between surface and deep mantle of the Earth.

Keywords: Ammonium; Clinopyroxene; Nitrogen cycle; High pressure; IR spectroscopy; Earth's mantle

4.2 Introduction

Studies on the nitrogen cycle in deep Earth have shown that the input of nitrogen from the Earth's surface to depth occurs through subduction of ammonium-bearing sediments and altered oceanic crust. In most environments nitrogen is soon released to the surface via arc volcanism (e.g., Sano et al., 2001; Fischer et al., 2002) or lost during increasing metamorphic grade (Bebout and Fogel, 1992; Bebout et al., 1999; Sadofsky and Bebout, 2000; Mingram and Bräuer, 2001; Pöter et al., 2004; Plessen et al., *in revision*). By contrast, at cold slab conditions nitrogen remains in the rocks at least down to 90 km and very probably beyond the depth locus of island arc magmatism (Busigny et al., 2003a). This is because the ammonium cation, NH_4^+, inherited from organic material, has a similar ionic radius as Rb^+ and can replace K^+ in the respective K-bearing phases (e.g., Williams et al., 1992).

Experimental work has shown that the NH_4-analogues of the ultrahigh-pressure K-bearing phases phengite, K-cymrite, K-Si-wadeite, and K-hollandite are successively stable with increasing pressure – at least to 12 GPa in the case of NH_4-hollandite – provided that redox conditions are reducing enough to stabilize NH_3/NH_4^+ relative to molecular nitrogen, N_2 (Watenphul et al., 2009). This supports the idea that substantial amounts of nitrogen are recycled into the deep mantle. Busigny et al. (2003a) presented a mass balance indicating that currently about 3 to $5 \cdot 10^{10}$ mol nitrogen are annually transported to greater depths via cold slabs. At the other end of the deep nitrogen cycle, molecular nitrogen, N_2, is discharging from the Earth's mantle for a long time in hydrothermal and volcanic activities (e.g., Javoy et al., 1986; Marty, 1995). It has been suggested that the main nitrogen release would take place at mid-ocean ridges (Sano et al., 2001). Another approach ascribes the overall nitrogen output mainly to volcanic arcs (Hilton et al., 2002). As the case may be, an important issue remains unclear so far, namely if and how nitrogen could be stored to significant amounts in upper mantle assemblages, i.e., in peridotitic rocks.

Regarding the major phases in peridotites, clinopyroxene represents the most probable candidate for incorporation of NH_4. There is experimental evidence that clinopyroxene can uptake K_2O by several weight% at pressures between 7 and 14 GPa through the coupled substitution $(Ca^{2+})_{M2} + (Mg^{2+})_{M1} \Leftrightarrow (K^+)_{M2} + (M^{3+})_{M1}$ (Harlow 1997; Safonov et al., 2003; Harlow and Davies, 2004), where M^{3+} stands for Al or Cr. Omphacitic clinopyroxenes from ultrahigh-pressure rocks have been reported to uptake potassium within the same concentration range (Perchuk et al., 2002; Bindi et al., 2003). Following the rationale of NH_4 substituting K in mineral structures, it is possible that NH_4 may be incorporated into ultrahigh-pressure clinopyroxene by the same mechanism.

In this contribution we test whether high-pressure clinopyroxene is a potential host for nitrogen in the Earth's mantle by performing experiments in a multi-anvil apparatus. We will show that Cr-bearing clinopyroxene can incorporate NH_4 concentrations by up to 1000 ppm at relevant P–T conditions, and argue that its storage capacity for NH_4 might represent the nitrogen reservoir in the upper mantle. We finally speculate on the role that clinopyroxene might play during the long-time, large-scale nitrogen cycle between Earth's surface and depth.

Table 4.1. Starting materials, experimental conditions, run durations, and run products.

Run no.	$X_B^{Bulk\ a}$	P (GPa)	T (°C)	t (h)	Run products (wt%)
AW24-08	0.1	11.5	750	8	NH_4-Di (66), Stv (24), Grt (10)
AW01-09	0.1	12.8	725	5	NH_4-Di (81), Gy (10), Stv(6), En (3)
AW18-08	0.5	9.5	750	10	NH_4-Di (∼70), Gy (∼20), Grt (∼2), unkn. phase 1 (∼8)
AW23-08	0.5	11.5	750	6	NH_4-Di (53), Stv (31), Gy (13), Grt (3), Cr-Top (< 1)
AW25-08[b]	0.2	11.5	750	8	NH_4-Di (∼45), Stv (∼28), Grt (∼17), Ky (∼5), unkn. phase 2 (∼5)

Abbreviations: NH_4-Di=NH_4-bearing diopside, Stv=stishovite, Grt=garnet, Gy=guyanaite, Ky=kyanite, En=enstatite, Cr-Top=$Cr_2SiO_4(OH)_2$, unkn. phase 1=unknown phase with d = 4.87 Å, 2.67 Å, unkn.phase 2=unknown phase with d = 2.32 Å, 2.73 Å.
[a] X_B^{bulk} = proportion of hypothetical $NH_4M^{3+}Si_2O_6$ mixture in the starting bulk composition.
[b] run with Al_2O_3 instead of Cr_2O_3.

4.3 Experimental and Analytical methods

4.3.1 Synthesis

Inherent difficulties arise when NH_4-bearing minerals are synthesized at high-pressure. Using heated gels as starting materials is almost impossible, because ammonium is rapidly evaporated during heating. Thus, we used stoichiometric oxide mixtures of SiO_2, $Ca(OH)_2$, MgO, Cr_2O_3, and Al_2O_3 as starting solids. MgO, Cr_2O_3, and Al_2O_3 were pre-heated at 700 °C for several hours. Ammonium was introduced as 25% NH_4OH solution in excess. Starting bulk compositions consisted of different proportions of two mixtures, a stoichiometric diopside mixture A [$CaMgSi_2O_6$] and a hypothetic mixture B [$(NH_4)M^{3+}Si_2O_6$], with M^{3+} being either Cr or Al. Bulk compositions of the starting mixtures are listed in Table 4.1.

Stabilization of NH_4-bearing phases requires some NH_3/NH_4^+-gas pressure. Hence, excess NH_4OH solution is needed to produce a sufficiently high partial pressure of ammonia and to keep the hydrogen fugacity high, i.e., the redox conditions reducing, at least as long as the H–N–O fluid provides enough hydrogen at any given pressure and temperature. We used gold capsules surrounded by hexagonal boron nitride (h-BN) to minimize hydrogen loss during the course of the run. A detailed description of the experimental setup is given in Watenphul et al. (2009). In addition, about 4 mg of TiH_2 were placed outside of the Au-capsules as supplementary source for hydrogen, following the method of Pal'yanov et al. (2002).

Experiments were performed in a multi-anvil apparatus at 360°-rotation of the Walker-type module with a rate of 5°/s to prevent separation of fluid and solid components. We used 14/8 pressure assemblies (octahedron edge length/anvil truncation edge length). Temperature was measured using a W5%Re–W26%Re (Type C) thermocouple with a precision of about ± 10 °C. Pressure calibration was performed by press-load experiments based on several room and high-temperature phase transitions. The estimated pressure uncertainty is about ± 0.2 GPa.

By using this setup, the experimental temperatures are limited to a sample temperature of about 800 °C in the applied pressure range. This is because the actual temperatures of the h-BN spacers in direct contact with the furnace are much higher. If higher sample temperatures were applied, the h-BN spacer would undergo a phase transition to the cubic structure, which induces a large volume change and, consequently, a failure of the experiment.

After the experiments the capsules were carefully separated from the assembly material and cleaned with ethanol in an ultrasonic bath for 10 min. Analysis of any ammonium, possibly from outside contamination of the crystals due to quench fluids, is avoided by washing the run products with warm bi-distilled water and subsequent drying at 100 °C for several days.

4.3.2 Powder X-ray diffraction (XRD)

About 1 mg of the run products was ground for several minutes in an agate mortar, diluted with Elmar's white glue and spread evenly on a "zero scattering" foil. Preferential orientation of the crystals was minimized by constantly stirring the sample during the drying process. The sample was covered with an empty foil and mounted onto a transmission sample holder. Powder XRD patterns were recorded in transmission with a fully automated STOE STADI P diffractometer using CuKα_1-radiation at 40 kV and 40 mA, a take-off angle of 6°, a primary monochromator, and a 7° wide position-sensitive detector (PSD). The intensity was recorded between 5° and 125° 2θ with a detector step size of 0.1° and a resolution of 0.02°. The counting time was chosen such that the maximum intensity resulted in about 3500 to 4000 counts. The collected pattern was processed using the GSAS software package for Rietveld refinement (Larson and von Dreele, 2004) for phase identification, determination of phase proportions, and refinement of unit cell parameters. Crystal structures were taken from the Inorganic Crystal Structure Database (ICSD, FIZ Karlsruhe, http://icsdweb.FIZ-Karlsruhe.de).

The statistical parameters χ^2 and Durbin-Watson (DW) of the Rietveld refinements of the runs AW23-08, AW24-08, and AW01-09 are within the ranges of $1 < \chi^2 < 1.2$ and $1.3 < \mathrm{DW} < 1.5$. The run products AW18-08 (Cr-bearing) and AW25-08 (Al-bearing) included an unidentified phase. Phase proportions of the unknown phases in these two runs were estimated by comparison of their reflection intensities with that of all other known phases. Statistical parameters were within the ranges of $1 < \chi^2 < 1.5$ and $1.0 < \mathrm{DW} < 1.3$. The obtained unit cell parameters of all phases from these runs are reliable despite of the uncertainty in the phase proportions.

4.3.3 Infrared spectroscopy (IR)

Infrared spectroscopic measurements were carried out on KBr pellets. 2 mg of the run products were ground in an agate mortar and mixed homogeneously with 450 mg pre-dried KBr. This mixture was pressed under vacuum to 13 mm diameter pellets and dried for several days at 170 °C.

Measurements at room temperature and temperature-dependent measurements at -180 °C, 20 °C, and 200 °C were carried out with a Bruker IFS 66v FTIR spectrometer equipped with a Graseby Specac P/N 21525 variable temperature cell, respectively. We

used a globar as light source, a KBr beam splitter and a DTGS detector. The sample chamber of the interferometer was evacuated down to 200 Pa, therefore, interference of atmospheric H_2O and CO_2 was negligible.

Spectra were taken in the region from 4000 to 400 cm^{-1} with a resolution of 2 cm^{-1} and averaged over 256 scans. The interferograms were phase-corrected after the procedure of Mertz (1965) and Griffiths and de Haseth (1986). The Blackman-Harris 3-term mode was chosen as apodization function. All spectra were fitted using the program PeakFit by Jandel Scientific. Background correction was uniformly carried out in the region from 1550 to 1350 cm^{-1}, because the NH_4-ν_4 absorption band in cpx is located around 1414 cm^{-1} (see below). Absorption bands were fitted with a mixed Gaussian and Lorentzian distribution function.

NH_4 concentrations c_{NH_4} were calculated according to the Lambert–Beer-law:

$$c_{NH_4} = M_{NH_4} \times A^{\mu}_{NH_4} / (t \times \rho_{cpx} \times \epsilon^{\mu}_{N-H}) \tag{4.1}$$

where M_{NH_4} is the molecular weight of the absorbing species, t the sample thickness, ρ_{cpx} the density of the absorbing sample, ϵ^{μ}_{N-H} the molecular absorptivity of the corresponding N–H vibration at a certain wavenumber μ, and $A^{\mu}_{NH_4}$ the related absorbance in the IR spectrum corrected to 100 wt% diopside in the sample. Because molar absorption coefficients for NH_4 in pyroxenes are currently not available, their NH_4 concentrations are estimated based on a mean molecular absorptivity, which was determined for micas (Busigny et al., 2003b, Busigny et al. 2004). The plausibility of this procedure is explained below.

The thickness of the absorbing pyroxene is determined by the difference in thickness between a KBr pellet, which contains sample powder, and a pure KBr pellet. Such differential measurements were identically performed for all samples, and resulted in an averaged thickness of 20 μm. Calculations applied a density value for cpx of 3.315 g/cm^3, which is an averaged value, calculated from our Rietveld refinements.

A similar procedure was used for estimation of traces of OH concentrations of additional phases produced in the runs.

4.3.4 Electron microprobe analysis (EMP)

Polished grain mounts of each sample were analyzed using a JEOL JXA-8500F field emission electron microanalyzer in the wavelength-dispersive mode (WDS). As standards diopside (Ca, Mg, Si), Cr_2O_3 (Cr), and orthoclase (Al) were used. Nitrogen could not be measured because concentrations were below the EMP detection limit. The operation conditions were 15 kV, 10 nA, with a beam diameter of about 50 nm. On-peak counting times were 20 s for all elements. Background on both sides of the peak was measured for 10 s.

Some NH_4-bearing diopsides contained solid inclusions of a Cr-rich phase (Fig. 4.1a). The size of the inclusions was too small for EMP analysis. Special care was taken in choosing analysis spots to avoid contamination by the inclusions.

4.3.5 Transmission electron microscopy (TEM)

Thin foils of diopsides from runs AW23-08 and AW24-08 were prepared by the focused ion beam (FIB) technique (Wirth, 2009) for TEM analyses. The foils, about 8 μm × 10 μm

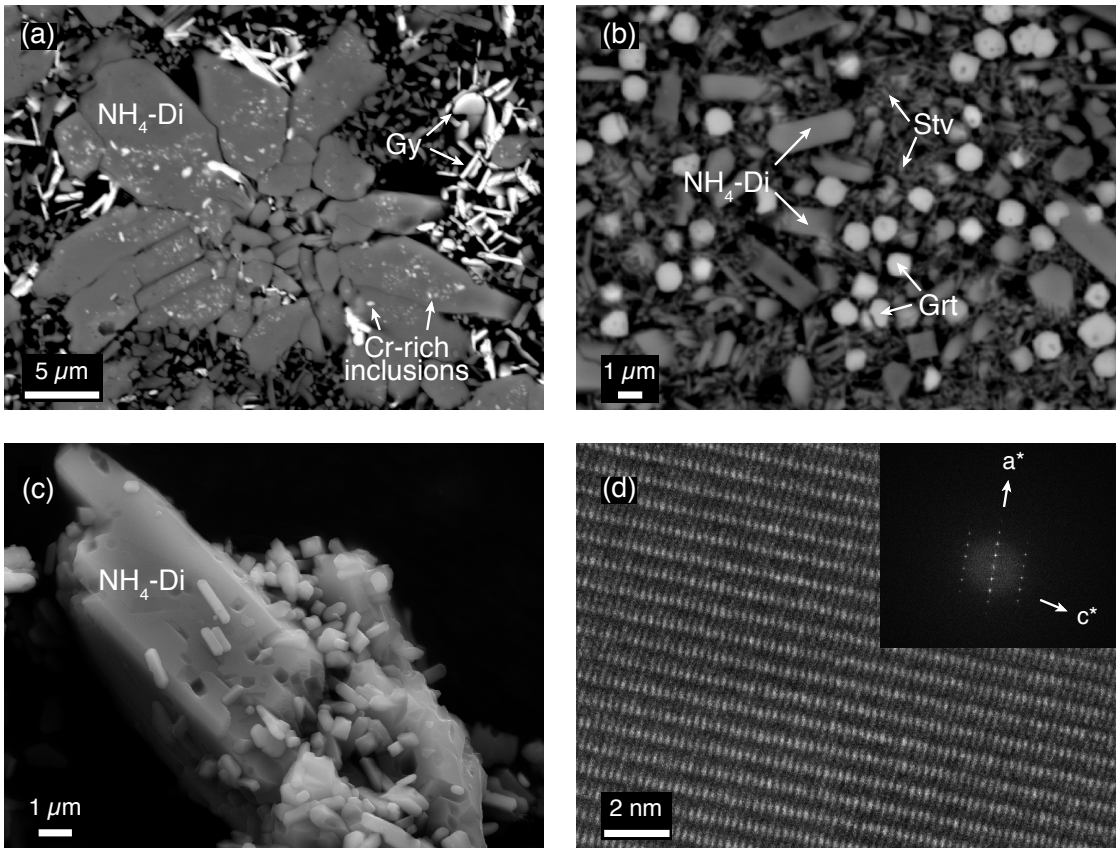

Figure 4.1: Microprobe images of the run products: (a) run AW23-08 produced diopside (large crystals) with Cr-rich inclusion, probably guyanaite. (b) run AW24-08 contains smaller inclusion-free diopside. (c) Scanning electron micrograph of run AW23-08 showing a large (10 μm) long diopside. (d) HRTEM image displaying lattice fringes of a diopside from run AW23-08, along with the corresponding SAED pattern.

in size with thickness between 100 to 200 nm, were placed on a TEM copper grid. ATEM analyses were carried out using a FEI Tecnai G^2 transmission electron microscope equipped with a field emission cathode. Operation conditions were 200 kV, condenser aperture 3, spot size 9, and a tilt angle of 20°. Beam damage of the samples was minimized by applying frames of about 150 nm × 100 nm for the energy dispersive X-ray (EDX) analyses. Counting time was 120 s.

Inclusions of the Cr-rich phase appeared also in the bright-field image overview of the diopside foil from run AW23-08 (Fig. 4.2a). Their sizes ranged from micro- to nanometers. Hence, frames set for EDX analysis were chosen from high-angle annular dark field (HAADF) images (Fig. 4.2b), so that inclusions were avoided. EDX spectra were analyzed for Mg, Si, Ca, and Cr. The data were corrected for background, absorption, and internal K_{AB}-factors using the TIA software package. The relative total errors were Mg, Ca (4 %), Si (3 %), and Cr (min. 50 %).

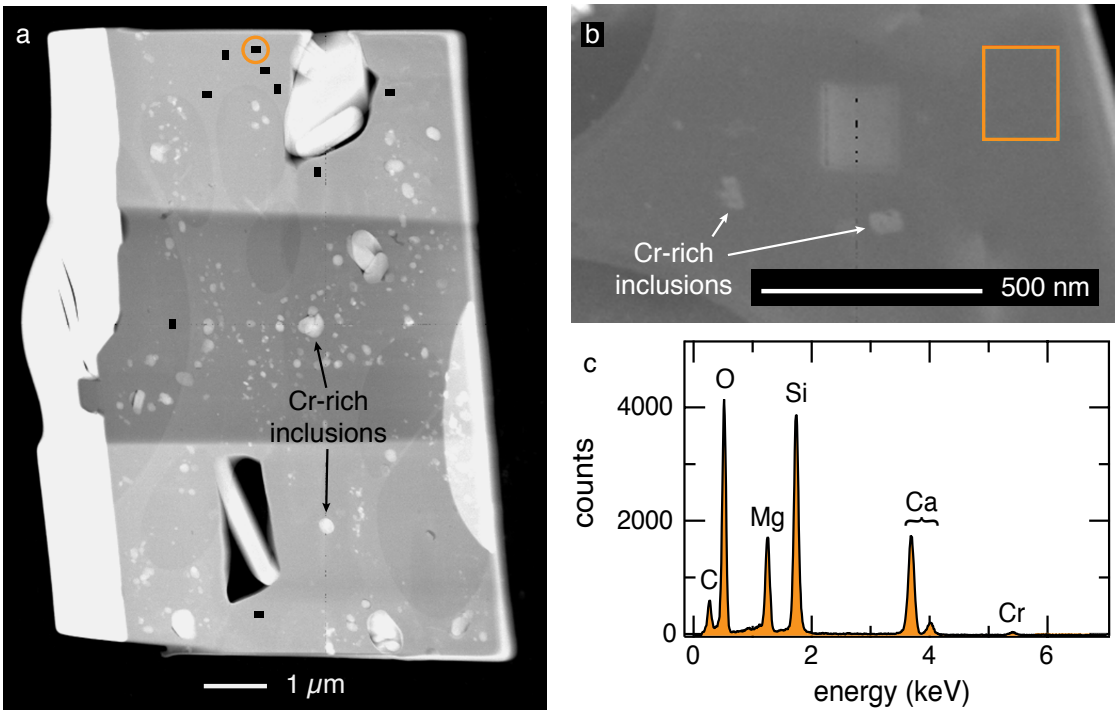

Figure 4.2: (a) Bright-field image of the FIB foil cut from a diopside of run AW23-08. Center of the foil (dark gray) is thinner than the parts above and below. Black rectangles mark positions of the EDX measurements. (b) Enlarged portion of the FIB foil. Frame indicates the encircled measuring spot in (a). (c) EDX spectrum corresponding to the frame marked in (b).

Attempts to quantify nitrogen with electron energy loss spectroscopy (EELS) were not successful. This might be due to rapid amorphization of the sample foil during spectra acquisition, concentrations not far from the detection limit, and the position of the N K-edge at the broad shoulder of the Ca K-edge. Nitrogen is a trace element here, and its K-edge is very weak compared to that of Ca. Its intensity is therefore difficult to estimate after background correction.

Thin foils were also used for high-resolution imaging of the lattice fringes of the diopsides. For that, a foil thickness of about 100 nm or less is required. Fourier transformation of high-resolution images resulted in diffraction patterns that contained the identical information as the selected area electron diffraction (SAED) patterns on the same sample foil (Fig. 4.1d).

4.3.6 Scanning electron microscopy (SEM)

A Gemini ultra high-resolution FE-SEM from Zeiss was used to characterize the reaction products (Fig. 4.1c). Individual phases with measurable sizes were identified by EDX analysis of the respective elements. The operation conditions were 20 kV, a point size beam diameter and on-spot counting times of 60 s. The resulting EDX spectra were comparable

with those determined by ATEM.

4.4 Results

The proportions of the $CaMgSi_2O_6 - (NH_4)M^{3+}Si_2O_6$ mixtures in the starting bulk compositions, experimental conditions, run durations, and relative amounts of solid run products are summarized in Table 4.1. NH_4-bearing diopside was produced in all experiments as the main solid phase with varying proportions from 45 to 81 wt% of the run products. Additional phases, identified by Rietveld refinement, are present in various amounts.

In Cr-bearing runs NH_4-bearing diopside is formed together with stishovite, garnet, which is very rich in uvarovite [$Ca_3Cr_2(SiO_4)_3$] component, and/or guyanaite [CrOOH], whereas the latter is only present if the starting bulk composition is very rich in chromium. Run AW01-09 produced minor amounts of enstatite, run AW23-08 yielded traces of the Cr end member of topaz-OH [$Cr_2SiO_4(OH)_2$]. Cr-topaz-OH was identified in the IR spectrum due to almost identical OH bands as observed for topaz-OH. The position of one of these bands is slightly shifted, and both display the identical splitting at -180 °C as observed for the Al-analogue (Watenphul and Wunder, 2009). Run AW18-08 additionally produced an unidentified phase in minor amounts (∼8 wt%).

The Al-bearing run AW25-08 produced NH_4-bearing diopside along with stishovite, garnet, rich in grossular [$Ca_3Al_2(SiO_4)_3$] component, kyanite, and small amounts of an unidentified phase (∼5 wt%).

Fig. 4.1a–c show EMP and SEM backscattered micrographs of representative run products. NH_4-bearing diopside forms idiomorphic crystals with typical monoclinic crystal shapes (Fig. 4.1c), and grain sizes varying between 1 to 25 μm. Larger crystals from runs with high Cr content in the starting mixture (runs AW18-08, AW23-08, AW01-09) contained micro- to nanometer-sized inclusions of a Cr-rich phase, which is very probable guyanaite (Fig. 4.1a). Small NH_4-bearing diopsides (run AW24-08) are free of solid inclusions (Fig. 4.1b). Accompanying phases were too small in size (1 μm and below) to be analyzed for chemical composition.

Unit cell dimensions of NH_4-bearing diopside from all samples are given in Table 4.2 along with that of a pure reference diopside, which was hydrothermally synthesized from a mixture of $CaCO_3$, MgO, and SiO_2 plus H_2O in excess at 0.3 GPa, 750 °C, and a run duration of 9 days. The a and b lattice parameters of the NH_4-bearing diopsides are slightly smaller compared to the reference diopside.

Lattice fringe images of NH_4-bearing diopsides from run AW23-08 (Fig. 4.1d) and AW24-08 showed that there are no chain multiplicity faults present. Also, the crystals are free of other defects.

Reliable EMP analyses were difficult to obtain due to problems with solid inclusions in NH_4-bearing diopside (runs AW18-08, AW23-08, and AW01-09), and the small crystal size of NH_4-bearing diopsides (runs AW24-08, AW25-08). The determined Cr and Al contents presented in Table 4.3 are associated with a relatively high degree of uncertainty and represent average values of about 15 analyses for each sample.

A typical EDX spectrum taken from the diopside foil of sample AW23-08 is shown in Fig. 4.2c. The orange square in Fig. 4.2b displays the analysis frame, which is free of solid

Table 4.2. Lattice parameters of NH_4-bearing diopsides calculated from Rietveld refinements.

Run no.	a (Å)	b (Å)	c (Å)	β (°)	V (Å^3)
Diopside[a]	9.7500(7)	8.9279(5)	5.2510(3)	105.834(6)	439.74(6)
AW24-08	9.741(1)	8.919(1)	5.2529(4)	105.861(6)	439.02(9)
AW01-09	9.739(1)	8.9178(7)	5.2530(4)	105.874(6)	438.88(7)
AW18-08	9.738(2)	8.915(2)	5.252(1)	105.89(1)	438.5(1)
AW23-08	9.732(2)	8.912(1)	5.2547(9)	105.89(1)	438.3(1)
AW25-08	9.742(2)	8.918(1)	5.2532 (7)	105.85(1)	439.1(1)

[a] single-phase diopside ($CaMgSi_2O_6$) hydrothermally synthesized at 0.3 GPa, 750 °C, run duration: 9 d.
2σ uncertainties given in parentheses apply to the last digit.

inclusions. The electron beam may cause minor damage to the foil, visible by a slightly brighter rectangle in the center of the HAADF image (Fig. 4.2b), which resulted from an earlier frame analysis. The carbon peak, visible in the spectrum, is due to the carbon coating of the foil. The observed relative intensities of Ca, Mg, Si, and O are typical for diopside. There is a significant Cr peak in all spectra, which corresponds to the concentration of 1.30(46) wt% Cr_2O_3 in AW24-08, and 0.83(40) wt% Cr_2O_3 in AW23-08 (Table 4.3). This is roughly in line with EMP analyses. Cr_2O_3 contents are averaged values over 10 analyses for each sample.

Room temperature IR spectra of the run products of all runs are presented in Fig. 4.3a. Spectra display a distinctive absorption band in the spectral region of around 1414 cm^{-1}, which is assigned to the NH_4 bending vibration ν_4 (see Watenphul et al., 2009). That this band represents indeed the NH_4-ν_4 vibration is confirmed by the shift of the band position with temperature (Fig. 4.3b). The NH_4-ν_4 vibration of runs AW23-08, AW01-09, and AW24-08, respectively, gains intensity upon cooling and shifts from 1431 cm^{-1} at -180 °C to 1397 cm^{-1} at 200 °C, typical for vibrations in which hydrogen is involved. In the vicinity of the NH_4-ν_4 band further weak bands appear at somewhat higher wavenumbers (Fig. 4.3a), which are attributed to overtones of lattice vibrations. Unlike the NH_4-ν_4 vibration, the lattice vibrations display only very minor shifts of less than 8 cm^{-1} along the

Table 4.3. NH_4 and Cr concentrations determined from IR, EMP, and ATEM, respectively.

Run no.	NH_4 (wt ppm)	Al_2O_3 (wt%)	Cr_2O_3 (wt%)	Cr_2O_3 (wt%)	NH_4 (apfu)	Al (apfu)	Cr (apfu)	Cr (apfu)
Method	IR	EMP	EMP	ATEM	IR	EMP	EMP	ATEM
AW24-08	177(80)	-	0.90(33)	1.30(46)	0.002(1)	-	0.013(3)	0.019(7)
AW01-09	428(200)	-	1.02(50)	-	0.005(2)	-	0.015(7)	-
AW18-08	481(200)	-	1.33(50)	-	0.006(2)	-	0.019(7)	-
AW23-08	1014(450)	-	1.68(36)	0.83(40)	0.012(5)	-	0.024(10)	0.012(6)
AW25-08	92(70)	1.5(7)	-	-	0.001(1)	0.017(8)	-	-

1σ-uncertainites for NH_4 and 2σ for Al/Cr concentration apply to the last digit(s).

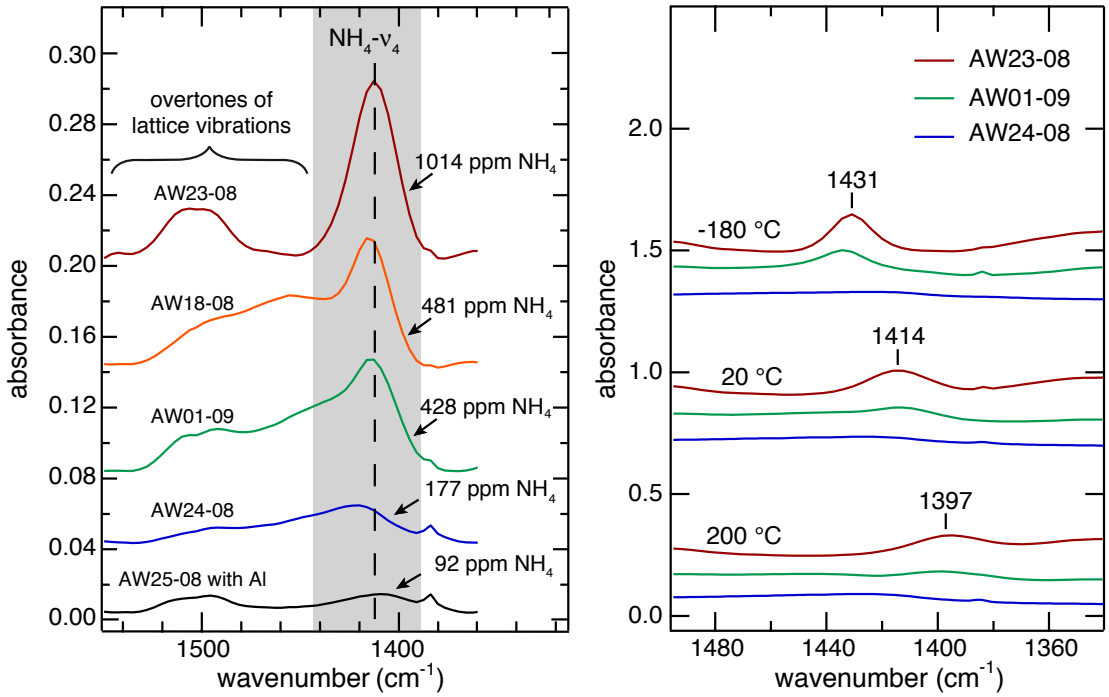

Figure 4.3: (a) Mid-infrared spectra in the spectral range from 1550 to 1360 cm^{-1} of run products from AW23-08 (1014 ppm NH_4), AW18-08 (481 ppm NH_4), AW01-09 (428 ppm NH_4), AW24-08 (177 ppm NH_4) and AW25-08 (92 ppm NH_4). Gray shaded area emphasizes the NH_4-ν_4 bending mode; vertical dashed line marks the position. (b) Mid-infrared spectra in the spectral range from 1490 to 1347 cm^{-1} of the run AW23-08, AW01-09 and AW24-08 as a function of temperature. The position (in cm^{-1}) of the NH_4-ν_4 bending mode is marked. All spectra are offset for clarity.

temperature range of -180 °C to 200 °C, and can therefore be clearly distinguished from the NH_4-ν_4 band. Because the NH_4 concentrations in diopside are low, relatively large amounts of sample material are required to obtain an NH_4 signal. Hence, the intensities of the lattice vibrations (normal modes not shown in Fig. 4.3a) are high and overtones around 1500 cm^{-1} are visible.

Diopside is the predominant solid phase in the run products and the sole one that could host small but significant amounts of NH_4. Crystal chemical constraints for clinopyroxene require charge balance for the trivalent cation, Cr^{3+}, sitting at the M1 position, and it is most plausible that this is done via incorporation of the monovalent NH_4^+ into M2, rather than by Cr^{3+} incorporation into the tetrahedral site (see below). Furthermore, it is highly unlikely that the additional phases stishovite and guyanaite could significantly incorporate NH_4^+, which is also true for the traces of kyanite in the Al-bearing sample. Wang and Takahashi (1999) showed that below 22.5 GPa garnets virtually do not uptake K_2O. Because NH_4 is only incorporated in K-bearing phases, all garnets of this study are considered ammonium-free. Minute amounts of enstatite occur in one, and minor amounts of an unknown phase

in only two samples, and these are therefore considered as not being responsible for the observed IR signal in all samples.

Thus, incorporation of NH_4^+ at the diopside M2 site accounts for the NH_4-ν_4 absorbance. If so, measured intensities allow for calculation of NH_4 concentrations. By using eq. (1), concentrations between 177 and 1014 ppm NH_4 result for the four Cr-bearing samples, and about 92 ppm for the Al-bearing sample (Table 4.3, Fig. 4.3a).

XRD patterns in combination with IR spectra provide information on additional phases in the run products. Guyanaite-containing samples AW18-08, AW23-08, and AW01-09 display small very broad and diffuse absorbances between 3670 and 3000 cm^{-1}, which are interpreted as the OH stretching bands of guyanaite. The IR spectrum of AW23-08 additionally shows two small OH stretching bands at 3600 and 3530 cm^{-1}. Upon cooling at -180 °C, the two bands split into four, revealing identical behavior as observed for topaz-OH (Watenphul and Wunder, 2009). Thus, Cr-topaz-OH must account for these bands. The IR spectrum of the Al-bearing sample AW25-08 displays a weak OH stretching band at 3563 cm^{-1}, together with broad shoulders at the low-energy wing. This band is interpreted as belonging to the OH incorporation into garnet (e.g., Beran and Libowitzky, 2006). The lattice parameter a of this garnet was determined to 11.755(1) Å, corresponding to $Grs_{81}Py_{19}$ solid solutions if a simple grossular-pyrope binary is assumed. Using an averaged molar absorption coefficient ϵ of 12500 l mol^{-1} cm^{-2} for OH in grossular-rich garnet (Maldener et al., 2003), measured intensities are converted to OH concentrations applying the procedure described above. It results that about 1000 ppm H_2O are incorporated. Samples containing uvarovite-rich garnet show no distinctive bands in the OH stretching region. Similarly, there is no hint for OH incorporation into NH_4-bearing diopsides.

4.5 Discussion

4.5.1 NH_4 concentrations and the incorporation mechanism into diopside

IR spectroscopy is the only direct method for the identification and quantification of the incorporated amount of NH_4 into diopside. The free ammonium ion, NH_4^+, has T_d symmetry resulting in four internal vibration modes, NH_4-ν_1 to NH_4-ν_4. From these, only the symmetric stretching vibration NH_4-ν_3 between 3350 and 3200 cm^{-1}, and the antisymmetric bending vibration NH_4-ν_4 around 1430 cm^{-1} are IR-active (positions from high-pressure NH_4-phases from Watenphul et al., 2009). The reported IR spectra of NH_4-bearing minerals and synthetic solid phases always display NH_4-ν_4 as the most intense vibration of the NH_4-tetrahedron. Therefore, this is probably the only vibration that is visible in IR spectra at low NH_4 concentrations. With regard to all solid phases investigated so far, the NH_4-ν_4 positions vary over about 20 cm^{-1}, due to the different crystal structures and local environments involved. In diopside, the NH_4-ν_4 band is located around 1414 cm^{-1}, at somewhat lower wavenumbers compared to other NH_4-bearing high-pressure phases such as NH_4-hollandite, NH_4-Si-wadeite, NH_4-cymrite, and NH_4-phengite(Watenphul et al., 2009) but still higher than for the free NH_4^+ cation (at 1397 cm^{-1}; Herzberg, 1966).

The unambiguous identification of the NH_4-ν_4 vibration is confirmed by heating and cooling the NH_4-bearing diopside containing samples while recording IR spectra. The bandshift of the NH_4-ν_4 vibration averages about 30 cm^{-1} between -180 and 200 °C, which is about

the same as the shift of the ND_4-ν_4* vibration in ND_4-tobelite [$(ND_4)Al_3Si_3O_{10}(OH)_2$] between -253 and 7 °C (Mookherjee et al., 2002). Compared to the relatively large bandshift of NH_4-ν_4, the lattice vibrations shift only about 5 to 8 cm^{-1} over the relevant temperature range. This is mainly because the X–O bonds (X = Si, Ca, Mg, Cr, Al) of the lattice forming atoms are much stronger than the N–H bonds of the NH_4 tetrahedron.

The NH_4 concentrations are calculated with a molar absorption coefficient of $\epsilon^{\mu}_{N-H} = 451.5 \pm 32$ l mol^{-1} cm^{-1}, which is an average value of the molar absorption coefficients of the NH_4-ν_4 bands at 1430 cm^{-1} in muscovite (Busigny et al., 2003b) and biotite (Busigny et al., 2004). The uncertainty corresponds to the minima and maxima for each value. The resulting concentrations vary between 92 and 1014 ppm NH_4 (Table 4.3). It is clear that the absorption coefficients of NH_4 in diopside and mica must be different, due to significant differences in crystal structure and density. Thus, the presented concentrations are approximate values, which can be potentially corrected once better absorption coefficients are available. A procedure to estimate a correction to the molar absorption coefficient for NH_4 in diopside would make use of the bandshift of the NH_4 stretching vibrations between muscovite/biotite and NH_4-bearing diopside. This shift would provide a measure for the difference in strength of the N–H bonds in both minerals, which directly correlates with the change of the absorption coefficient. Unfortunately, the NH_4 stretching frequencies are invisible in our spectra because NH_4 concentrations are too low. However, even if the absolute NH_4 concentrations presented in Table 4.2 and Figure 4.3 were slightly different from the "true" values, a correction would shift all values towards the same direction. Accordingly, the following considerations about the incorporation mechanism of NH_4 into diopside would still hold true.

In K-bearing clinopyroxene, potassium is incorporated into M2 via the coupled substitution $(Ca^{2+})_{M2} + (Mg^{2+})_{M1} \Leftrightarrow (K^{+})_{M2} + (M^{3+})_{M1}$. It is reasonable to assume that a similar mechanism holds also for the NH_4 incorporation. If so, the molar concentrations of NH_4 and Cr or Al, respectively, should be equal. Assuming the ideal diopside end member, the concentrations of the NH_4 and M^{3+} per formula unit (Table 4.3) are calculated under the assumptions that (1) every mol NH_4 is balanced by the equal proportion of M^{3+} and vice versa, and that (2) NH_4 substitutes for Ca in M2 and M^{3+} for Mg in M1. Fig. 4.4 shows that a coupled exchange of $(NH_4^{+})_{M2} + (M^{3+})_{M1} \Leftrightarrow (Ca^{2+})_{M2} + (Mg^{2+})_{M1}$, within error limits, is only valid for NH_4-bearing diopside produced in run AW23-08, and for Cr concentrations determined by ATEM. NH_4-bearing diopsides from other runs display somewhat lower NH_4 concentrations at similar contents of M^{3+}. Despite of the fact that the concentrations of Cr and Al in the starting compositions were very high, we measured a maximum solubility of (Cr,Al) in NH_4-bearing diopside of about 0.025 atoms pfu at the given P-T range. Saturation in the Cr, Al-bearing systems is always ensured, because the additional phases Cr-rich garnet, guyanaite or kyanite were present in the runs (Table 4.1).

The excess of M^{3+} in NH_4-bearing diopside relative to NH_4 might have several reasons: (1) The actual NH_4 concentrations have relatively large uncertainties, as our applied molar absorption coefficient for NH_4 is only a rough estimation. However, if we would evenly correct our measured intensities to higher NH_4 concentrations this would, for AW23-08, result in an NH_4 excess relative to the trivalent cation, which is highly unlikely. (2) Additional substitution mechanisms are active. Possible candidates for that are (i) the incorporation of an Ca-Eskolaite component [$Ca_{0.5}\square_{0.5}M^{3+}Si_2O_6$], or (ii) incorporation of M^{3+} into the

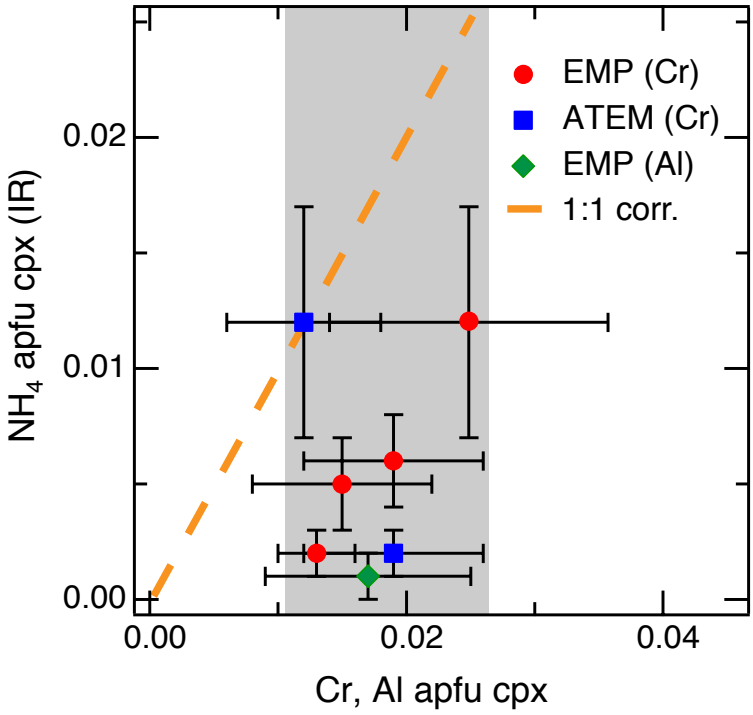

Figure 4.4: Plot of the calculated NH_4 concentrations (pfu) from IR measurements versus measured (Cr,Al) concentrations (pfu) from EMP and ATEM analyses. Gray shaded area emphasizes the measured M^{3+} concentrations within the errors. Dashed line gives the 1:1 correlation, which indicates the charge-balanced coupled substitution $NH_4^+ + M^{3+} \Leftrightarrow Ca^{2+} + Mg^{2+}$.

tetrahedron via Ca-Tschermak's substitution $[(Mg^{2+})_{M1} + (Si^{4+})_T \Leftrightarrow (M^{3+})_{M1} + (M^{3+})_T]$. Aside from that incorporation of small amounts of Mg on the Ca position is also possible, representing a small clinoenstatite component [$Mg_2Si_2O_6$]. This substitution would not explain the M^{3+} excess in most NH_4-bearing diopsides. (3) The varying NH_4 concentrations may also be due to changing redox conditions during the course of the experiments. Reducing conditions are a prerequisite for the formation of NH_3/NH_4^+ in the mineral–fluid system and for preventing oxidation to N_2. In all experiments a large excess of NH_4OH was used that kept the redox conditions sufficiently reducing. This enabled the formation of NH_4-bearing diopside in the presence of NH_3-bearing fluid. However, with our experimental setup loss of hydrogen into the pressure medium during the course of the experiment could not be completely avoided. This would imply that molecular nitrogen is produced and that the NH_3/NH_4^+ partial pressures were continuously reduced. Hence, it is possible that the NH_4-bearing diopsides in our quench products were partially decomposed, and it is not unlikely that some of the Cr-rich nanoinclusions, probably representing guyanaite, might stem from this partial decomposition process. (4) Differences in pressure might explain the different NH_4 concentrations measured in NH_4-bearing diopsides from AW23-08 (at 11.5 GPa; 1014 ppm NH_4) and AW18-08 (at 9.5 GPa; 481 ppm NH_4), for which all other variables

were identical. It would appear that within our experimental range temperature plays a minor role on the incorporation mechanism.

An important result is that the occurrence of significant amounts of OH defects in the crystal structure of the NH_4-bearing diopsides is excluded. No bands were visible in the IR spectra that could be related to OH incorporation.

The unit cell dimensions of the NH_4-bearing diopsides are very similar to the pure synthesized reference diopside (Table 4.2). Variations in their lattice parameters are very small and do not allow for further interpretation of possibly occurring substitution mechanisms. Compared to the reference diopside, all synthesized NH_4-bearing diopsides have a and b lattice parameters that are lower by about 1‰ relative. This is interpreted due to incorporation of small amounts of Mg replacing Ca on the M2 position. Unfortunately, our EMP and ATEM analytical data are not precise enough to confirm this assumption. There is no effect of structural defects on lattice parameters and chemical compositions, because high-resolution images of the lattice fringes display perfect crystals.

4.5.2 Comparison with K-bearing clinopyroxenes

There is no doubt that high pressures facilitate the incorporation of NH_4 into the diopside structure via the coupled substitution $(Ca^{2+})_{M2} + (Mg^{2+})_{M1} \Leftrightarrow (NH_4^+)_{M2} + (M^{3+})_{M1}$. The identical behavior has been observed for the analogous mechanism where K is involved instead of NH_4 (e.g., Luth, 1997; Harlow, 1997; Safonov et al., 2003; Harlow and Davies, 2004) and the extent of K incorporation indeed has been used as a geobarometer (e.g., Harlow and Veblen, 1991; Sobolev and Shatsky, 1990; Bindi et al., 2003). In comparison to NH_4, much higher amounts of K are incorporated. Experiments by Harlow (1997) at 1400 °C, 10 GPa resulted in concentrations of up to 4.7 wt% K_2O in diopside, and maximum contents at 1600 °C, 7 GPa reach about 25 mol% of Kcpx [$KM^{3+}Si_2O_6$] component (Chudinovskikh et al., 2001). The highest contents reported from a natural ultrahigh-pressure sample amount to about 17 mol% Kcpx component (Bindi et al., 2003; Harlow and Davies, 2004). Our experiments have been performed at significantly lower temperatures than that for K incorporation. However, there is overall agreement that substitution of Ca + Mg by K + M^{3+} is mainly driven by pressure and not so much by temperature (Perchuk et al., 2002; Harlow and Davies, 2004, and references therein). If so, one could speculate that higher temperatures would not induce dramatically increased NH_4 concentrations in clinopyroxenes. That NH_4 at high pressures is only incorporated as a trace component, and K as a minor or major component, might simply reflect the fact that in eight-fold coordination the ionic radius of NH_4^+ is 1.68 Å (Watenphul et al., 2009), whereas that of K^+ is 1.51 Å (Shannon, 1976). It would appear that the increase of about 10% in the ionic radius would prevent an easy incorporation of NH_4^+ into the M2 position of clinopyroxene.

There are other similarities between synthetic K- and NH_4-bearing clinopyroxenes. Cation-deficiencies in M1, i.e., Ca-Eskolaite component [$Ca_{0.5}\square_{0.5}M^{3+}Si_2O_6$], have been reported by Safonov et al. (2003; 2005), small amounts of Al-incorporation into the tetrahedron via the Ca-Tschermak's substitution $[(Mg^{2+})_{M1} + (Si^{4+})_T \Leftrightarrow (Al^{3+})_{M1} + (Al^{3+})_T]$ by Harlow (1997), Konzett and Ulmer (1999), Safonov et al. (2003, 2005), and small amounts of clinoenstatite component [$Mg_2Si_2O_6$] by Safonov et al. (2005). Harlow (1997) showed that tetrahedral substitution of Si by Cr did not occur in his experiments. Therefore, we

did not consider Cr-incorporation into the tetrahedral site as a charge balance mechanism for our NH_4-bearing diopsides.

4.5.3 Implications for nitrogen and hydrogen storage in the Earth's mantle

The Earth's mantle is continuously discharging nitrogen for a long time (Javoy et al., 1986; Marty, 1995; Sano et al., 2001). Degassing occurs mainly as molecular N_2. Currently, the estimated nitrogen supply from the Earth's interior to the atmosphere is estimated at about $3 \cdot 10^{10}$ mol/a (Hilton et al., 2002). This represents a very small amount compared to the atmospheric and biospheric nitrogen contents, which are higher by several orders of magnitude. While N_2 degassing is a fact, there is no sound notion about the nature of nitrogen reservoirs in mantle phases. A huge amount of investigations reports that diamonds can incorporate nitrogen by up to several thousands of ppm (e.g., De Corte et al., 1998; Davies et al., 2004), and nitrogen isotope ratios measured in diamonds, mantle xenoliths, basalts, and volcanic gases have been used to speculate about possible input of isotopically different nitrogen into the mantle via subducted sediments (e.g., Mohapatra and Murty, 2000; Pinti et al., 2001; Busigny et al., 2003a; Cartigny and Ader, 2003; Marty and Dauphas, 2003a,b; Mather et al., 2004; Thomassot et al., 2007). Busigny et al. (2003a) have shown that in blueschist and eclogite facies rocks from the Western Alps the entire nitrogen content inherited from organic material remained in the rocks, mainly as NH_4 in high-pressure phengites. Estimating the global nitrogen input they calculated that currently about 3 to $5 \cdot 10^{10}$ mol nitrogen per year are transported into the mantle via cold slab subduction. At pressures exceeding the upper stability of phengitic micas at 8 to 9 GPa and cold slab temperatures, NH_4 can be incorporated into successor K-bearing phases such as K-Si-wadeite and K-hollandite (Watenphul et al., 2009), which may be stable down to conditions of the transition zone and probably beyond. Our experiments indicate that clinopyroxene may also act as NH_4-bearing carrier downwards. The contribution of presumably K-Al-rich omphacitic clinopyroxene, typical of ultrahigh-pressure eclogites, for the nitrogen flux is probably minor because our experiments suggest that uptake of NH_4 into Al-bearing clinopyroxenes is in the order of 100 ppm at the relevant P–T-conditions. One can reasonably assume that ammonium would preferentially partition into K-richer phases such as K-bearing phengite, K-hollandite or K-Si-wadeite provided that the pressure conditions and the bulk compositions of the slab rocks allowed for the formation of these phases.

The estimations of nitrogen flux output, mainly as N_2 through mid ocean ridge basalts and volcanic arcs, and input as NH_4 via cold slabs, roughly balance each other (Hilton et al., 2002; Busigny et al., 2003a). Because a significant amount of nitrogen release occurs at mid-ocean ridges (Sano et al., 2001) a nitrogen reservoir in normal mantle rocks, i.e., peridotites, must be considered. Our experiments have shown that Cr-diopsides have an NH_4 storage capacity in the range of 500 to 1000 ppm, making them ideal candidates for nitrogen storage at depth. Clinopyroxene is stable throughout the most part of the upper mantle (e.g., Gasparik, 2003). A very rough estimation, using values for upper mantle thickness of 400 km, mean rock density of 3.5 g/cm^3, average cpx amount of 13 vol% (Koga et al., 2003), and mean concentration of 0.01 NH_4 pfu in cpx corresponding to about 500 ppm NH_4, results in the calculated nitrogen storage capacity of 10^{12} mol nitrogen for the whole upper mantle. This amount exceeds the annually recycled nitrogen by one and a

half order of magnitude but is still vanishingly small compared to the 10^{20} moles nitrogen present in the Earth's atmosphere and biosphere.

Input of ammonium by slab minerals and output as molecular nitrogen requires oxidation reactions to occur during the recycling process. The fate of any possible NH_4-silicate component at depths is subject to the redox conditions, of which no sound information is currently available. Oxidation reactions of the type

$$NH_4-\text{bearing phase} + O_2 \rightarrow \text{phase(s)} + 0.5\,N_2 + 2\,H_2O \tag{4.2}$$

would produce the required N_2 for degassing. Andersen et al. (1995) have shown that this actually occurs. Olivine porphyroclasts in spinel dunites from a chrome-diopside xenolith suite (Lanzarote, Canary Islands) trapped within the upper mantle have fluid inclusions containing major amounts of N_2, and some of them are pure N_2 inclusions. They interpreted that the molecular nitrogen originates from the oxidation of ammonium-bearing silicates due to increasing oxygen fugacity and/or increasing temperature, and assumed that the breakdown of phlogopite or amphibole was responsible for N_2 production. However, there is no indication of OH-bearing phases in these xenoliths, and it is quite possible that breakdown of an NH_4-bearing Cr-diopside component and oxidation to N_2 was responsible for that. Recently, Yokochi et al. (2009) reported nitrogen concentrations of mantle peridotite xenoliths from various locations worldwide. Contents amount up to 26 ppm N in phlogopite, about 0.8 ppm N in amphibole, and 0.3 ppm N in clinopyroxene, much lower than that of our synthetic diopsides from the high-pressure experiments. It is, however, important to note that these xenoliths stem from the uppermost part of the mantle, where redox conditions favor oxidation of the ammonium molecule by reaction to molecular nitrogen plus water.

NH_4 incorporation into clinopyroxene may have important implications for the water budget of the upper mantle. Water is mainly stored as OH defects in nominally anhydrous minerals. The storage capacity in upper mantle assemblages is dependent on pressure, temperature and redox conditions, and amounts from several hundred up to 4000 ppm of H_2O (e.g., Hirschmann et al., 2005; Keppler and Bolfan-Casanova, 2006; Mierdel et al., 2007). It has been experimentally shown that Cr-diopside may incorporate about 450 ppm of H_2O at upper mantle conditions (Bromiley et al., 2004), and clinopyroxenes from ultrahigh-pressure rocks may have up to 1000 ppm of H_2O (Skogby, 2006). The NH_4 component in clinopyroxene may thus significantly contribute to the upper mantle's water budget considering that, through the oxidation reaction eq. (2), one ammonium produces 0.5 N_2 + 2 H_2O, and at reducing conditions 1 NH_3 and 0.5 H_2O. Incorporation of OH^- and NH_4^+ into clinopyroxene – and potentially other mantle phases – depends, among other parameters, on the partial pressures of H_2O and NH_3. If the oxygen fugacity, f_{O_2}, is buffered by FMQ, any H–N–O fluid at relevant upper mantle conditions will consist of H_2O and N_2 (Churakov and Gottschalk, 2003a,b; and unpublished calculations; see also Simakov 1998). Fluid species rapidly change to NH_3 + H_2O at f_{O_2} of about 3 log units below FMQ. Along a normal upper mantle geotherm, increasing pressure would favor formation of NH_3. Frost and McCammon (2008) have shown that oxygen fugacities prevailing in the upper part of the upper mantle, i.e., in spinel lherzolites, are between ΔFMQ -2 and +2 log units, whereas they gradually decrease with depth attaining values of -3 to -4 log units at 4 to 6 GPa below the cratonic lithosphere, and may attain -5 log units at 8 GPa. It would thus appear that in the lower part of the upper mantle NH_3/NH_4^+ predominates in H–N–O fluids, and therefore may sta-

bilize the NH_4-component in clinopyroxene relative to N_2 plus water. Still, the contribution to the mantle's water content may be significant. If one follows this speculation, it would imply that ammonium is stored within the lower part of the upper mantle, and that some transition region would exist where pressure decrease and f_{O_2} increase would allow for gradual oxidation of the NH_4-bearing component by reaction (2). If so, this process is expected to occur somewhere in the mid-upper mantle. Qualitatively, it provides a reasonable explanation for the fact that nitrogen input – and storage – into the mantle occurs via subducted ammonium, and degassing via molecular nitrogen.

4.6 Conclusions

Our experiments show that at high pressure and reducing conditions allowing for stabilization of NH_3/NH_4^+ in H–N–O fluids ammonium, NH_4, is incorporated into diopside by the coupled substitution $(Ca^{2+})_{M2} + (Mg^{2+})_{M1} \Leftrightarrow (NH_4+)_{M2} + (M^{3+})_{M1}$. For Cr-diopside, the amount of nitrogen incorporation attains concentrations of NH_4 by up to 1000 ppm at 11.5 GPa, 750 °C. This makes clinopyroxene potentially an important carrier of ammonium in upper mantle rocks, i.e., in clinopyroxene-bearing peridotites.

Nitrogen is transported into the mantle via cold slabs through ammonium inherited from sedimentary material that is stored in K-bearing minerals, mainly micas. NH_4 remains in subducted rocks by continuous redistribution into newly formed high-pressure K-bearing phases such as phengite, K-Si-wadeite, K-hollandite, and K-Al-rich clinopyroxenes. At the other end of the deep nitrogen cycle, the mantle releases molecular nitrogen, N_2, through degassing. This occurs most probably due to oxidation of the NH_4 component in clinopyroxene at mid-upper mantle conditions. Thus, the stability of ammonium as a component in subducted slabs and mantle phases is very important for long-time, large-scale recycling of nitrogen and hydrogen between the Earth's crust and the deeper mantle.

Acknowledgements

We thank HP. Nabein and R. Schulz for technical assistance, A. Schreiber for preparation of the FIB-foils, G. Berger for preparation of the EMP samples, O. Appelt for help with the EMP work and H. Kemnitz for assistance at the SEM. Constructive reviews by V. Busigny and an anonymous reviewer helped to improve the manuscript and are highly appreciated. We thank B. Bourdon for the effective editorial handling of the manuscript. This work was supported by the German Science Foundation [He 2015/(8-1)] within the framework of the Priority Program 1236 "Structures and properties of crystals at extreme pressures and temperatures", which is gratefully acknowledged.

4.7 References

Andersen, T., Burke, E.A.J., Neumann, E.-R., 1995. Nitrogen-rich fluid in the upper mantle: fluid inclusions in spinel dunite from Lanzarote, Canary Islands. Contributions to Mineralogy and Petrology 120 (1), 20-28.

Bebout, G.E., Fogel, M.L., 1992. Nitrogen-isotope compositions of metasedimentary rocks in the Catalina schists, California: Implications for metamorphic devolatilization history. Geochimica et Cosmochimica Acta 56 (7), 2839-2849.

Bebout, G.E., Cooper, D.C., Bradley, A.D., Sadofsky, S.J., 1999. Nitrogen-isotope record of fluid-rock interactions in the Skiddaw aureole and granite, English Lake District. American Mineralogist 84, 1495-1505.

Beran, A., Libowitzky, E., 2006. Water in mantle minerals II: Olivine, garnet and accessory minerals. In: Keppler, H., and Smyth, J.R. (Eds.), Water in nominally anhydrous minerals. Reviews in Mineralogy and Geochemistry, vol. 62. Mineralogical Society of America and Geochemical Society, Chantilly, Virginia, pp. 169-191.

Bindi, L., Safonov, O.G., Litvin, Y.A., Perchuk, L.L., Menchetti, S., 2002. Ultrahigh potassium content in the clinopyroxene structure: an X-ray single crystal study. European Journal of Mineralogy 14 (5), 929-934.

Bindi, L., Safonov, O.G., Yapaskurt, V.O., Perchuk, L.L., Menchetti, S., 2003. Ultrapotassic clinopyroxene from the Kumdy-Kol microdiamond mine, Kokchetav Complex, Kazakhstan: Occurrence, composition and crystal-chemical characterization. American Mineralogist 88, 464-468.

Bromiley, G.D., Keppler, H., McCammon, C., Bromiley, F.A., Jacobsen, S.D., 2004. Hydrogen solubility and speciation in natural, gem-quality chromian diopside. American Mineralogist 89, 941-949.

Busigny, V., Cartigny, P., Philippot, P., Ader, M., Javoy, M., 2003a. Massive recycling of nitrogen and other fluid-mobile elements (K, Rb, Cs, H) in a cold slab environment: evidence from HP to UHP oceanic metasediments of the Schistes Lustrés nappe (western Alps, Europe). Earth and Planetary Science Letters 215 (1-2), 27-42.

Busigny, V., Cartigny, P., Philippot, P., Javoy, M., 2003b. Ammonium quantification in muscovite by infrared spectroscopy. Chemical Geology 198 (1-2), 21-31.

Busigny, V., Cartigny, P., Philippot, P., Javoy, M., 2004. Quantitative analysis of ammonium in biotite using infrared spectroscopy. American Mineralogist 89, 162-1630.

Cartigny, P., Ader, M., 2003. A comment on "The nitrogen record of crust-mantle interaction and mantle convection from Archean to Present" by B. Marty and N. Dauphas. Earth and Planetary Science Letters 206 (3-4), 397-410.

Chudinovskikh, L.T., Zharikov, V.A., Ishbulatov, R.A., Matveev, Y. A., 2001. Mechanism of ultrahigh potassium content incorporation into high-pressure clinopyroxene. Doklady Earth Sciences 381 (8), 956-959.

Churakov, S.V., Gottschalk, M., 2003a. Perturbation theory based equation of state for polar molecular fluids: I. Pure fluids. Geochimica et Cosmochimica Acta 67 (13), 2397-2414.

Churakov, S.V., Gottschalk, M., 2003b. Perturbation theory based equation of state for polar molecular fluids: II. Fluid mixtures. Geochimica et Cosmochimica Acta 67 (13), 2415-2425.

Davies, R.M., Griffin, W.L., O'Reilly, S.Y., McCandless, T.E., 2004. Inclusions in diamonds from the K14 and K10 kimberlites, Buffalo Hills, Alberta, Canada: diamond growth in a plume? Lithos 77 (1-4), 99-111.

De Corte, K., Cartigny, P., Shatsky, V.S., Sobolev, N.V., Javoy, M., 1998. Evidence of fluid inclusions in metamorphic microdiamonds from the Kokchetav massif, northern Kazakhstan. Geochimica et Cosmochimica Acta 62 (23-34), 3765-3773.

Fischer, T.P., Hilton, D.R., Zimmer, M.M., Shaw, A.M., Sharp, Z.D., Walker, J.A., 2002. Subduction and recycling of nitrogen along the Central American Margin. Science 297 (5584), 1154-1157.

Frost, D.J., McCammon, C.A., 2008. The redox state of Earth's mantle. Annual Review of Earth and Planetary Sciences 36, 389-420.

Gasparik, T., 2003. Phase diagrams for geoscientists – An atlas of the Earth's interior. Springer.

Griffiths, P.R., de Haseth, J.A., 1986. Fourier transform infrared spectroscopy. John Wiley and Sons. New York.

Harlow, G.E., 1997. K in clinopyroxene at high pressure and temperature: An experimental study. American Mineralogist 82, 259-269.

Harlow, G.E., Davies R.M., 2004. Status report on stability of K-rich phases at mantle conditions. Lithos 77, 647-653.

Harlow, G.E., Veblen, D.R., 1991. Potassium in clinopyroxene inclusions from diamonds. Science 251 (4994), 662-665.

Herzberg, G., 1966. Molecular spectra and molecular structure Vol.2: Infrared and Raman spectra of polyatomic molecules. Van Nostrand, Princton.

Hilton, D.R., Fischer, T.P., Marty, B., 2002. Noble gases and volatile recycling at subduction zones. In: Porcelli, D.P., Ballentine, C.J., and Wieler, R. (Eds.), Noble Gases – In geochemistry and cosmochemistry. Reviews in Mineralogy and Geochemistry, vol. 47. Mineralogical Society of America and Geochemical Society, Chantilly, Virginia, pp. 319-370.

Hirschmann, M.M., Aubaud, C., Withers, A., 2005. Storage capacity of H_2O in nominally anhydrous minerals in the upper mantle. Earth and Planetary Science Letters 236 (1-2), 167-181.

Javoy, M., Pineau, F., Delorme, H., 1986. Carbon and nitrogen isotopes in the mantle. Chemical Geology 57 (1-2), 41-62.

Keppler, H., Bolfan-Casanova, N., 2006. Thermodynamics of water solubility and partitioning. In: Keppler, H., and Smyth, J.R. (Eds.), Water in nominally anhydrous minerals. Reviews in Mineralogy and Geochemistry, vol. 62. Mineralogical Society of America and Geochemical Society, Chantilly, Virginia, pp. 193-230.

Koga, K., Hauri, E., Hirschmann, M., Bell, D., 2003. Hydrogen concentration analyses using SIMS and FTIR: Comparison and calibration for nominally anhydrous minerals. Geochemistry, Geophysics, Geosystems 4 (2), doi: 10.1029/2002GC000378.

Konzett, J., Ulmer, P., 1999. The stability of hydrous potassic phases in lherzolitic mantle – an experimental study to 9.5 GPa in simplified and natural bulk compositions. Journal of Petrology 40 (4), 629-652.

Larson, A.C., von Dreele, R.B., 2004. General structure analysis system (GSAS). Los Alamos National Laboratory Report LAUR, pp. 86-748.

Luth, R.W., 1997. Experimental study of the system phlogopite-diopside from 3.5 to 17 GPa. American Mineralogist 82, 1198-1209.

Maldener, J., Hösch, A., Langer, K., Rauch, F., 2003. Hydrogen in some natural garnets studied by nuclear reaction analysis and vibrational spectroscopy. Physics and Chemistry of Minerals 30, 337-344.

Marty, B., 1995. Nitrogen content of the mantle inferred from N_2-Ar correlation in oceanic basalts. Nature 377 (6547), 326-329.

Marty, B., Dauphas, N., 2003a. The nitrogen record of crust-mantle interaction and mantle convection from Archean to Present. Earth and Planetary Science Letters 206 (3-4), 397-410.

Marty, B., Dauphas, N., 2003b. Nitrogen isotopic composition of the present mantle and the Archean biosphere: Reply to comment by Pierre Cartigny and Magali Ader. Earth and Planetary Science Letters 216 (3), 433-439.

Mather, T.A., Allen, A.G., Bavison, B.M., Pyle, D.M., Oppenheimer, C., McGonigle, A.J.S., 2004. Nitric acid from volcanoes. Earth and Planetary Science Letters 218 (1-2), 17-30.

Mertz, L., 1965. Transformations in optics. Wiley, New York.

Mierdel, K., Keppler, H., Smyth, J.R., Langenhorst, F., 2007. Water solubility in aluminous orthopyroxene and the origin of Earth's asthenosphere. Science 315 (5836), 364-368.

Mingram, B., Bräuer, K., 2001. Ammonium concentration and nitrogen isotope composition in metasedimentary rocks from different tectonometamorphic units of the European Variscan Belt. Geochimica et Cosmochimica Acta 65 (2), 273-287.

Mohapatra, R.K., Murty, S.V.S., 2000. Search for the mantle nitrogen in the ultramafic xenoliths from San Carlos, Arizona. Chemical Geology 164 (3-4), 305-320.

Mookherjee, M., Redfern, S.A.T., Zhang, M., Harlov, D.E., 2002. Orientational order-disorder of $N(D,H)_4^+$ in tobelite. American Mineralogist 87, 1686-1691.

Pal'yanov, Y.N., Sokol, A.G., Borzdov, Y.M., Khokhryakov, A.F., Sobolev, N.V., 2002. Diamond formation through carbonate-silicate interaction. American Mineralogist 87, 1009-1013.

Perchuk, L.L., Safonov, O.G., Yapaskurt, V.O., Barton Jr., J.M., 2002. Crystal-melt equilibria involving potassium-bearing clinopyroxene as indicator of mantle-derived ultrahigh-potassic liquids: an analytical review. Lithos 60 (3-4), 89-111.

Pinti, D.L., Hashizume, K., Matsuda, J.I., 2001. Nitrogen and argon signatures in 3.8 to 2.8 Ga metasediments: Clues on the chemical state of the Archean ocean and deep biosphere. Geochimica and Cosmochimica Acta 65 (14), 2301-2315.

Plessen, B., Harlov, D.E., Henry, D., Guidotti, C.V. Ammonium loss and nitrogen isotopic fractionation in biotite as a function of metamorphic grade in metapelites from western Maine, USA. In revision.

Pöter, B., Gottschalk, M., Heinrich, W., 2004. Experimental determination of the K-NH_4-partitioning between muscovite, K-feldspar, and aqueous chloride solutions. Lithos 74 (1-2), 67-90.

Sadofsky, S.J., Bebout, G.E., 2000. Ammonium partitioning and nitrogen-isotope fractionation among coexisting micas during high-temperature fluid-rock interactions: Examples from the New England Appalachians. Geochimica et Cosmochimica Acta 64 (16), 2835-2849.

Safonov, O.G., Litvin, Y.A., Perchuk, L.L., Bindi, L., Menchetti, S., 2003. Phase relations of potassium-bearing clinopyroxene in the system $CaMgSi_2O_6 - KAlSi_2O_6$ at 7 GPa. Contributions to Mineralogy and Petrology 146 (1), 120-133.

Safonov, O.G., Perchuk, L.L., Litvin, Y.A., Bindi, L., 2005. Phase relations in the $CaMgSi_2O_6 - KAlSi_2O_6$ join at 6 and 3.5 GPa as a model for formation of some potassium-bearing deep-seated mineral assemblages. Contributions to Mineralogy and Petrology 149 (3), 316-337.

Sano, Y., Takahata, N., Nishio, Y., Fischer T.P., Williams S.N., 2001. Volcanic flux of nitrogen from the Earth. Chemical Geology 171 (3-4), 263-271.

Shannon, R.D., 1976. Revised effective ionic radii and systematic studies of interatomic distances in halides and chalcogenides. Acta Crystallographica A32, 751-767.

Simakov, S.K., 1998. Redox state of upper mantle peridotites under the ancient cratons and its connection with diamond genesis. Geochimica et Cosmochimica Acta 62 (10), 1811-1820.

Skogby, H., 2006. Water in natural mantle minerals I: Pyroxenes. In: Keppler, H., and Smyth, J.R. (Eds.), Water in nominally anhydrous minerals. Reviews in Mineralogy

and Geochemistry, vol. 62. Mineralogical Society of America and Geochemical Society, Chantilly, Virginia, pp. 155-167.

Sobolev, N.V., Shatsky, V.S., 1990. Diamond inclusions in garnets from metamorphic rocks: a new environment for diamond formation. Nature 343 (6260), 742-746.

Thomassot, E., Cartigny, P., Harris, J.P., Viljoen K.S., 2007. Methane-related diamond crystallization in the Earth's mantle: Stable isotope evidences from a single diamond-bearing xenolith. Earth and Planetary Science Letters 257 (3-4), 362-371.

Wang, W., Takahashi, E., 1999. Subsolidus and melting experiments of a K-rich basaltic composition to 27 GPa: Implication for the behavior of potassium in the mantle. American Mineralogist 84, 357-361.

Watenphul, A., Wunder, B., 2009. Temperature-dependence of the OH-stretching frequencies in topaz-OH. Physics and Chemistry of Minerals, doi 10.1007/s00269-009-0310-6.

Watenphul, A., Wunder, B., Heinrich, W., 2009. High-pressure ammonium-bearing silicates: Implications for nitrogen and hydrogen storage in the Earth's mantle. American Mineralogist 94, 283-292.

Williams, L.B., Wilcoxon, B.R., Ferrell, R.E., Sassen, R., 1992. Diagenesis of ammonium during hydrocarbon maturation and migration, Wilcox Group, Louisiana, USA. Applied Geochemistry 7 (2), 123-134.

Wirth, R., 2009. Focused Ion Beam (FIB) combined with SEM and TEM: Advanced analytical tools for studies of chemical composition, microstructure and crystal structure in geomaterials on a nanometre scale. Chemical Geology 261 (3-4), 217-229.

Yokochi, R., Marty, B., Chazot, G., Burnard, P., 2009. Nitrogen in peridotite xenoliths: Lithophile behavior and magmatic isotope fractionation. Geochimica et Cosmochimica Acta 73, 4843-4861.

Chapter 5

This chapter is published as

"Temperature dependence of the OH-stretching frequencies in topaz-OH"

by

Anke Watenphul and Bernd Wunder

in

Physics and Chemistry of Minerals, 37, 65-73, 2010.

Temperature dependence of the OH-stretching frequencies in topaz-OH

Anke Watenphul and Bernd Wunder

Deutsches GeoForschungsZentrum (GFZ), Telegrafenberg, 14473 Potsdam, Germany,
Section 3.3 email: watenphul@gfz-potsdam.de

Abstract

Hydrogen bonding in topaz-OH, $Al_2SiO_4(OH)_2$, was investigated by IR spectroscopic analysis of the temperature dependence of the OH-stretching frequencies. Low-temperature spectra ranging from –196 to –160°C prove the existence of four non-equivalent H-positions in the crystal structure from the occurrence of four different OH-bands. With increasing temperature, these bands merge first, above –160°C, into two OH-bands and then above 400°C into one asymmetric broad band. Shifting of the OH-bands is caused by thermally induced hydrogen order–disorder. Low temperature fixes the protons in their positions; increasing temperature induces proton movement and allows switching between the different positions. Autocorrelation analysis of the IR spectra reveals two phase transitions, one at about –155°C from *P1* to $Pbn2_1$ characterized as static–dynamic change and the second at about 380°C from $Pbn2_1$ to *Pbnm* caused by disordering of the protons. The increasing symmetry with temperature is due to advanced proton movement and dynamical averages over the proton distribution densities.

Keywords Topaz-OH · IR spectroscopy · Autocorrelation analysis · Order–disorder phase transition

5.2 Introduction

Topaz, $Al_2SiO_4(F,OH)_2$, is a well-known hydrous mineral in aluminous and fluorine-rich rocks occurring in near-surface environments (e.g., Ribbe 1982); less often it is also found in low-temperature, high- to ultrahigh-pressure metamorphic rocks (Theye 1988; Zhang et al. 2002). The range of the (OH,F)-solid solution was previously thought to be limited up to $X_{OH} = 0.5$ [$X_{OH} = OH/(OH + F)$] due to proton–proton avoidance (Barton 1982). However, finding of OH-rich topaz with $X_{OH} = 0.55$ in samples from ultrahigh-pressure rocks of the Sulu terrane, eastern China (Zhang et al. 2002), as well as experimental studies at high pressure indicate that depending on the P–T–X-conditions, topaz might be stable along the complete (OH,F)-solid solution series (Wunder et al. 1993, 1999). The existence of topaz with $X_{OH} = 1.0$ was first predicted from energy calculations (Abbott 1990) and confirmed later by high-pressure synthesis (Wunder et al. 1993). Since then, the fully hydrated end-member of topaz, $Al_2SiO_4(OH)_2$, is termed topaz-OH. The stability of topaz-OH in the $Al_2O_3 - SiO_2 - H_2O$–system has been reported at pressures between 5.5 and 13 GPa and temperatures up to 1,500°C (Wunder et al. 1993; Ono 1999). Topaz-OH is suggested to be an important water carrier in pelitic sediments and basaltic rocks, which are subducted to depths below 150 km (Schreyer 1995; Schmidt 1995; Domanik and Holloway 1996; Ono 1998).

The hydrogen-bonding geometry of topaz-OH is controversial discussed. X-ray studies of topaz-OH and its deuterated analog, topaz-OD, using single crystal X-ray (Northrup et al. 1994) and neutron powder diffraction (Chen et al. 2005; Komatsu et al. 2008) indicated that hydrogen is located in two non-equivalent sites. In contrast to that, Churakov and Wunder (2004) predicted the existence of four non-equivalent proton positions, H1–H4, from ab initio quantum mechanical calculations. At ambient conditions, the four protons are in dynamic exchange between the allowed positions of local minima. Flipping of the protons between different sites is achieved by simple rotation of the OH-dipole between the closely adjacent H4 and H1 as well as H3 and H2 positions, which corresponds to the two observed OH-bands in the IR spectrum, respectively. This prediction is supported by NMR- and Raman investigations on topaz-OH (Xue et al. 2006).

The aim of the present work is to clarify the OH-bonding geometry in topaz-OH and its temperature dependence using IR spectroscopy and the autocorrelation method.

5.3 Experimental and analytical techniques

5.3.1 Experimental setup

For synthesis of topaz-OH, we used a stoichiometric $Al_2O_3 - SiO_2$–gel plus 20 wt% of bidistilled water as starting materials. The gel was dried for 1 h at 700°C before usage. The gel and fluid were loaded into a gold capsule, which was then cold-welded. Topaz-OH was synthesized in a rotating multi-anvil apparatus at 900°C, 10 GPa, and a run duration of 50 h. To prevent separation of fluid and solid components, experiments were performed at 360°-rotation of the Walker-type module with a speed of 5°/s. The experiment was performed with a 14/8 assembly (octahedron edge length/anvil truncation edge length). The temperature was measured using a W5%Re–W26%Re (Type C) thermocouple with a pre-

cision of about ±10°C. The pressure calibration was performed by press–load experiments based on room and high-temperature phase transitions. The estimated pressure uncertainty is about ±0.2 GPa. A detailed description of the synthesis method and the assembly set up is given in Watenphul et al. (2009). After the experiment, the capsule was separated from the assembly material, cleaned in an ultrasonic bath for 10 min in ethanol and then carefully opened.

5.3.2 Analytical methods

Powder X-ray diffraction

The run product was characterized by powder X-ray diffraction (XRD) in the 2θ–range 5–125° using a STOE STADI P diffractometer with a CuKα_1-radiation source. The collected pattern was processed using the GSAS software package for Rietveld refinement (Larson and von Dreele 2004) for phase identification and refinement of unit cell parameters.

IR spectroscopy

The topaz-OH crystals were up to about 10 μm × 25 μm in size, which is too small for a single-crystal IR analysis. Therefore, about 0.5 mg of the crystals was powdered in an agate mortar. Subsequently, a small pinch of the powder was spread on one diamond of a diamond anvil cell (DAC). The DAC was closed and the powder was pressed to a thin film with a pressure of about 2–3 GPa. This preparation method has several advantages: (1) the sample film has a constant thickness, which can be used to calculate the OH concentration with the Lambert–Beer-law and (2) any possible preferred orientation of the crystals is minimized. The film was then mounted on a glass carrier. The film thickness was determined to 3 ± 0.5 μm by analysis of video images using the program OPUS by Bruker. The film on the glass carrier was then mounted into a Linkam FTIR600 heating/freezing stage.

Unpolarized IR spectra were collected in the spectral range 4,000–3,000 cm^{-1} between –196 and 600°C using a Bruker IFS 66v FTIR spectrometer and a Hyperion IR microscope. The resolution was 1 cm^{-1} using a Globar light source, a KBr beamsplitter and a MCT-detector. The spectra were taken with an aperture of 40 μm × 40 μm and averaged over 256 scans. The interferograms were phase-corrected after the procedure of Mertz (1965) and Griffiths and de Haseth (1986). Blackman–Harris 3-term mode was chosen as apodization function. The measured spectra were transformed into absorption spectra. After background correction, the band center and the full width at half band maximum (FWHM) of each band were determined using the program *PeakFit* by Jandel Scientific.

Autocorrelation analysis

In case of vibrational spectroscopy, the band position, band intensity and bandwidth are known to correlate with the square of the order parameter Q from Landau theory (Salje et al. 2000). Especially in case of dynamic order–disorder transitions, the investigation of bandwidths has proven versatile, whereas changes in band positions and intensities were found to be not that sensitive (Libowitzky and Beran 2004).

To obtain an effective linewidth of the OH-bands of topaz-OH, we used the autocorrelation method (Salje et al. 2000). Therefore, the spectral region 3,650–3,420 cm^{-1} has been selected as the appropriate segment of each primary IR spectrum. A suitable linear baseline between these end points was subtracted from each spectrum. Then, each segment was correlated with itself using the autocorrelation function

$$Corr(\alpha, \omega') = \int \alpha(\omega + \omega')\alpha(\omega)d\omega \tag{5.1}$$

to produce an autocorrelated spectrum (Salje et al. 2000). The width of the central peak of each autocorrelation spectrum varies with the general width of the bands of the primary IR spectrum. Therefore, it contains the combined information of the linewidth of the overlapping sequence of bands. Within the limit $\omega \rightarrow 0$ the width of the central peak contains the quantitative information of the primary linewidths, which can be extracted by extrapolation. We fitted a Gaussian curve to the central peak around the offset $\omega' = 0$ for successive ranges of ω' between 8 and 30 cm^{-1}. ΔCorr, the FWHM of the Gaussian curve at $\omega' = 0$, is derived by extrapolation using a fourth-order polynomial.

5.4 Results

5.4.1 Powder X-ray diffraction

The run products were characterized by powder XRD at room temperature. Topaz-OH was the sole solid phase found. As initial crystal structure for the structure refinement, we took the data reported by Northrup et al. (1994) from the Inorganic Crystal Structure Database (ICSD, FIZ Karlsruhe, http://icsd.FIZ-karlsruhe.de). The refined unit cell parameters were $a = 4.7278(2)$ Å, $b = 8.9302(5)$ Å, $c = 8.4264(4)$ Å and $V = 355.77(3)$ $Å^3$, 2σ–uncertainties given in parentheses. The space group (SG) used for the refinement was *Pbnm*. The obtained values are in good agreement with the data reported by Wunder et al. (1993) and Northrup et al. (1994).

5.4.2 Temperature-dependent IR spectroscopy

IR spectra of the OH-stretching region at 3,740–3,340 cm^{-1} are shown in Fig. 5.1a for selected temperatures between –196 and 600°C. At room temperature two OH-bands at 3,602 cm^{-1} (ν_1) and 3,525 cm^{-1} (ν_2) are present, together with an unresolved shoulder at the low-energy wing of ν_2 (Wunder et al. 1993, 1999). With increasing temperature, both bands broaden and the band centers approach each other so that at 600°C only one asymmetric broad band at about 3,580 cm^{-1} is visible. The behavior in the low-temperature range, –196 to 30°C, is shown in Fig. 5.1b. The band's shape gets more distinct at lower temperatures and the shoulder at the low-energy wing of ν_2 becomes increasingly pronounced. The center of ν_1 remains unaffected, whereas ν_2 shifts toward lower wavenumbers. At about –160°C the shape of both bands flattens at the top and two plateaus form, of which each splits with further decreasing temperature into two bands (Fig. 5.1b). At –196°C one can clearly distinguish between four different bands: ν_{1a}, ν_{1b}, and ν_{2a}, ν_{2b}. Both effects, band splitting at low temperature as well as overlapping of the two bands ν_1 and ν_2 at high temperature, are reversible during heating and cooling along the entire temperature range.

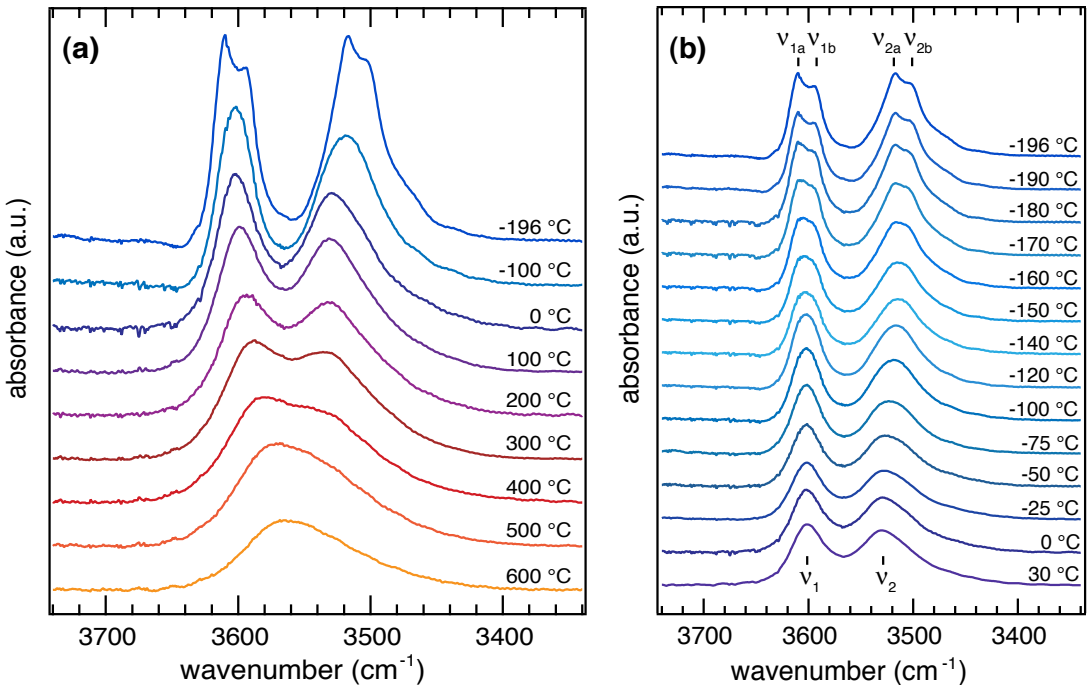

Figure 5.1: **a** IR spectra of topaz-OH in the spectral region of the OH-stretching vibrations at selected temperatures between –196 and 600°C. **b** IR spectra of topaz-OH in the same spectral region with focus on low temperature between –196 and 30°C. All spectra are offset for clarity.

Band positions and FWHMs of the low-temperature spectra (Fig. 5.1b) were determined by peak fitting of the absorption bands in the OH-stretching region. The data were extracted from fits neglecting the band splitting at very low temperatures, i.e., only one band was fitted under each position. This is reasonable because the splitting occurs symmetrically and has no significant effect on the bandwidth. The data are listed in Table 5.1. The 1σ-uncertainty of the band position and the FWHM is about ± 1.5 cm^{-1}. Figure 2a and b show the behavior of peak position and FWHM of ν_1 and ν_2, respectively, as a function of temperature. The OH-concentration c for each particular OH-band was calculated using the Lambert–Beer-law $c = A/(3 \cdot \epsilon \cdot t)$, where A is the measured absorbance from the particular band in the IR spectrum, ϵ the molar absorption coefficient for water in minerals from Libowitzky and Rossman (1997) and t the film thickness. Taking the spectrum at 30°C as an example, ν_1 represents about 40% and ν_2 about 60% of the total OH-concentration. This implies that the sites are non-equally occupied, which is in agreement with neutron powder diffraction data of topaz-OD at room temperature (Komatsu et al. 2008). In case of the splitted bands at –196°C a further evaluation of the absolute intensities of ν_1 and ν_2, respectively, allowed the following assignment: 55% to ν_{1a} and 45% to ν_{1b}, as well as 64% to ν_{2a} and 36% to ν_{2b}.

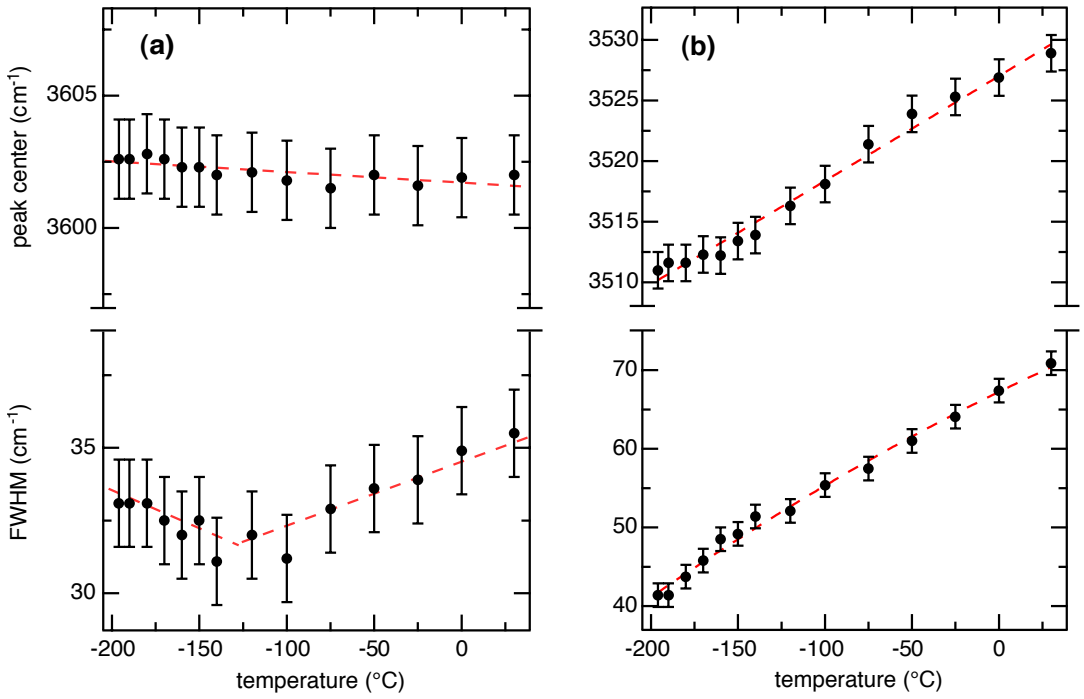

Figure 5.2: Temperature dependence of the peak position and the FWHM of the OH-stretching bands **(a)** ν_1 and **(b)** ν_2. Data were obtained by fitting only one band at each position (see text for further explanations). Dashed lines are derived from linear fits of the data points and illustrate changes in the slopes.

5.4.3 Autocorrelation analysis

The results from the autocorrelation analysis of the temperature-dependent IR spectra are shown in Fig. 5.3. The variation of ΔCorr as a function of temperature reveals two steps in the slope, one at about –155°C and another at about 380°C, which can be interpreted as indications of phase transitions. The transition temperature at 380°C is determined by the intersection of two linear fits, but due to the large temperature interval between two adjacent points in Fig. 5.3, only an approximate value is obtained. The 1σ-uncertainties of ΔCorr are below 1%. The main source of errors in the autocorrelation analysis is the sample preparation. All IR measurements of this study were carried out on the same sample film. A systematic error due to the sample preparation is hence negligible. The uncertainty of ΔCorr comes from the autocorrelation itself.

Table 5.1. Band positions and FWHMs of the OH-stretching bands ν_1 and ν_2 at low temperatures.

T (°C)	band center ν_1 (cm^{-1})	FWHM ν_1 (cm^{-1})	band center ν_2 (cm^{-1})	FWHM ν_2 (cm^{-1})	r^2
30	3602.0	35.5	3528.9	70.9	0.9957
0	3601.9	34.9	3526.9	67.4	0.9931
–25	3601.6	33.9	3525.3	64.1	0.9942
–50	3602.0	33.6	3523.9	61.0	0.9938
–75	3601.5	32.9	3521.4	57.5	0.9949
–100	3601.8	31.2	3518.1	55.4	0.9926
–120	3602.1	32.0	3516.3	52.1	0.9942
–140	3602.0	31.1	3513.9	51.4	0.9911
–150	3602.3	32.5	3513.4	49.2	0.9910
–160	3602.3	32.0	3512.2	48.5	0.9895
–170	3602.6	32.5	3512.3	45.8	0.9881
–180	3602.8	33.1	3511.6	43.7	0.9876
–190	3602.6	33.1	3511.6	41.4	0.9807
–196	3602.6	33.1	3511.0	41.4	0.9831

1σ-uncertainty of band position and FWHM: 1.5 cm^{-1}
r^2: agreement factors from peak fitting

5.5 Discussion

5.5.1 IR spectroscopy

We discuss our experimental results in the light of the predictions derived from ab inito quantum-mechanical calculations (Churakov and Wunder 2004). Applying their notation, we assign the four OH-bands at low temperatures (Fig. 5.1b) to the following stretching modes, for reasons, which will become clear below: ν_{1a} to O4–H4, ν_{1b} to O4–H1, ν_{2a} to O4–H3 and ν_{2b} to O4–H2. The calculated atomic positions of hydrogen in the crystal structure proposed by Churakov and Wunder (2004) have been reconciled by Komatsu et al. (2008) with those obtained from X-ray and neutron diffraction data of topaz-OH(D) (Northrup et al. 1994; Chen et al. 2005; Komatsu et al. 2008). Accordingly, positions H3 and H4 of Churakov and Wunder's (2004) assignment correspond to H(D)1 and H(D)2 of the terminology of Komatsu et al. (2008).

Below –160 °C, the IR spectra of topaz-OH clearly show four different OH-bands in the spectral region of the OH-stretching vibrations (Fig. 5.1b), indicating four non-equivalent hydrogen positions. According to Churakov and Wunder's (2004) calculations, the distribution among these four sites is strongly temperature dependent. Their calculations at –218°C predict abandoned H1 and H2 positions, but indicate high proton concentrations in H3 and H4. Both positions, H3 and H4, are half occupied due to H–H repulsion. With increasing thermal energy, the proton mobility increases and more protons enter the H1 and H2 sites, which is in line with our low-temperature IR spectra (Fig. 5.1b).

From the results of the calculations, we consider H3 and H4 to be the most occupied positions at liquid nitrogen temperature. Our data for the OH-concentrations at this temperature showed higher concentration for ν_{1a} and ν_{2a}. Therefore, we assign ν_{1a} to the O4–H4

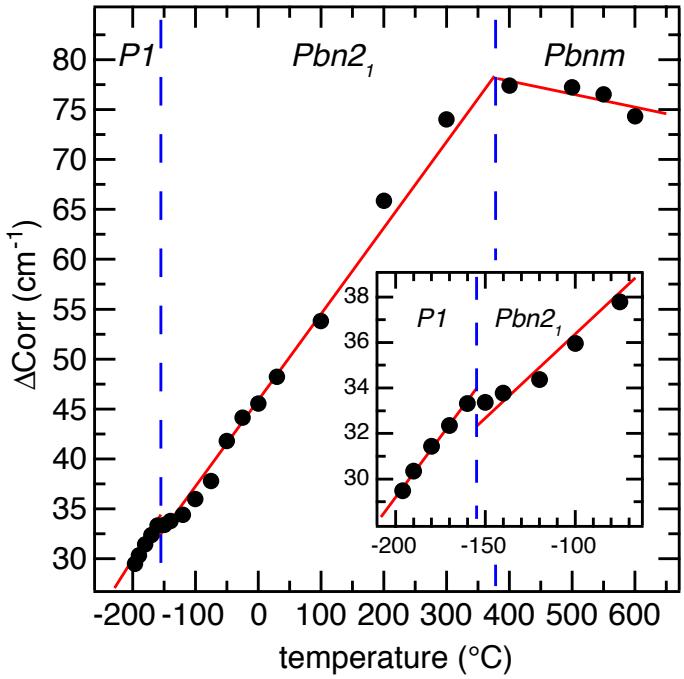

Figure 5.3: Variation of ΔCorr with temperature obtained from autocorrelation analysis of the IR spectra in the wavenumber range between 3,650 and 3,420 cm^{-1}. Vertical dashed lines indicate approximate transition temperatures of the *P1* ↔ *Pbn2*$_1$ ↔ *Pbnm* order–disorder phase transitions. Errors are within the size of the plotted data points.

and ν_{2a} to the O4–H3 mode. As H1 is closely adjacent to H4 and, accordingly, H2 to H3, ν_{1b} is assigned to O4–H1 and ν_{2b} to O4–H2 mode.

Approaching –160 °C from below results in enhanced occupation of H1 and H2 at the expense of H4 and H3, respectively (Fig. 5.1b). Accordingly, above –160 °C ν_{1a} and ν_{1b} merge into ν_1, and ν_{2a} and ν_{2b} into ν_2. Following Churakov and Wunder (2004), ν_1 and ν_2 display the superposition of the four bands, because increasing thermal energy allows the protons to switch between the closely adjacent positions. The two positions at room temperature, H(D)1 and H(D)2 after Komatsu et al. (2008), are in turn the superposed positions of H3, H2 and H4, H1, respectively. The small difference between these positions is yet unresolvable by crystal structure analysis. At higher temperatures, the protons switch easily among the four sites, which connote that they are completely disordered. Accordingly, above 400°C the OH-bands ν_1 and ν_2 merge into one superposed band ν_{OH} (Fig. 5.1a). One can speculate that high-temperature X-ray diffraction possibly detects only one proton position.

Generally, in case of linear or nearly linear hydrogen bonds, the OH-bands shift toward higher wavenumbers with increasing temperature due to extended O–H$\cdots$O distances. Furthermore, the bands broaden with increasing thermal energy as a result of the enhanced oscillation amplitudes of the OH-vibrations. Principally, the OH-band ν_2 follows these common rules (Fig. 5.2b), though we find that the band's shift and the increase of the FWHM is

nonlinear, but of a second-order polynomial. In contrast to that, the temperature-dependent behavior of the band position and the bandwidth of ν_1 (Fig. 5.2a) is quite surprising: (1) The position of ν_1 does not change within the error (Fig. 5.2a), and (2) the FWHM of ν_1 shows a pronounced discontinuity, which is characterized by a minimum of the FWHM at about –140°C (Fig. 5.2a). One possible explanation of this behavior, another is given in the following section, is a temperature-induced crossover of the two bands underneath ν_1. Crossover means that two bands interchange their positions due to changing conditions (temperature, pressure, $\cdots$) in a way that their paths cross each other. However, such a crossover implies that ν_{1a} is the low-wavenumber band underneath ν_1 at room temperature and that the corresponding O4–H4$\cdots$O4 bond weakens, i.e., with decreasing temperature the O4–H4$\cdots$O4 distance increases, O4–H4$\cdots$O4 strongly bends or O4–H4 forms bonds with further acceptor oxygens.

The effect that decreasing temperature or increasing pressure on crystal structures has is often comparable, because both generally result in volume contraction and therefore shortening of the interatomic distances. Komatsu et al. (2008) investigated the effect of pressure up to 7.5 GPa on the crystal structure of topaz-OD by neutron powder diffraction. With increasing pressure, each of the O–D$\cdots$O distances (following notation after Komatsu et al. 2008) decreased. However, as a result of extremely decreasing O–D–O angles the distances D1$\cdots$O2 and D2$\cdots$O1 increase with increasing pressure. As a consequence, the donor–acceptor interaction strengthens for O4–D1$\cdots$O3, O4–D2$\cdots$O2 and O4–D2$\cdots$O4 and weakens for O4–D1$\cdots$O2 and O4–D2$\cdots$O1 with increasing pressure. From these results, indeed, O4–D2$\cdots$O1, corresponding to O4–H1$\cdots$O1 of Churakov and Wunder (2004), is a possible candidate for the OH-band shift toward higher wavenumbers with decreasing temperature. This hypothesis partly contradicts the results of Churakov and Wunder (2004) in that H1 and not H4 represents ν_{1a} at –196°C. For verification, low-temperature crystal structure analyses on topaz-OD, using neutron diffraction, are strongly needed. However, these measurements go beyond the scope of this study.

Komatsu et al. (2005) determined Raman spectra of topaz-OH in the range of the OH-bands between ambient conditions and 17.3 GPa. With increasing pressure, neither an indication of band splitting nor any unusual discontinuity in the band shift was observed. Hypothetically, in analogy to the low-temperature IR spectra, a band splitting might occur at pressures above 17.3 GPa. Yet, we suggest that the thermally induced hydrogen order–disorder is mainly responsible for the observed band splitting and not the shortening of the interatomic distances due to volume contraction, which is simulated by the applied pressure. This is indicated by simultaneous splitting of ν_1 and ν_2 at the same temperature of about –160°C. A change of O–H$\cdots$O distances with temperature or pressure is known to be strongly anisotropic (Fei 1995) and hence would induce individual band splitting at different temperatures or pressure.

5.5.2 Autocorrelation analysis

Changes in the line width of IR and Raman spectra can conveniently characterize dynamic order–disorder phase transitions. Therefore, reliable FWHM, extracted from spectroscopic data, are required. Low-temperature IR spectra of topaz-OH show four different OH-bands, which overlap with increasing temperature. Manual fitting each single band to determine its

line width is difficult and imprecise over the whole temperature range. Fitting two superior bands, ν_1 and ν_2, works at low temperatures (Table 5.1, Fig. 5.2). However, band shifting and broadening as well as merging into one asymmetric broad band above 400°C affect accurate band fitting for the high-temperature spectra. In contrast to conventional peak fitting, the autocorrelation method characterizes bandwidths in phonon spectra with even complex band shape (Salje et al. 2000) and therefore is used here to examine the FWHM changes.

Steps in the slope of ΔCorr reveal possible phase transitions at about –155°C and 380°C (Fig. 5.3), respectively. A step in the FWHM of ν_1 and ν_2 at low temperature is also observed for the manually fitted data (Fig. 5.2). Because of the above described difficulties with the band fitting, the determined transition temperature, –140°C, is much less accurate. We suggest changes in symmetry from space group *P1* to $Pbn2_1$ for the low-temperature and from $Pbn2_1$ to *Pbnm* for the high-temperature transition. The low-temperature transition is a static–dynamic transition, whereas the high-temperature transition is caused by disordering of the protons.

Several observations from other studies support our proposed phase transitions, hence the limitations of the methods has to be kept in mind for the interpretation of the results. Diffraction studies are sensitive to long-range order and give crystal structure properties averaged over many unit cells. In contrast, spectroscopic studies focus on short-range order and give informations on the local structure and the crystal chemical properties.

Churakov and Wunder (2004) argued that at low temperature, ordered proton configurations of four non-equivalent H-positions exist and that the protons are almost fixed in their positions due to restricted proton movement. These configurations, essentially observable in the IR spectrum at –196°C, violate all symmetry elements of *Pbnm* and hence have to be assigned to *P1*. Northrup et al. (1994) found two structurally different H-sites by single-crystal XRD on topaz-OH at room temperature. As a result of ordering of the H-atoms, they suggested a symmetry reduction from the centrosymmetic space group *Pbnm* to non-centrosymmtric $Pbn2_1$ due to loss of the mirror plane (001). This assumption was verified by second harmonic generation measurements, which indicated a lack of a center of symmetry (Northrup et al. 1994). Calculations of the proton density distribution at 392°C (Churakov and Wunder 2004) clearly indicate the existence of the mirror plane (001) and thus point to space group *Pbnm* at such high temperature.

Even though there are a number of arguments for two temperature-dependent phase transitions, no indication of symmetry reduction of space group *Pbnm* was ever observed for topaz-OH from crystal structure refinements (Northrup et al. 1994; Chen et al. 2005; Komatsu et al. 2008). This is not surprising, because X-ray or neutron diffraction techniques, especially at room or higher temperatures, give always only informations on long-range order. We, however, assume that the temperature-induced order–disorder phase transitions in topaz-OH only involve the positions of the H-atoms and that the lattice framework itself remains almost static apart from temperature-dependent volume changes. The detection of H-positions is quite challenging, and in case of topaz-OH even more demanding, because the proton positions are closely adjacent and disordered. A temperature-dependent neutron diffraction study on topaz-OD might be able to resolve the four averaged positions and confirm space group *P1* at low temperatures.

5.6 Conclusion

The IR spectra at temperatures below –160°C prove the existence of four non-equivalent H-positions in topaz-OH, which were first predicted by Churakov and Wunder (2004) from ab initio quantum mechanical calculations.

Increasing temperature enhances proton movement in the structure and consequently switching between the closely adjacent positions, H4 and H1 as well as H3 and H2. Around room temperature one can only distinguish between two superposed positions corresponding to two broad OH-bands in the IR spectra. Above 400°C the protons are in complete dynamic exchange between the four positions, which is in line with only one asymmetric broad band in the IR spectra.

The temperature-dependent change of the OH-band shapes is caused by a thermally induced hydrogen order–disorder in the structure, whereas the lattice framework remains almost static. The autocorrelation analysis of the IR spectra in the region of the OH-stretching frequencies revealed two order-disorder phase transitions with regard to the H-atoms. At about –155°C the space group changes from *P1* to $Pbn2_1$ and at about 380°C from $Pbn2_1$ to *Pbnm*. The phase transitions are caused by temperature and dynamic average as temperature induces proton movement and an increasingly more symmetric proton density distribution.

Acknowledgments We thank M. Koch-Müller for the help with the film preparation in the DAC and helpful comments, M. Gottschalk for the help with the program for the autocorrelation analysis and W. Heinrich and E. Libowitzky for fruitful discussions. The reviews by Sergey Churakov and an anonymous reviewer helped to improve the manuscript and are highly appreciated. We thank M. Rieder for the effective editorial handling of the manuscript. This work was supported by the German Science Foundation (He 2015/(8-1)) to W. Heinrich within the framework of the Priority Program 1236 "Structures and properties of crystals at extreme pressures and temperatures", which is gratefully acknowledged.

5.7 References

Abbott RN Jr (1990) Topaz: energy calculations bearing on the location of hydrogen. Can Mineral 28:827–833

Barton MD (1982) The thermodynamic properties of topaz solid solution and some petrological applications. Am Mineral 67:956–974

Chen J, Lager GA, Kunz M et al (2005) A Rietveld refinement using neutron powder diffraction data of a fully deuterated topaz, $Al_2SiO_4(OD)_2$. Acta Crystallogr E. doi:10.1107/S1600536805034811

Churakov SV, Wunder B (2004) Ab initio calculations of the proton location in topaz-OH, $Al_2SiO_4(OH)_2$. Phys Chem Miner 31:131–141. doi:10.1007/s00269-003-0365-8

Domanik KJ, Holloway JR (1996) The stability and composition of phengitic muscovite and associated phases from 5.5 to 11 GPa: implications for deeply subducted sediments. Geochim Cosmochim Ac 60(21):4133–415. doi:10.1016/S0016-7037(96)00241-4

Fei Y (1995) Thermal expansion. In: Mineral physics and crystallography – a handbook of physical constants. AGU Reference Shelf 2:29–43

Griffiths PR, de Haseth JA (1986) Fourier transform infrared spectroscopy. Wiley, New York

Komatsu K, Kagi H, Okada T et al (2005) Pressure dependence of the OH-stretching mode in F-rich natural topaz and topaz-OH. Am Mineral 90:266–270. doi:10.2138/am.2005.1652

Komatsu K, Kagi H, Marshall WG et al (2008) Pressure dependence of the hydrogen-bond geometry in topaz-OD from neutron powder diffraction. Am Mineral 93:217–227. doi:10.2138/am.2008.2483

Larson AC, von Dreele RB (2004) Generalized structure analysis system. Los Alamos Nat Lab Rep LAUR, 96–748

Libowitzky E, Beran A (2004) IR spectroscopic characterisation of hydrous species in minerals. In: Beran A, Libowitzky E (eds) Spectroscopic methods in mineralogy, EMU notes in mineralogy, vol 6, pp 227–279

Libowitzky E, Rossman GR (1997) IR absorption calibration for water in minerals. Am Mineral 82:1111–1115

Mertz L (1965) Transformation in optics. Wiley, New York

Northrup PA, Leinenweber K, Parise JB (1994) The location of H in the high-pressure synthetic $Al_2SiO_4(OH)_2$ topaz analogue. Am Mineral 79:401–404

Ono S (1998) Stability limits of hydrous minerals in sediment and mid-ocean ridge basalt compositions: implications for water transport in subduction zones. J Geophys Res 103(B8):18253–18267. doi:10.1029/98JB01351

Ono S (1999) High temperature stability limit of phase egg, $AlSiO_3(OH)$. Contrib Mineral Petr 137:83–89. doi:10.1007/s004100050583

Ribbe PH (1982) Topaz. In: Ribbe PH (ed) Orthosilicates. Reviews in Mineralogy, 2rd edn, pp 215–230

Salje E, Carpenter MA, Malcherek, T et al (2000) Autocorrelation analysis of infrared spectra from minerals. Eur J Mineral 12:503–519

Schmidt MW (1995) Lawsonite: upper pressure stability and formation of higher density hydrous phases. Am Mineral 80:1286–1292

Schreyer W (1995) Ultradeep metamorphic rocks: the retrospective viewpoint. J Geophys Res 100(B5):8353–8366. doi:10.1029/94JB02912

Theye T (1988) Aufsteigende Hochdruckmetamorphose in Sedimenten der Phyllit-Quarzit-Einheit Kretas und des Peloponnes. Ph.D. Thesis, University of Braunschweig

Watenphul A, Wunder B, Heinrich W (2009) High-pressure ammonium-bearing silicates: implications for nitrogen and hydrogen storage in the Earth's mantle. Am Mineral 94:283–292. doi: 10.2138/am.2009.2995

Wunder B, Rubie DC, Ross II CD et al (1993) Synthesis, stability, and properties of $Al_2SiO_4(OH)_2$: a fully hydrated analogue of topaz. Am Mineral 78:285–297

Wunder B, Andrut M, Wirth R (1999) High-pressure synthesis and properties of OH-rich topaz. Eur. J. Mineral 11:803–813

Xue X, Kanzaki M, Fukui H et al (2006) Cation order and hydrogen bonding of high-pressure phases in the $Al_3O_3 - SiO_2 - H_2O$ system: an NMR and Raman study. Am Mineral 91:850-861. doi:10.2138/ am.2006.2064

Zhang RY, Liou JG, Shu JF (2002) Hydroxyl-rich topaz in high-pressure and ultrahigh-pressure kyanite quartzites, with retrograde woodhousite, from the Sulu terrane, eastern China. Am Mineral 87:445–453

Chapter 6

This chapter is submitted as

"The OH site in topaz: an IR spectroscopic investigation"

by

Anke Watenphul, Eugen Libowitzky, Bernd Wunder, and Matthias Gottschalk.

to

Physics and Chemistry of Minerals.

The OH site in topaz: an IR spectroscopic investigation

Anke Watenphul[1]*, Eugen Libowitzky[2], Bernd Wunder[1], and Matthias Gottschalk[1]

[1] Deutsches GeoForschungsZentrum (GFZ), Telegrafenberg, 14473 Potsdam, Germany, Section 3.3

[2] Institut für Mineralogie und Kristallographie, Universität Wien – Geozentrum, Althanstraße 14, A-1090 Wien, Austria

* email: watenphul@gfz-potsdam.de

Abstract

The OH site in topaz is investigated by IR spectroscopy in dependence of the OH concentration and temperature. Two OH bands can be differentiated and are due to the local ordering of F and OH in neighboring sites of the crystal structure. The first typical sharp band stems from OH groups with fluorine in the neighboring site. The second band occurs as a shoulder on the low-energy wing and is related to two neighboring OH groups. The degree of local OH–OH ordering depends on the OH concentration and, due to statistical F/OH distribution, can be predicted by probability calculations. The substitution of OH for F has a non-linear effect on the increase of the lattice parameters. An autocorrelation analysis of the IR spectra revealed two temperature-induced phase transitions. At -135°C, the space group changes from *P1* to $Pbn2_1$, although this change involves only the H atoms. The transition from $Pbn2_1$ to *Pbnm* at about 160°C is caused by changes of the local F/OH ordering in the crystal structure.

Keywords Topaz · IR spectroscopy · hydrogen bond geometry · autocorrelation analysis

6.2 Introduction

Natural topaz, $Al_2SiO_4(F,OH)_2$, is most commonly found in igneous rocks such as pegmatites, granites, and rhyolites. It occurs in near-surface environments (e.g., Ribbe 1982; Barton 1982), but was also found in low-temperature, high- to ultrahigh-pressure metamorphic rocks (Theye 1988; Xu 1994; Zhang et al. 2002). The OH content in topaz of near-surface environments most often does not exceed $X_{OH} = 0.3$ [$X_{OH} = OH/(OH + F)$], which led to the "proton–proton avoidance"-theory implying a X_{OH} limit of 0.5 (Barton 1982). However, recent topaz-findings in ultrahigh-pressure rocks of the Sulu terrane, Eastern China (Zhang et al. 2002) with $X_{OH} = 0.55$, as well as experimental high-pressure studies indicated that topaz might be stable along the complete (OH,F) solid solution series depending on the P–T–X conditions (Wunder et al. 1993; 1999). Increasing pressure has an increasing effect on the OH content. Therefore, it is not unexpectedly that the fully hydrated end member $Al_2SiO_4(OH)_2$, topaz-OH, was shown to be a high-pressure and high-temperature phase, albeit it is only known from experimental studies, yet (Wunder et al. 1993; Schmidt 1995; Ono 1999). The incorporation of up to 10.7 wt% H_2O (OH end member) makes topaz an important hydrous phase in subducted pelitic sediments and basaltic rocks (Schreyer 1995; Schmidt 1995; Domanik and Holloway 1996; Ono 1998).

The crystal structure of topaz consists of isolated $[SiO_4]^{4-}$ tetrahedra, which connect chains of edge-sharing $[AlO_4(F,OH)_2]^{7-}$ octahedra. The OH group resides in a cavity aligned within the (010) plane and is inclined about $\sim 35°$ from the c axis (Gebert and Zemann 1965; Shinoda and Aikawa 1997; Libowitzky and Beran 2006). Topaz has the orthorhombic space group *Pbnm*, in which F and OH are statistically distributed on the same crystallographic site (e.g., Zemann et al. 1979). The substitution of the slightly larger hydroxyl anion (ionic radii after Wells 1984: $F^- = 1.33$ Å, $(OH)^- = 1.37$ Å) effects structural and optical parameters, so that several linear correlations between the fluorine content and the parameters a, b, V, and the optical axial angle $2V_\gamma$ were established (Ribbe and Rosenberg 1971; Wunder et al. 1999; Alberico et al. 2003). The high confidence with up to $r^2 = 0.982$ allows quite precise predictions of the fluorine, and thus the OH content.

IR spectra of topaz, except of both end members, display one sharp absorption band around 3650 cm^{-1} along with a shoulder on the low-energy side (e.g., Beny and Piriou 1987; Wunder et al. 1999; Pinheiro et al. 2002; Komatsu et al. 2005). The sharp absorption band is attributed to the stretching mode of the hydroxyl in the crystal structure (e.g., Aines and Rossman 1985). Up to now, the nature of the shoulder was still unknown. It was attributed to different hydroxyl sites within the crystal structure (Pinheiro et al. 2002), a coupled substitution of cations with the OH group or other local distortions (Wunder et al. 1999). In addition to the stretching bands, Shinoda and Aikawa (1997) observed the OH bending mode at 1165 cm^{-1} and a harmonic combination mode at 4803 cm^{-1}.

Pressure-dependent IR studies up to 30.4 GPa determined a small frequency increase of the main OH band with pressure, which indicates that the weak hydrogen bonding does not significantly strengthen with compression (Bradbury and Williams 2003; Komatsu et al. 2005). In-situ single-crystal XRD studies up to 10.55 GPa found no phase transitions in that pressure range (Komatsu et al. 2003; Gatta et al. 2006a). The effect of pressure is mostly accommodated by the $AlO_4(F,OH)_2$ octahedra and the voids in the crystal structure. The bond distances decrease anisotropically with pressure, which causes a distortion of

the octahedra. Topaz shows a significant anisotropy in it's thermal expansion (e.g., Fei 1995), which is related to differences in the increase of Al–O and Al–(F,OH) bonds of the $AlO_4(F,OH)_2$ octahedra with temperature (Komatsu et al. 2003).

The aim of the present study is to clarify the OH bonding geometry in topaz in dependence of the OH content and temperature. Natural and synthetic topaz samples with varying OH contents are studied by unpolarized and polarized IR spectroscopy over a broad temperature range. It is shown that the statistical distribution of F and OH in the crystal structure has a major influence on the OH bonding behavior and thus, requires the existence of two OH stretching bands. A precise autocorrelation analysis of the OH stretching region of IR spectra reveals temperature- and X_{OH}-dependent structural changes.

6.3 Sample description and analytical methods

6.3.1 Sample description

Natural and synthetic topaz samples with OH contents of X_{OH} between 0.075 and 0.82 were investigated in this study (Table 6.1). The 17 synthetic samples have been previously described in Wunder et al. (1999) and are termed here with the same labels. Starting materials, run conditions, and phase proportions of the run products are listed in the previous work. The investigated IR samples are KBr pellets consisting of 1 mg finely ground sample material homogenized with 450 mg KBr. Two natural topaz samples were also investigated. The topaz sample from Ouro Preto, Minas Gerais, Brazil has been described in Wirth and Wunder (2000) as sample Top16 with an OH concentration of $X_{OH} = 0.23$. A clear, colorless, gem-quality topaz crystal from Spitzkopje, Namibia was previously described in Libowitzky and Beran (2006), and is labeled here Top-E. The reported OH concentration is $X_{OH} = 0.075$.

6.3.2 Sample preparation and IR spectroscopy

The KBr pellets of the synthetic samples and an equally prepared KBr pellet of Top-E were pre-dried at 170°C for one week before reinvestigation. Measurements were carried out with a Bruker IFS 66v FTIR spectrometer equipped with a Globar lightsource, a KBr beamsplitter and a DTGS detector at the GFZ Potsdam. The sample chamber was evacuated to 200 Pa, so that influences of atmospheric H_2O and CO_2 were negligible. The measurements were carried out between 4000 and 400 cm^{-1} with a resolution of 1 cm^{-1}. The measured spectra were averaged over 256 scans.

The temperature dependence was investigated between -196 and 600°C on a thin film of the natural sample Top16. A detailed description of the film preparation is given in Watenphul and Wunder (2009). The film thickness was determined to 3 ± 0.5 μm by measurements on video images using the program *OPUS* by Bruker.

The film was then mounted on a glass carrier and placed in a Linkam FTIR600 heating/freezing stage under a Hyperion microscope attached to the FTIR spectrometer. Spectra were taken with an aperture of 40 μm $\times$40 μm, intensities were recorded with a MCT detector. Measurements were carried out in the spectral range from 4000 to 3000 cm^{-1} with a resolution of 1 cm^{-1}. The spectra were averaged from 256 scans.

Table 6.1 Investigated samples, OH concentration, and sample preparation method

Sample	Origin	X_{OH}	Sample preparation
Top-E	Spitzkopje, Namibia	0.075[b]	KBr pellet (unpol. IR), single-crystal plates (pol. IR)
415/1	synthetic	0.22[a]	KBr pellet
Top16	Minas Gerais, Brazil	0.23[a]	thin film
427/1	synthetic	0.27[a]	KBr pellet
427/2	synthetic	0.28[a]	KBr pellet
427/3	synthetic	0.29[a]	KBr pellet
426/1	synthetic	0.29[a]	KBr pellet
426/2	synthetic	0.32[a]	KBr pellet
426/3	synthetic	0.33[a]	KBr pellet
427/4	synthetic	0.34[a]	KBr pellet
426/4	synthetic	0.35[a]	KBr pellet
423/1	synthetic	0.40[a]	KBr pellet
423/2	synthetic	0.43[a]	KBr pellet
419/1	synthetic	0.46[a]	KBr pellet
420/1	synthetic	0.48[a]	KBr pellet
420/2	synthetic	0.51[a]	KBr pellet
424/2	synthetic	0.58[a]	KBr pellet
422/2	synthetic	0.67[a]	KBr pellet
422/1	synthetic	0.82[a]	KBr pellet

[a] X_{OH} determined from the unit cell volume V (Wunder et al. 1999)
[a] X_{OH} determined from the lattice parameter b (Ribbe and Rosenberg 1971)

Polarized IR spectra were recorded from the sample Top-E. The crystal was oriented according to the excellent cleavage parallel to (001) and along the optical extinction directions. Three platelets (100), (010), and (001) were cut, attached with epoxy resin to a glass sample holder and then diamond-polished to a final thickness of about 15 μm. The IR spectra were taken at the University of Vienna with a Bruker Tensor27 FTIR spectrometer and a Hyperion microscope in the spectral range from 4000 to 2500 cm^{-1} with a resolution of 1 cm^{-1} using a Globar light source, a KBr beamsplitter and a MCT detector. Measurements were carried out without removing the polished crystal thin section from the glass plate therefore, the spectra were corrected for background absorption from glass and epoxy resin.

For temperature-dependent measurements a Linkam FTIR600 heating/freezing stage under the Hyperion microscope was used. The spectra were averaged from 128 scans. All spectra were background-corrected and afterwards the band center and the full width at half band maximum (FWHM) of each band were determined using the program *PeakFit* by Jandel Scientific.

6.3.3 Autocorrelation analysis

The autocorrelation method has been proven useful to investigate changes of the bandwidth if the bands' shape is of complex nature (Salje et al. 2000). The shoulder at the low-energy side of the OH stretching band of topaz is not well resolved and, therefore, it is difficult

to obtain the band position and the full width at half maximum (FWHM) unambiguously and with low estimated standard deviation with conventional peak fitting methods. The spectral region 3570 to 3680 cm^{-1} has been selected as the appropriate segment of the concentration-dependent and the unpolarized temperature-dependent IR spectra, the region from 3630 to 3670 cm^{-1} as the best segment of the polarized temperature-dependent spectra. A suitable linear baseline between the end points was subtracted from each spectral segment. This baseline-corrected subspectrum $\alpha(\omega)$ is correlated with itself using the autocorrelation function

$$Corr(\alpha, \omega') = \int \alpha(\omega + \omega')\alpha(\omega)d\omega \tag{6.1}$$

reported by Salje et al. (2000) to produce an autocorrelation spectrum. The width of the central peak of each autocorrelation spectrum at $\omega' = 0$ varies with the general width of the overlapping peaks in the primary IR spectrum, thus the autocorrelation spectrum contains the combined information of the line widths of the overlapping sequence of peaks. Extrapolation of the width of the central peak in the limit $\omega' \rightarrow 0$ yields the quantitative information on the primary line widths. Therefore, a Gaussian curve is fitted to the central peak around the offset $\omega' = 0$ for successive ranges of ω'. ΔCorr, a variable proportional to the FWHM of the Gaussian curve at $\omega' = 0$, is obtained by extrapolation using a polynomial function.

6.4 Results

6.4.1 OH concentration dependence

Room temperature IR spectra of the samples in the region of the OH stretching frequency are shown in Fig. 6.1. IR spectra of the samples 426/1 (identical X_{OH} as 427/1; Table 6.1) and 415/1 (low topaz content, see below) are excluded. All spectra have been scaled, so that the maximum absorbance equals one, because of the varying amounts of the synthetic topaz in the run products. Each spectrum displays one sharp absorption band along with a shoulder on the low-energy side, which is variously pronounced depending on the OH concentration. Following the notation of Pinheiro et al. (2002), the sharp band is termed ν_B and the shoulder ν_A. The bands at 3667 and 3675 cm^{-1} in the topaz spectra with $X_{OH} = 0.67$ and 0.81 have been described in Wunder et al. (1999) and belong to an additional, unknown OH-bearing phase. The amount of this phase in the run products was too small for quantification, and therefore, it will not be considered further in this study.

The band center of ν_B shifts with increasing OH content up to $X_{OH} = 0.51$ to lower wavenumbers. At higher OH contents the band center relocates to higher wavenumbers. ν_A shows a similar behavior except that the backshift is less pronounced. These behaviors have also been observed by Wunder et al. (1999). The intensity and FWHM of ν_A increase significantly with increasing OH content.

Changes in the total bandwidth of both underlying components are analyzed by autocorrelation analysis. The variation of ΔCorr as a function of the OH concentration displays a continuous change of the slope (Fig. 6.2), which can be described by a Gaussian function.

The analytical uncertainties in ΔCorr from the autocorrelation analysis itself are below 1%. The main source of error in the determined bandwidths is caused by the sample

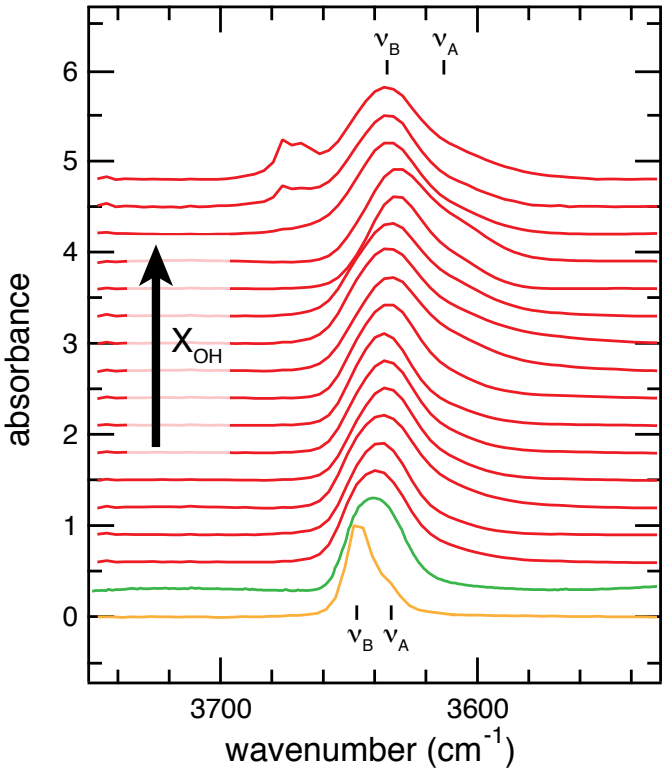

Figure 6.1: IR spectra of all topaz samples (except of samples 426/1, 415/1; see text) in the spectral region of the OH stretching vibration. Absorbances are standardized to $A_{max} = 1$; spectra are equidistantly offset for clarity. All red spectra are taken from the synthetic topaz samples from Wunder et al. (1999), the green spectrum is taken from Top16 (Wunder and Wirth 2000), the yellow spectrum stems from Top-E (Libowitzky and Beran 2006).

preparation (Salje et al. 2000). The preparation of the KBr pellets was carried out very carefully to avoid discrepancies, but the sample Top16 was prepared by a different method (thin film-pressing). Therefore, we assumed altogether an error of 5% for ΔCorr to cover any uncertainties due to differences in the sample preparation and the error of the autocorrelation analysis itself. The 2σ-uncertainty of the OH concentration is ± 0.02 as determined by the regression lines of Wunder et al. (1999) and Ribbe and Rosenberg (1971). The determined bandwidth (ΔCorr) of sample 415/1 with $X_{OH} = 0.22$ displays a significant variation from the fitted trend. This outlier might be due to the low topaz content in the run products (23 wt%) and thus in the KBr pellet. In contrast, the sample Top16 with a comparable OH concentration ($X_{OH} = 0.23$) fits well to the displayed data trend.

6.4.2 Temperature dependence

Fig. 6.3 shows selected IR spectra in the temperature range -196 to 600°C taken from the thin film of sample Top16 with $X_{OH} = 0.23$. The band centers of ν_A and ν_B shift concertedly to lower wavenumbers with increasing temperature, both bands broaden and

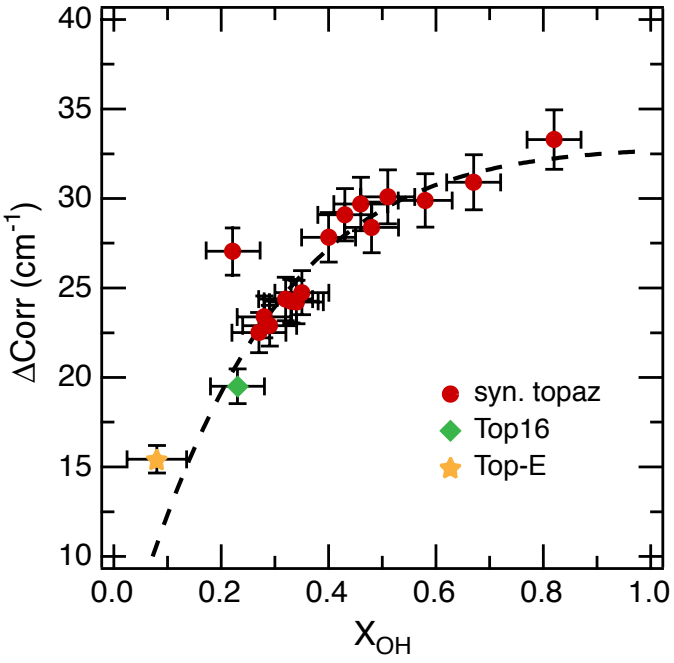

Figure 6.2: Variation of ΔCorr with X_{OH} calculated from the lattice parameters. Red circles mark the synthetic topaz samples from Wunder et al. (1999), the green diamond indexes sample Top16 (Wunder and Wirth 2000), the yellow star sample Top-E (Libowitzky and Beran 2006). The dashed black line is derived from fitting a gaussian curve to the data points and illustrates the change in the slope.

the absorbance decreases. Band position and FWHM are determined by "normal" peak fitting, which required a simplification to one superposed absorption band due to the small frequency difference between ν_A and ν_B. The shift of the band center as well as the variation of the FWHM displays a discontinuity at 150°C (Fig. 6.4). The evolution of the band position can be described by linear fits on both sides of the discontinuity, whereas the FWHM decreases linearly up to 150°C, but with higher temperatures the broadening shows a polynomial increase. The position of the band center is determined with an uncertainty of 1.5 cm^{-1}; the FWHM contains an error of 1 cm^{-1}. The variation of both bandwidths is further analyzed by autocorrelation analysis of the temperature-dependent spectra. The variation of ΔCorr with temperature displays two steps in the slope, one at about -150°C, the other at about 160°C (Fig. 6.5). Both discontinuities are determined by intersections of linear fits and hold a temperature uncertainty of ± 25°C, which is caused by the temperature steps between each two measured IR spectra.

Beside the dependence on OH concentration and temperature, the intensities of ν_A and ν_B vary also with polarization (insertion in Fig. 6.6). IR spectra of thin crystal plates from sample Top-E were taken in the temperature range -196 to 0°C with E ∥ X and E ∥ Z. An autocorrelation analysis of these temperature-dependent spectra shows a small variation between those two polarization directions (Fig. 6.6). However, the behavior of

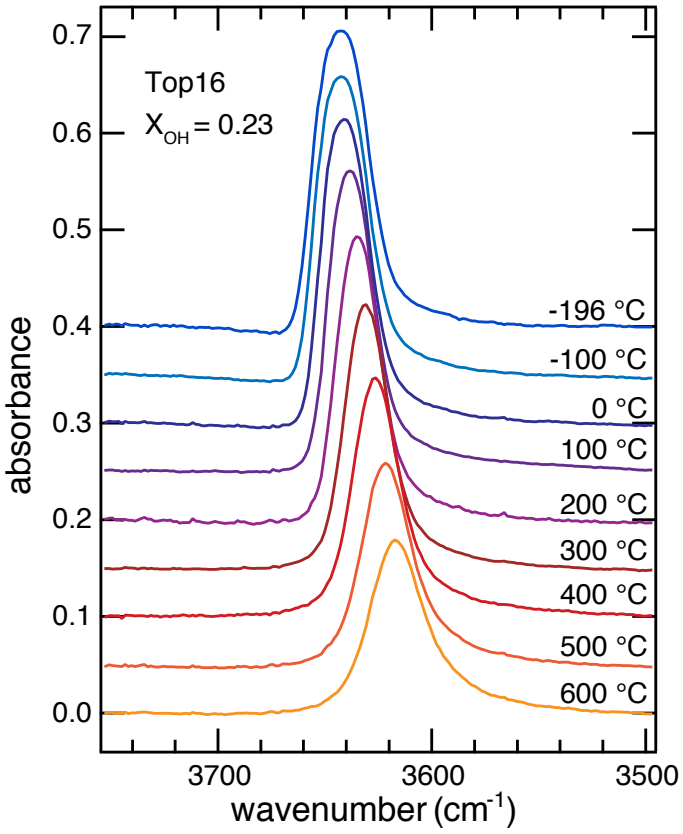

Figure 6.3: IR spectra of sample Top16 in the spectral region of the OH stretching vibration at selected temperatures between -196 and 600°C. Spectra are equidistantly offset for clarity.

ΔCorr with temperature determined from the polarized spectra is complementary to that observed from the unpolarized spectra (Fig. 6.5). In the polarized cases, ΔCorr increases in the investigated temperature range, whereas a decrease is observed in the unpolarized case shown in Fig. 6.5. The small temperature step of 10°C between two spectra allowed a better determination of the low-temperature discontinuity by the intersection of linear fits (Fig. 6.6). The step in the slope is visible at -135°C ± 5°C. The preparation of the thin crystal plates was carried out very carefully, so that differences can almost be excluded. Moreover, during the measurement very little contamination due to condensed water occurred. Therefore, 1σ-uncertainties of these analyses are estimated to 1.5%.

6.5 Discussion

6.5.1 Origin of the OH bands ν_A and ν_B

The crystal structure of topaz was first solved by Alston and West (1928) and Pauling (1928) and afterwards reinvestigated several times (e.g., Zemann et al. 1979; Aines and Rossman 1985; Alberico et al. 2003; Gatta et al. 2006a,b). In the orthorhombic space

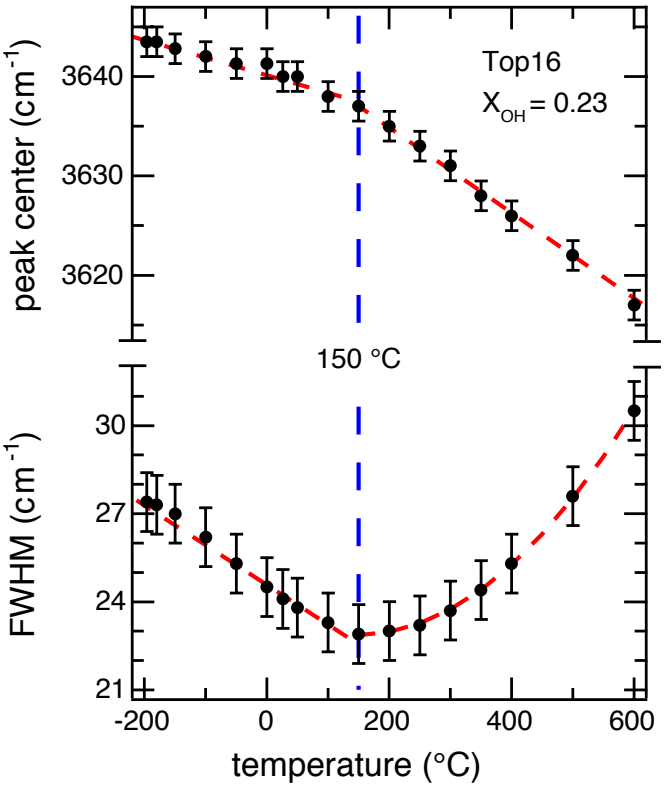

Figure 6.4: Temperature dependence of the peak position and the FWHM of the superposed OH stretching band (see text for further explanations). The dashed red lines are regression lines from linear or polynomial fitting and illustrate the changing slopes. The dashed blue line indicates the discontinuity temperature.

group *Pbnm*, F/OH occupy the same crystallographic site, i.e., a Wyckoff *8d* position. At low OH concentrations ($X_{OH} < 0.5$) the resulting, most probable F$\cdots$OH configuration will constitute in only one OH stretching band in the IR spectrum of topaz. In contrast, a few studies observed that the OH band consists of more than one component, however the origin was controversially discussed (e.g., Wunder et al. 1999; Pinheiro et al. 2002). All IR spectra of this study show these two components, ν_A and ν_B, of the OH stretching band. Most of the analyzed samples are of synthetic origin (Table 6.1), thus, impurities such as Cr^{3+} or Fe^{3+}, which substitute for Al^{3+} in the crystal structure, can be ruled out as the origin of ν_A. A coupled exchange of $Si^{4+} + O_2^- \Leftrightarrow Al^{3+} + F^-$ was reported by Rosenberg (1972). This might also occur for $(OH)^-$ instead of F^- and by this means result in a second OH stretching band. However, the EMP analyses of the synthetic topaz samples showed no significant deviation from the Al/Si ratio = 2 (Wunder et al. 1999). Therefore, it seems that ν_A is not related to such an exchange mechanism.

On the other hand, IR spectra are very sensitive to differences in the neighborhood of the investigated absorbing species and to differences in the hydrogen bond arrangement, such as differing H bond acceptors. Thus, we propose that a different local surrounding of the OH

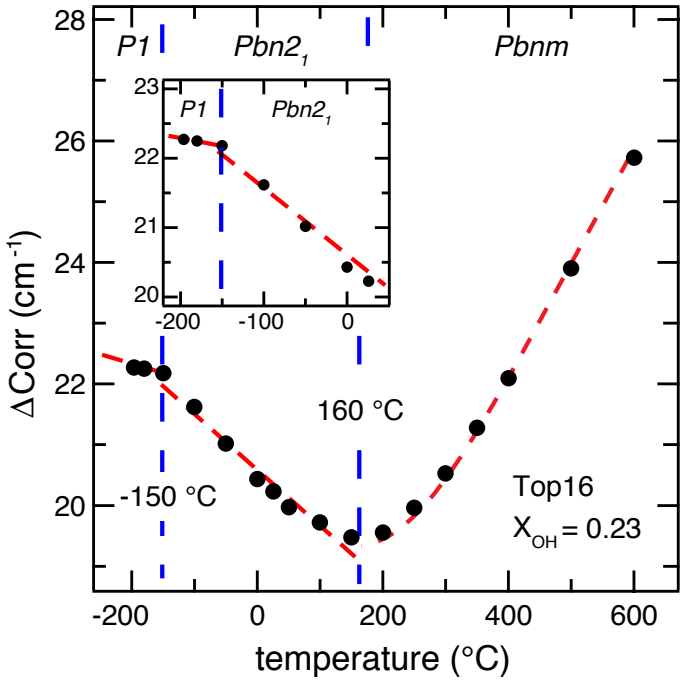

Figure 6.5: Variation of ΔCorr with temperature calculated from the temperature-dependent IR spectra of sample Top16. The dashed red lines represent linear fits, the vertical blue lines indicate the approximate discontinuity temperatures.

group is responsible for the occurrence of two bands in the IR spectra. The Al octahedra in the topaz structure build crankshaft-like chains, which are linked by oxygen atoms. The fluorine atom and the oxygen atom of the respective hydroxyl group are distributed on adjacent corner positions of an octahedron (Fig. 6.7). The occurrence of ν_A and ν_B depends on the occupying atom opposite to OH (roughly along the direction of the O–H vector) of the neighboring octahedron. Fig. 6.7 illustrates the three possible cases: (1) Both positions are occupied by fluorine atoms (Fig. 6.7, upper left part). As a matter of fact, this case is invisible in the OH stretching region of the IR spectrum. (2) One corner is occupied by a fluorine atom, the opposite by a hydroxyl group (Fig. 6.7, lower part). This is the most common situation in topaz with $X_{OH} < 0.66$ (almost all natural samples) and results in the occurrence of ν_B at higher wavenumbers in the IR spectrum. (3) Both opposite corners are occupied by hydroxyl groups (Fig. 6.7, lower part). Such a constellation causes a slight frequency shift of the resulting OH bands, so that the additional OH band ν_A is actually visible in the IR spectrum. In addition, the relaxation or disorder (positional or dynamic) of the two H atoms facing each other too closely (see also discussion below), causes a broadened band shape (FWHM) of the low-energy band ν_A.

The position of the OH$\cdots$F band (ν_B) at higher wavenumbers than the OH$\cdots$OH band (ν_A) is confirmed by the stretching frequency vs. bond distance correlation curves of Mikenda and Steinböck (1994), who studied the impact of various H bond acceptors such as fluorine and oxygen on the OH/OD stretching frequencies of hydrous solids in IR spectra.

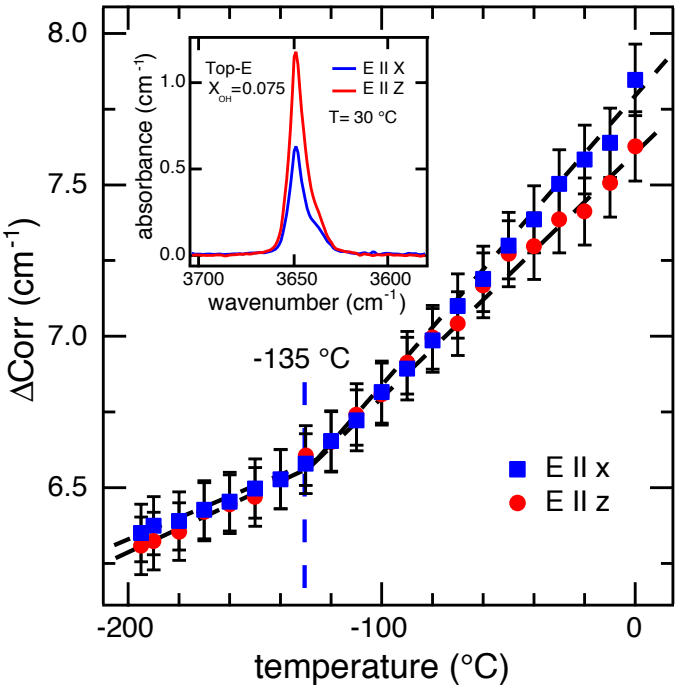

Figure 6.6: Variation of ΔCorr with temperature calculated from the temperature-dependent polarized IR spectra of sample Top-E. The insertion illustrates the dependence of the absorbance on polarization. The dashed lines represent linear fits, the vertical line indicates the approximate discontinuity in the slope.

Their studies showed convincingly that at constant H bond length the OH$\cdots$F bond resulted in up to 50 cm^{-1} higher wavenumbers than the OH$\cdots$O bond. This effect was reasonably well explained by the higher electronegativity of F and its smaller ionic radius (Mikenda and Steinböck 1996). The only slight distance between ν_A and ν_B in the topaz spectra (e.g. $\sim$ 25 cm^{-1} in Fig. 6.8) is related to the rather weak/long H bond, i.e., H$\cdots$O/F $\sim$ 2.38 Å, O$\cdots$O/F $\sim$ 3.20 Å (Libowitzky and Beran 2006, their Fig. 11), which attenuates the influence of the H bond acceptor.

According to Zemann et al. (1979), there is no F/OH ordering in the crystal structure and F/OH are statistically distributed on their shared position. If so, the occurrence and relative intensities of ν_A and ν_B depend only on the OH concentration and can be determined by probability calculations. The probability p for the occupation of two adjacent corners with two OH groups is given by $p(\mathrm{OH}\cdots\mathrm{OH}) = (\mathrm{X_{OH}})^2$. Thus, the probability for two adjacent F atoms can be calculated as $p(\mathrm{F}\cdots\mathrm{F}) = (1-\mathrm{X_{OH}})^2$, and $p(\mathrm{OH}\cdots\mathrm{F}) = 1-(\mathrm{X_{OH}})^2-(1-\mathrm{X_{OH}})^2$ for one fluorine atom close to one hydroxyl group. Fig. 6.1 shows that with increasing OH concentration the FWHM of ν_A increases (see above) more than its intensity. Moreover, the FWHM of OH stretching bands increases generally with increasing H bond strength and decreasing wavenumber and thus must be considered for calibration purposes (Libowitzky and Rossman 1997). Therefore, the integrated areas

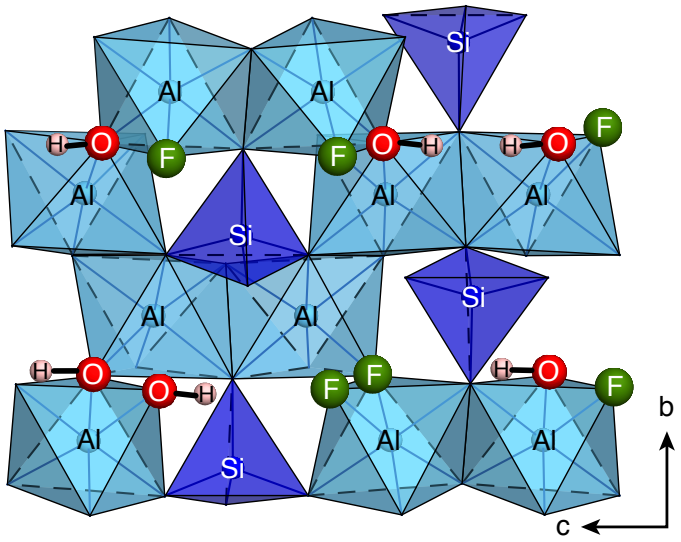

Figure 6.7: Crystal structure of topaz with highlighted F/O4 and H positions. All possibilities (OH···F, OH···OH, F···F) of neighboring corner occupation are illustrated with OH···F plotted as the most common case. Atomic positions from Gatta et al. (2006b).

of ν_A and ν_B are the appropriate variables to reflect the occupation probabilities. The determination of these integrated areas from an IR spectrum by peak fitting methods is illustrated in Fig. 6.8a. The maximum relative uncertainty of the determined sizes is 5% for ν_B and 10% for ν_A. Fitted and calculated probabilities of the OH environment are in excellent agreement and show almost no deviations (Fig. 6.8b). The integrated area of ν_A increases in favor of ν_B with increasing OH content, which means that the two neighboring F/OH positions are more often occupied by two OH groups. This accordance between calculated occupation probability and determined integrated areas proves that (i) the nature of ν_A and ν_B is only related to the local OH surrounding in the crystal structure, and (ii) the distribution of F and OH is actually statistical. Thus, ν_A is visible in every topaz IR spectrum because the band's origin and intensity are intimately related to the OH content itself.

6.5.2 X_{OH}-dependent changes of the crystal structure

Changes in the bandwidth of phonon spectra like IR or Raman spectra can conveniently characterize order–disorder phase transitions. The autocorrelation analysis gives reliable bandwidth data even for spectra with a complex bandshape, which may be caused by the overlap of multiple components (Salje et al. 2000). The determined value ΔCorr is proportional to the original bandwidth. Thus, discontinuities in the slope of ΔCorr reveal possible phase transitions. However, the variation of ΔCorr with increasing OH content displays a continuous slope change (Fig. 6.2) and no distinct transition, as it would be characteristic for a phase transition. This alternation of the bandwidth is interpreted as continuous change of the crystal structure with increasing X_{OH}, e.g., by an increasing ν_A band component with

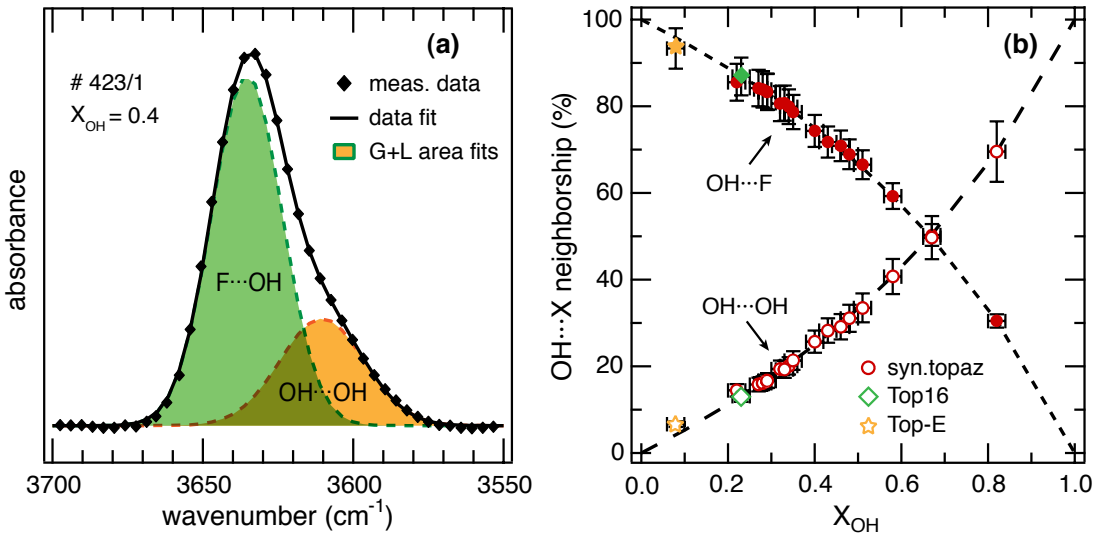

Figure 6.8: **(a)** Example of peak fitting of the OH bands of an unpolarized topaz room temperature IR spectrum used to derive the integrated areas of ν_A (OH$\cdots$OH) and ν_B (OH$\cdots$F). For $X_{OH} = 0.4$, probability calculations predict a ratio of 3:1 of ν_B : ν_A, which is reflected in the size of the integrated areas. **(b)** Integrated areas from peak fitting (symbols) and calculated percentage of the OH$\cdots$X neighborship from probability calculations (dashed black lines) versus the OH concentration in the topaz samples. Red circles: synthetic topaz from Wunder et al. (1999); green diamond: Top16 from Wunder and Wirth (2000); yellow star: Top-E from Libowitzky and Beran (2006).

broader FWHM (see above), and not a phase transition.

Topaz is mainly reported in space group *Pbnm*, independent of the OH concentration of the investigated topaz samples. No symmetry change associated with the OH content was ever observed. Ribbe and Rosenberg (1971) observed a linear correlation between the amount of OH substitution for F in the crystal structure and the lattice parameter b, which increases with increasing OH content. The reason for this increase is that the ionic radius of the OH group is about 0.04 Å larger than that of the fluorine atom. Thus, it is reasonable that structural increases were also observed for the lattice parameters a and V (Wunder et al. 1999, Alberico et al. 2003), but not for c. The O–H dipole has only a small deviation from the c axis and lies in a cavity, which compensates the structural increase. However, all these correlations are based on data sets of samples with $X_{OH} < 0.5$, which are extened to the data of the OH end member. The experimentally observed data for the synthetic topaz samples of Wunder et al. (1999), although having an uncertainty of 5% in the OH content, and the data of Zhang et al. (2002) show that above $X_{OH} \approx 0.4$ the lattice parameter c increases significantly with the OH content, too. In total, the substitution of OH for F has a non-linear effect on the crystal structure and, thus, on the bandwidths of the OH bands (Fig. 6.2). The incorporation of the larger OH group expands the lattice parameters a and b almost linearly over the whole concentration range, whereas in the c direction the effect is buffered by the cavity adjacent to the Al octahedra up to $X_{OH} \approx 0.4$ (Fig. 6.7).

Above $X_{OH} \approx 0.4$, in connection with the increase of the lattice parameter c, the increase of the entire crystal structure is non-linear. This non-linearity is quite small, so that the linear V-regression by Wunder et al. (1999) has a maximal uncertainty of 8%. However, IR spectroscopy is that sensitive for changes in the neighborhood of the OH group that the effect is significantly pronounced in the autocorrelation analysis of the OH stretching bands in the IR spectra (Fig. 6.2).

The Al–F/OH bonds are about 0.1 Å smaller than the other Al–O bonds of the Al octahedra (e.g., Gatta et al. 2006b). Increasing OH incorporation results in an increasing distortion of the Al octahedra, which is possibly compensated by further twisting of the octahedral chains along b. It is as well probable that the angle of the O–H dipole changes with increasing OH content. The distance between two neighboring OH groups is preferentially as large as possible, which can be accomplished by an opposed rotation/relaxation of the dipole. Because the proportion of the OH$\cdots$OH configuration increases mutually with the OH content, the degree of rotation of neighboring OH groups increases, too. At room temperature, topaz-OH has two non-equivalent H positions in a diagonal configuration, which results in a symmetry reduction to space group $Pbn2_1$ (Northrup et al. 1994; Watenphul and Wunder 2009).

Structural changes such as further twisting of the octahedral chains and/or rotation of the OH dipole with increasing OH concentration would contribute to the non-linear evolution of the bandwidths as well. However, complete and detailed structural parameters, determined of selected samples of the complete (F,OH) solid solution range, are missing in the literature and go beyond the scope of this study.

6.5.3 T dependence of the OH stretching frequencies

The temperature dependence of the two OH stretching frequencies was investigated on a thin film of sample Top16 with $X_{OH} = 0.23$ and on single-crystal plates of Top-E with $X_{OH} = 0.075$. In a first attempt we assume that the observed behavior of the OH stretching frequencies with temperature is independent of the OH concentration, and therefore can be generalized to every topaz sample, except both end members. With increasing temperature, the selected spectra in Fig. 6.3 show a shift of the OH stretching bands to lower wavenumbers and the first narrow bands broaden along with decreasing absorbance. The same behavior was also observed by Aines and Rossman (1985) between -196 and 750°C, albeit they observed an intensity increase of the OH stretching frequencies with temperature. However, their topaz sample shows some additional OH bands caused by OH in anomalous positions, which is related to radiation damage. With increasing temperature, these OH groups re-equilibrate to the normal positions (corner of the Al octahedron) and thus, the intensities of the typical OH stretching bands, ν_B and ν_A, increase. Unlike topaz-OH (Watenphul and Wunder 2009), topaz of the (F,OH) solid solution series displays no splitting of the OH bands in the IR spectra at -196°C. Thus, the frequency difference between ν_A and ν_B is even too small to induce a band splitting among the narrow bands at this low temperature. This is reasonable, because ν_A originates from an only slightly different local surrounding in the crystal structure of topaz. Decreasing temperature causes a volume contraction and therefore a shortening of the interatomic distances. Nevertheless, the change of the local surrounding of the OH groups is too small to cause a significant frequency

difference between both OH bands, which is visible in the IR spectra.

"Normal" peak fitting gives only insufficient data for the band positions and bandwidths of both OH stretching bands. Therefore, a simplification to one superposed OH band was made to extract data of the temperature-dependent bandshift and a superposed bandwidth. Both variables decrease with increasing temperature up to about 150°C ± 25°C, where their slopes display a distinct discontinuity (Fig. 6.4). The decrease of the band position with increasing temperature can be interpreted as a shortening of the O–H$\cdots$O distance, respectively the O$\cdots$H distance (Libowitzky 1999). The neutron diffraction data by Gatta et al. (2006b) reveals that the H$\cdots$O3 distance decreases from 2.386(6) Å at -263°C to 2.380(5) Å at 25°C, whereas all other H$\cdots$O distances increase with increasing temperature. The respective F/O4–H$\cdots$O(3) bond angle shows a similar decrease with temperature. The conformity in the behavior of bond distance and angle suggests that the O4–H$\cdots$O3 bond controls the temperature-dependent behavior of the OH stretching bands between -263 and 25°C and most likely at higher temperatures, too.

A decrease in the superposed bandwidth with increasing temperature up to 150°C implies that the frequency difference between ν_A and ν_B is reduced. It seems that the decreases of the O4–H$\cdots$O3 bond and the corresponding bond angle are also dependent on the occupation of the adjacent sites with OH or F. Both OH stretching bands increasingly broaden at temperatures above about 150°C, because of the increased thermal vibration of the OH groups. This band broadening prevails the small approach of both OH bands, which results from the decrease of the O4–H$\cdots$O3 bond with increasing temperature. Thus, the total bandwidth of the superposed band increases with increasing temperature above 150°C.

The slope changes at the discontinuities are abrupt compared to the continuous change observed in Fig. 6.2 for the X_{OH} dependence. Such an abruptness is a clear indication for a phase transition.

Autocorrelation analysis of the temperature-dependent spectra shows a similar behavior of ΔCorr with increasing temperature. The analysis of the complex bandshape of both OH stretching bands reveals even two discontinuities in the slope, the first at about -150°C ± 25°C and the second at about 160°C ± 25°C (Fig. 6.5). It is evident that the $\sim$ 150°C-discontinuity in Fig. 6.4 and the $\sim$ 160°C-discontinuity in Fig. 6.5 originate from the same phenomenon. The low-temperature transition is further confirmed by an autocorrelation analysis of polarized temperature-dependent IR spectra. Both polarization directions, E $\parallel$ X and E $\parallel$ Z, display a distinct slope discontinuity at -135°C ± 5°C (Fig. 6.6). The reduced uncertainty of the transition temperature is related to the smaller temperature-step size of these spectra. In the following, the temperatures determined by the autocorrelation analyses are used, because of the superior quality of these data. Therefore, topaz displays two temperature-dependent phase transitions at -135°C ± 5°C and at about 160°C ± 25°C.

The identification of the involved space groups in the temperature-dependent phase transitions is difficult, because of lacking crystal structure data on local order/disorder to confirm these transitions. However, crystal structure investigations, which are normally used to determine the space group of minerals, are sensitive to the long-range order (LRO), whereas we propose that the phase transitions in topaz are related to short-range order–disorder of F and OH. Therefore, the here proposed space groups are based on the combination of knowledge gained from crystal structure investigations (Zemann et al. 1979; Parise et al. 1980;

Komatsu et al. 2003; Gatta et al. 2006b) along with reasonable assumptions on changes in the crystal structure with temperature and the information on the short-range order (SRO) from our IR spectroscopic investigation.

The structural refinements, which lead to space group *Pbnm* for topaz (e.g., Zemann et al. 1979; Alberico et al. 2003; Komatsu et al. 2003; Gatta et al. 2006b), make no difference between F and O4 occupation of the Al octahedra corners. However, at room temperature F and OH are statistically distributed in the crystal structure, which leads to a certain distribution of the three different, local F/OH arrangements, i.e., F$\cdots$F, F$\cdots$OH (= OH$\cdots$F), OH$\cdots$OH (Fig. 6.8). The extent depends on the OH concentration. Our investigations showed that this short-range ordering explains the occurrence and relative intensities of the OH stretching bands ν_A and ν_B in the IR spectra and, therefore, is non-negligible. Excluding both end members, the necessary consideration of the short-range ordering requires locally the loss of the mirror plane (001), and hence, the local symmetry reduction of the topaz space group from *Pbnm* to $Pbn2_1$. Thus, only the fluorine end member, $Al_2SiO_4F_2$, can be described in space group *Pbnm* from local to bulk scale. In contrast, topaz-OH has space group $Pbn2_1$ at room temperature (Northrup et al. 1994; Watenphul and Wunder 2009). The hydrogen atoms are located on average in two non-equivalent positions in the crystal structure, i.e., A–B or B–A, but never A–A or B–B, which requires the symmetry reduction of *Pbnm* to $Pbn2_1$ by loss of the mirror plane (001).

In case of order–disorder phase transitions caused by temperature, the space group symmetry generally increases with increasing temperature. Therefore, we suggest that the topaz space group changes from *P1* to $Pbn2_1$ at -135°C and from $Pbn2_1$ to *Pbnm* at about 160°C. Temperature-dependent structure investigation by neutron diffraction at -263 and 25°C revealed no deviation from space group *Pbnm* (Gatta et al. 2006b). This does not have to be a contradiction to our proposed symmetry, if one takes into account that diffraction studies investigate the long-range order (LRO) of the crystal structure and average the properties over many unit cells, whereas spectroscopic studies reveal even the short-range order (SRO) and are sensitive to local structure differences. Moreover, it suggests that the structural changes, which cause the low-temperature phase transition, bear on the OH groups and their local surrounding.

Parise et al. (1980) reported space group *P1* for topaz from a neutron diffraction study due to the occurrence of certain reflections, which are forbidden in space group *Pbnm*. In *Pbnm*, hydrogen occupies eight equivalent sites in the crystal structure. Local ordering, caused by two OH groups occupying adjacent positions (see above), might induce a splitting into a second type of hydrogen site. In the regular H site the protons of the neighboring OH groups approach too closely, so that they are deflected into two new positions (Parise et al. 1980; Aines and Rossman 1985). Gatta et al. (2006b) also observed forbidden reflections in their diffraction studies. In contrast to Parise et al. (1980), they argued that these reflections could be ascribed to the Renninger effect, which describes double diffraction phenomena, so that the space group of topaz was confirmed in *Pbnm*. As the case may be, splitting of the hydrogen site comparable to those described by Parise et al. (1980) might be responsible for the low-temperature phase transition. At low temperature, the crystal structure is contracted and the interatomic distances are shortened. Dynamic fluctuations and thermal vibrations are frozen in. As a consequence, the hydrogen positions of two ordered OH groups approach too closely for a simultaneous occupation of both positions in

the normal symmetry. A possible small rotation of both OH dipoles increases the distance between the H atoms and results in two non-equivalent H positions. These non-equivalent H site are closely adjacent similar to the H sites in topaz-OH (Watenphul and Wunder 2009). However, the splitting of the hydrogen positions violates all symmetry elements, so that topaz at temperatures below -135°C has at least locally space group *P1*. Increasing temperature elongates all interatomic distances, so that both hydrogen atoms of neighboring OH groups are relocated in the normal symmetry position and the space group changes to $Pbn2_1$. The slope change of ΔCorr at the low-temperature transition is significant (Fig. 6.5, Fig. 6.6), but less pronounced than the one at the high-temperature transition. This favors the assumption of two closely adjacent H positions. The closeness of the splitted H sites results in an only very small frequency difference between the resulting OH stretching bands in an IR spectrum, which might not be resolvable. This is in agreement with the observed IR spectra at low temperature (Fig. 6.3), which show no bandsplitting, but an enlarged bandwidth.

The detection of two closely adjacent hydrogen positions as in the low-temperature structure is very challenging. However, a very thorough neutron diffraction study on deuterated topaz samples of the solid-solution series might be able to confirm this theory and determine a symmetry reduction to *P1*.

The high-temperature phase transition at about 160°C might originate from order–disorder processes of F and OH in the crystal structure. The increased thermal vibration of the anions with temperature allows on average the disordering of F and OH over the whole crystal structure. The increased temperature reduces the local ordering, so that on average the space group changes from $Pbn2_1$ to *Pbnm*.

Komatsu et al. (2003) investigated the effect of temperature on the topaz crystal structure on a natural topaz sample with $X_{OH} = 0.215$. We re-plotted their data and thereby scaled down the axes of the lattice parameters (Fig. 6.9). This closer look reveals that the increase of *a*, *b*, and *c* with temperature is not linear within the reported uncertainties, but displays a slope change at about 150°C, which was not noticed by Komatsu et al. (2003). We assume that these discontinuities in the lattice parameters correspond to the phase transition at about 160°C observed by the autocorrelation analysis of the temperature-dependent IR spectra. The deviation in the transition temperature evidently originates from the wide temperature intervals of 150°C between each of the structure investigations of Komatsu et al. (2003). Hence, the disordering of F and OH has also an effect on the expansion of the crystal structure with temperature. The slope change of ΔCorr with temperature is more pronounced for the high-temperature transition. This might be the reason why this transition is also visible in structural data, whereas the low-temperature transition is not detected, yet.

It is very probable that temperature-dependent crystal structure investigations on deuterated topaz of the solid solution series will detect the symmetry change(s) with temperature. Moreover, the effect on the lattice parameters with temperature will be significantly increased because of the larger ionic radius of $(OD)^-$ compared to $(OH)^-$.

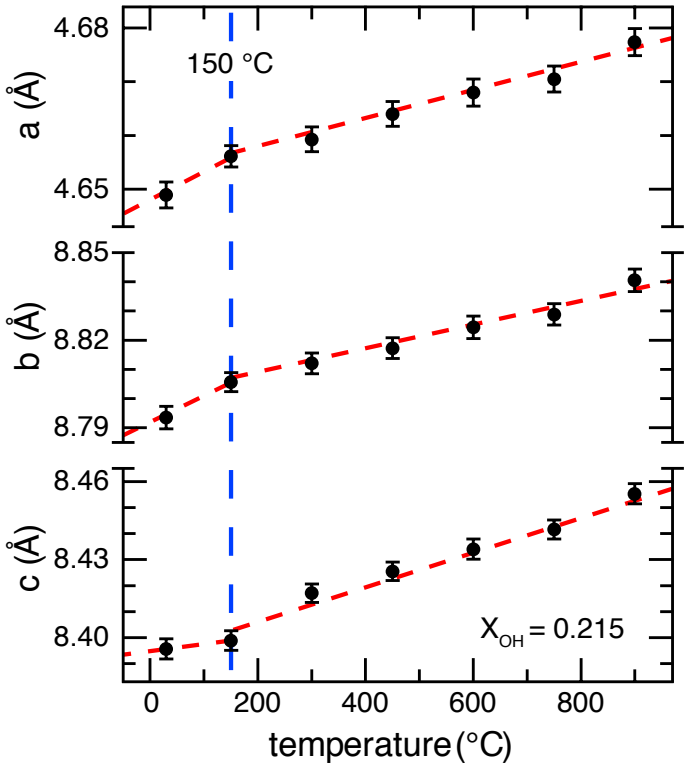

Figure 6.9: Temperature-dependence of the unit cell parameters determined by Komatsu et al. (2003) from X-ray diffraction data. Data are re-plotted with enlarged axis scaling. The dashed red lines illustrate changes in the slopes. The vertical blue line indicates the discontinuities in the slopes at about 150°C.

6.6 Conclusion

The existence of two OH stretching bands in the IR spectra of topaz from the (F,OH)-solid solution series is caused by the local surrounding of the F/OH site in the crystal structure. The typical sharp OH band is related to OH groups with fluorine in the adjacent site, whereas two adjacent OH groups result in a second OH band, which is visible as a shoulder on the low-energy side of the sharp band. The amount of local OH–OH ordering in neighboring sites is determined by OH concentration and can be calculated by probability calculations. The substitution of OH for F has a non-linear effect on the expansion of the crystal structure.

Autocorrelation analysis of the temperature-dependent IR spectra revealed two temperature-induced phase transitions. At about -135°C, the space group is suggested to change from *P1* to $Pbn2_1$ and at about 160°C from $Pbn2_1$ to *Pbnm*. The low-temperature transition is caused by the temperature-dependent contraction of the crystal structure. Two neighboring hydrogen positions approach too closely for simultaneous occupation. Splitting/relaxation of the H atoms in two closely adjacent, non-equivalent sites results in a symmetry reduction to *P1*. The high-temperature transition originates from temperature-

induced disorder of the local F–F/OH–OH ordering in neighboring sites. The increased movement of the anions leads on average to a complete disorder of F and OH in the crystal structure.

The sensitivity of the OH stretching frequency on the local surrounding, i.e. the occupation of the neighboring site by F or OH, suggests that the OH stretching band of other (F,OH)-bearing solid solutions may have also multiple components, which are related to the local ordering of F and OH in the crystal structure. Possible candidates might be the humite group, the mica group, the amphibole group, and talc. It is very probable that temperature will induce phase transitions in these minerals similar to the presented phase transitions in topaz.

Acknowledgments We thank M. Koch-Müller for the help with the thin film preparation and C. Schmidt for fruitful discussions. This work was supported by the German Science Foundation (He 2015/(8-1)) to W. Heinrich within the framework of the Priority Program 1236 "Structures and properties of crystals at extreme pressures and temperatures", which is gratefully acknowledged.

6.7 References

Aines RD, Rossman GR (1985) The high-temperature behavior of trace hydrous components in silicate minerals. Am Mineral 70:1169-1179

Alberico A, Ferrando S, Ivaldi G et al. (2003) X-ray single-crystal structure refinement of an OH rich topaz from Sulu UHP terrane (Eastern China) – Structural foundation of the correlation between cell parameters and flourine content. Eur J Mineral 15:875-881

Alston NA, West I (1928) The structure of topaz $[Al(F,OH)]_2SiO_4$. Proc R Soc London A121:358-367

Barton MD (1982) The thermodynamic properties of topaz solid solution and some petrological applications. Am Mineral 67:956-974

Beny JM, Piriou B (1987) Vibrational spectra of single-crystal topaz. Phys Chem Miner 15:148-154

Bradbury SE, Williams Q (2003) Contrasting behavior of two hydroxyl-bearing metamorphic minerals under pressure: Clinozoesite and topaz. Am Mineral 88:1460-1470

Domanik KJ, Holloway JR (1996) The stability and composition of phengitic muscovite and associated phases from 5.5 to 11 GPa: implications for deeply subducted sediments. Geochim Cosmochim Acta 60(21):4133-4415. doi:10.1016/S0016-7037(96)00241-4

Fei Y (1995) Thermal expansion. In: Mineral Physics and Crystallography – a handbook of physical constants. AGU Ref Shelf 2:29-44

Gatta GD, Nestola F, Boffa Ballaran T (2006a) Elastic behaviour and structural evolution of topaz at high pressure. Phys Chem Miner 33:235-242

Gatta GD, Nestola F, Bromiley GD et al. (2006b) New insight into crystal chemistry of topaz: A multi-methodological study. Am Mineral 91:1839-1846

Gebert W, Zemann J (1965) Messungen des Ultrarot-Pleochroismus von Mineralen. III. Der Pleochroismus der OH Streckfrequenz in Topas. N Jb Mineral Mh 1965: 380-384

Komatsu K, Kuribayashi T and Kudoh Y (2003) Effect of temperature and pressure on the crystal structure of topaz, $Al_2SiO_4(OH,F)_2$. J Miner Petrol Sci 98:167-180

Komatsu K, Kagi H, Okada T et al. (2005) Pressure dependence of the OH stretching mode in F-rich natural topaz and topaz-OH. Am Mineral 90:266-270. doi:10.2138/am.2005.

Libowitzky E (1999) Correlation of O–H stretching frequencies and O–H$\cdots$O hydrogen bond lengths in minerals. Monatsh Chem 130:1047-1059

Libowitzky E, Beran A (2006) The structure of hydrous species in nominally anhydrous minerals: information from polarized IR spectroscopy. In: Keppler H and Smyth JR (eds) Water in nominally anhydrous minerals, Rev Mineral Geochem, Vol. 62, pp 29-52

Libowitzky E, Rossman GR (1997) An IR absorption calibration for water in minerals. Am Mineral 82:1111-1115

Mikenda W, Steinböck S (1994) Stretching frequency versus bond distance correlation of O–D(H)$\cdots$F hydrogen bonds in solid hydrates. J Mol Struct 326:123-130

Mikenda W, Steinböck S (1996) Stretching frequency vs. bond distance correlation of hydrogen bonds in solid hydrates: a generalized correlation function. J Mol Struct 384:159-163

Northrup PA, Leinenweber K, Parise JB (1994) The location of H in the high-pressure synthetic $Al_2SiO_4(OH)_2$ topaz analogue. Am Mineral 79:401-404

Ono S (1998) Stability of hydrous minerals in sediment and mid-ocean ridge basalt composition: Implications for water transport in subduction zones. J Geophys Res 103:18253-18267

Ono S (1999) High temperature stability limit of phase egg, $AlSiO_3(OH)$. Contrib Mineral Petrol 137:83-89. doi:10.1007/s004100050583

Parise JB, Cuff C, Moore FH (1980) A neutron diffraction study of topaz: evidence for a lower symmetry. Mineral Mag 43:943-944

Pauling L (1928) The crystal structure of topaz. PNAS 14:306

Pinheiro MVB, Fantini C, Krambrock K et al. (2002) OH/F substitution in topaz studied by Raman spectroscopy. Phys Rev B 65:104301

Ribbe PH (1982) Topaz. In: Ribbe PH (ed) Orthosilicates, 2^{nd} ed. Rev Mineral, pp 215-230

Ribbe PH, Rosenberg PE (1971) Optical and X-ray determinative methods for fluorine in topaz. Am Mineral 56:1812-1821

Rosenberg PE (1972) Composition variation in synthetic topaz. Am Mineral 57:168-187

Salje E, Carpenter MA, Malcherek T et al (2000) Autocorrelation analysis of infrared spectra from minerals. Eur J Mineral 12:503-519

Schmidt MW (1995) Lawsonite: Upper pressure stability and formation of higher density hydrous phases. Am Mineral 80:1286-1292

Schreyer W (1995) Ultradeep metamorphic rocks: the retrospective viewpoint. J Geophys Res 100(B5):8353-8366. doi:10.1029/94JB02912

Shinoda K and Aikawa N (1997) IR active orientation of OH bending mode in topaz. Phys Chem Miner 24:551-554

Theye T (1988) Aufsteigende Hochdruckmetamorphose in Sedimenten der Phyllit-Quarzit-Einheit Kretas und des Peloponnes. PhD Thesis, University of Braunschweig

Watenphul A, Wunder B (2009) Temperature-dependence of the OH stretching frequencies of topaz-OH. Phys Chem Miner, *in press*, doi:10.1007/s00269-009-0310-6

Wells AF (1984) Structural inorganic chemistry. 5^{th} edn. Clarendon Press, Oxford, New York

Wirth R, Wunder B (2000) Characterization of OH containing phases by TEM using electron energy-loss spectroscopy (EELS): clinohumite-OH, chondrodite-OH, phase A and the (F,OH)-solid solution series of topaz. J Trace Microprobe T 18:35-49

Wunder B, Rubie DC, Ross II CD et al. (1993) Synthesis, stability, and properties of $Al_2SiO_4(OH)_2$: A fully hydrated analogue of topaz. Am Mineral 78:285-297

Wunder B, Andrut M, Wirth R (1999) High-pressure synthesis and properties of OH rich topaz. Eur J Mineral 11:803-813

Xu, S (1994) Ultra-high-pressure mineral assemblage of Dabie Shan metamorphic rocks, Eastern China (abstract). IMA conference, Pisa, Italy, 445-446

Zemann J, Zobetz E, Heger G et al. (1979) Strukturbestimmung eines OH reichen Topases. Öster Akad Wiss, Math-Naturwiss Kl 116:145-147

Zhang RY, Liou JG, Shu JF (2002) Hydroxyl-rich topaz in high-pressure and ultrahigh-pressure kyanite quartzites, with retrograde woodhousite, from the Sulu terrane, eastern China. Am Mineral 87:445-453

7 Eidesstattliche Erklärung

Hiermit versichere ich, dass ich die vorliegende Arbeit selbstständig verfasst und keine anderen als die aufgeführten Quellen und Hilfsmittel verwendet habe. Die Stellen der Arbeit, die anderen Werken wörtlich oder inhaltlich entnommen sind, wurden durch entsprechende Quellenangaben kenntlich gemacht.

Diese Arbeit hat in gleicher oder ähnlicher Form noch keiner Prüfungsbehörde vorgelegen.

Potsdam, den 19. November 2009

Anke Watenphul

8 Danksagung

Die vorliegene Arbeit wäre ohne die Unterstützung vieler Freunde und Kollegen undenkbar, bei ihnen möchte ich hier ganz herzlich bedanken.

An erster Stelle möchte ich mich bei Wilhelm Heinrich für die gute Betreuung, die vielen Diskussionen, seine wunderbaren Erklärungen zur Geochemie und Mineralogie, seine Unterstützung bei allen Projekten, die gerne erzählten “Lebensweisheiten” und nicht zuletzt für seine große Geduld bedanken.

Bernd Wunder danke ich für die vielen Gespräche und Diskussionen, die Hilfe bei den Piston Cylinder-Experimenten und für das stetige Interesse am Fortgang dieser Arbeit.

Bei Christian Schmidt möchte ich mich für die vielen Aufmunterungen in der letzen Zeit, die Beantwortung der verschiedensten Fragen und die Erklärungen zur HDAC und dem Raman Spektrometer bedanken. Besonders danke ich ihm für das Korrekturlesen dieser Arbeit und die ausführlichen Erklärungen zum englischen Satzbau (SPO).

Das Experimentieren an der Multi-Anvil-Presse und die Grundlagen der IR-Spektroskopie habe ich von Monika Koch-Müller erlernt. Dafür ein großes Dankeschön.

Matthias Gottschalk danke ich für die Einführung in die Röntgenpulverdiffraktometrie und die Datenauswertung mittels Rietveld-Verfeinerung, die Hilfe bei meinen Mac-Problemen und das “Verleihen” seines Büros.

Besonderer Dank gilt Reiner Schulz für das prompte Lösen der vielen kleinen und großen technischen Probleme.

Andreas Hahn, Heike Steigert und Hans-Peter Nabein danke ich für die schnellen Röntgenaufnahmen, Oona Appelt und Dieter Rhede für die Hilfe bei den Messungen an der Mikrosonde, Richard Wirth für die Durchführung der TEM-Analysen, Helga Kemnitz und Ulrich Gernert für die schönen SEM-Bilder, Gerhard Berger, Karin Paech und Anja Schreiber bin ich sehr dankbar für die Präparation der ”ach so winzigen” Proben.

Den Kollegen der Hochdruckwerkstatt, insbesondere Theo Steiner und Reik Sünkel, möchte ich für die Anfertigung der kleinen Kapseln, Öfen und sonstigen Teile für die Multi-Anvil-Versuche danken. Ohne Ihre präzise Arbeit wären nur die Hälfte aller Versuche so gut gelungen.

Die Veröffentlichungen und Manuskripte in dieser Arbeit sind durch die Mithilfe aller Koautoren und durch die hilfreichen Gutachten der Rezensenten und Editoren stetig verbessert worden, vielen Dank dafür.

Alle Kollegen der Sektion 3.3 haben die letzen 3 Jahren zu einer sehr schönen Zeit mitgestaltet. Besonders die vielen lustigen Abende im Hafthorn nach Feierabend mit meinen Doktoranden-Kollegen Manu, Fiore, Basti, Nick und Gregor und allen, die sich uns angeschlossen haben, werde ich in bester Erinnerung behalten, auch dank der vielen Fotos, die es davon gibt.

Mein ganz besonderer Dank gilt meinen Familie und meinen Freunden, die mich immer unterstützt haben und ohne welche es diese Arbeit so nicht gegeben hätte.